Dissertation
submitted to the
Combined Faculties of Natural Sciences and
Mathematics
of Heidelberg University, Germany
for the Degree of
Doctor of Natural Sciences

Put forward by

Dmytro Dmytriiev
Born in: Kyiv, Ukraine
Oral examination: 19/01/2022

Design of a position sensitive resonant Schottky detector for the Rare-RI Ring in RIKEN

Referees: Apl.Prof. Dr. Yuri A. Litvinov
Priv.-Doz. Dr. Wolfgang Quint

Supervisors: Apl.Prof. Dr. Yuri A. Litvinov
Prof. Dr. Klaus Blaum

Abstract

Studying the rapid neutron capture process (r-process) in stellar environment, that leads to the creation of about half of elements heavier than Fe, remains one of the fundamental questions of modern physics and therefore an active field of interdisciplinary research within nuclear structure, atomic and plasma physics, particle physics as well as nuclear astrophysics. Apart from other key measurable like neutron capture cross sections and decay lifetimes, nuclear masses are of utmost importance for pinpointing the r-process using theoretical and experimental approaches. Exotic nuclides which participate in the r-process typically have extremely low production yields and short half-lifes. Those, accessible today at radioactive-ion beam facilities can be efficiently investigated in a storage ring. In such facilities non-destructive methods of particle detection are often used for in-flight measurements based on a frequency analysis. Due to low particle number and thus inevitably the low signal level, the detectors should be very sensitive and fast. While there are many sensitive detectors available to provide the information on particle's revolution frequency, the main idea of this work is to design a position-sensitive cavity doublet for the Rare-Ri storage ring in RIKEN, Japan.

Additionally, a new data acquisition system based on the software defined radio (SDR) was developed and tested with an existing resonant Schottky pickup during an experimental campaign in the ESR at GSI Darmstadt. SDR based data acquisition systems are essential for use in future distributed pickup systems such as those planned in the collector ring (CR) of the FAIR project.

Finally a fully automated measurement system has been developed that can be used to measure the field profiles of such cavities in conjunction with the above mentioned data acquisition system. A toy model of such a position-sensitive resonant Schottky cavity doublet has been designed, constructed, manufactured and tested using the automated measurement system in the lab as well as at the linear accelerator S-DALINAC at University of Darmstadt.

Zusammenfassung

Die Erforschung des Schnellen Neutroneneinfachprozesses (r-Prozess) innerhalb von Sternen, der zur Erzeugung von Elementen schwerer als 56-Fe führt, bleibt einer der fundamentalen Fragestellungen der modernen Physik und ist deshalb ein aktives Forschungsfeld innerhalb der nuklearen Astrophysik. Neben anderen wesentlichen Messgrößen wie Neutroneneinfangquerschnitten und Zerfallskonstanten sind die Kernmassen von größter Bedeutung, um den Beitrag des r-Prozesses mittels theoretischer und experimenteller Methoden genau zu bestimmen. Exotische Kerne, die zum r-Prozess beitragen, besitzen typischerweise geringe Produktionsquerschnitte und kurze Halbwertszeiten. Jedoch können sie effizient in einem Speicherring untersucht werden. In solchen Anlagen werden oft nicht-destruktive Methoden zur Teilchendetektion basierend auf einer Frequenzanalyse verwendet. Aufgrund der geringen Signalstärke sollten die Detektoren äußerst sensitiv und schnell sein. Während viele sensitive Detektoren zur Messung der Umlauffrequenz der Teilchen existieren, ist die wesentliche Idee dieser Arbeit der Entwurf eines positionsempfindlichen Kavitätendoublets für den Rare-RI Speicherring bei RIKEN in Japan.

Zusätzlich wurde ein neues Datenerfassungssystem auf der Basis von Software Defined Radio (SDR) entwickelt und mit einem bestehenden resonanten Schottky-Pickup während eines Experiments im ESR an der GSI in Darmstadt getestet. SDR-basierte Datenerfassungssysteme sind essentiell für den Einsatz in zukünftigen verteilten Pickup-Systemen, wie sie im Collector Ring (CR) des FAIR-Projekts geplant sind.

Schließlich wurde ein vollautomatisches Messsystem entwickelt, das in Verbindung mit dem oben erwähnten Datenerfassungssystem zur Messung der Feldprofile solcher Kavitäten verwendet werden kann. Ein Modell eines solchen positionssensitiven resonanten Schottky- Kavitätendoubletts wurde entworfen, konstruiert, hergestellt und mit dem automatisierten Messsystem sowohl im Labor als auch am Linearbeschleuniger S-DALINAC der Universität Darmstadt getestet.

Contents

1 Introduction **1**
1.1 Nuclear Physics at Heavy-Ion Storage Rings . . . 1
1.2 Nuclear Mass and Lifetime Measurements . . . 1
1.3 Schottky Measurements at Storage Rings . . . 2
1.3.1 Schottky Mass Spectrometry . . . 3
1.3.2 Isochronous Mass Spetrometry . . . 4
1.3.3 Anisochronism Effect and its Corrections . . . 4
1.4 Motivation . . . 5

2 Theoretical Description **7**
2.1 Electrodynamics of a Cavity . . . 7
2.2 Shunt Impedance . . . 8
2.3 Couplers and Coupling Factor . . . 10
2.4 Tuning and Detuning . . . 12
2.5 Signal from the Cavity . . . 12
2.6 Correction for the Anisochronism Effect . . . 14

3 Design of a Position-Sensitive Cavity Doublet for R3 Ring **19**
3.1 Mechanical Restrictions Based on the R3 Blueprints . . . 19
3.2 Field Propagation Simulations . . . 20
3.3 Longitudinal Extension of the Cavity . . . 25
3.4 R/Q Distributions for Different Cavity Geometries . . . 27
3.5 Blending of the Pipe Walls Edges . . . 29
3.6 Blending of the Pipe-Cavity Connection . . . 32
3.7 Tuners Simulations . . . 35
3.8 Couplers . . . 43

4 Software Defined Radio Based Data Acqusition System **47**
4.1 Test measurements at ESR . . . 47
4.2 Noise Sources . . . 50

5 Automated Measurement System and an Adapted Position-Sensitive Cavity Doublet Model **53**
5.1 Mechanical Restrictions . . . 55
5.2 Lab Measurements . . . 55
5.2.1 Position Calculation and its Error . . . 55
5.2.2 Coupler Tests . . . 57
5.2.3 Tuner Measurements . . . 59
5.2.4 R/Q Map Measurements . . . 61
5.3 Experimental Setup at S-DALINAC . . . 62
5.4 Wire Measurements at S-DALINAC . . . 64

6 Summary and Conclusion **65**

7 Appendix **67**
7.1 Field Distributions for Different Modes in Elliptical Cavities 67
7.2 Simulations for the S-DALINAC Prototype 69
7.3 TCAP, NTCAP and SDR Comparison 72
7.4 Driving System 73
7.4.1 SWISSBOY 122M Lifter 73
7.4.2 ISEL Stepper Motor and Driver 74
7.5 SDR-based DAQ 75
7.5.1 Megatron Potentiometers 75
7.5.2 Assembled DAQ 76
7.6 Blueprints 78
7.7 Circuit schematics and PCB 82
7.8 Gerber files 85
7.9 SDR Program 89
7.10 List of publications 94

8 Acknowledgments **101**

1 Introduction

1.1 Nuclear Physics at Heavy-Ion Storage Rings

Heavy-Ion storage rings with their large momentum acceptance can store ions of different species simultaneously [1]. Utilization of the beam cooling devices or special ion-optical settings can turn a storage ring into a precise mass spectrometer [2]. This allows direct ion identification and mass measurement with a high precision ($10^{-6} - 10^{-7}$) [1]. A second advantage of a storage ring is the possibility to conduct decay studies if time-resolving detectors are present. Due to the high vacuum of the storage rings($10^{-10} - 10^{-12}$ mbar), reactions with residual gas are reduced allowing stored ions to circulate for greater times [1]. ESR is the experimental storage ring at the GSI facility in Darmstadt, Germany [3]. The scheme of ESR is illustrated in Fig. 1.1b. This facility together with linear accelerator UNILAC, synchrotron SIS 18, and a fragment separator FRS can produce, accelerate and store a wide variety of ion species from hydrogen to the uranium at different charge states. An illustration of the GSI and planned FAIR facility is shown in Fig. 1.1a. Other storage rings that conduct experiments with exotic nuclei from different regions of the nuclear chart such as CRYRING [4] at GSI, CSR [5] at IMP, Lanzhou, China and the Rare-RI Ring [6, 7] at RIKEN, Saitama, Japan.

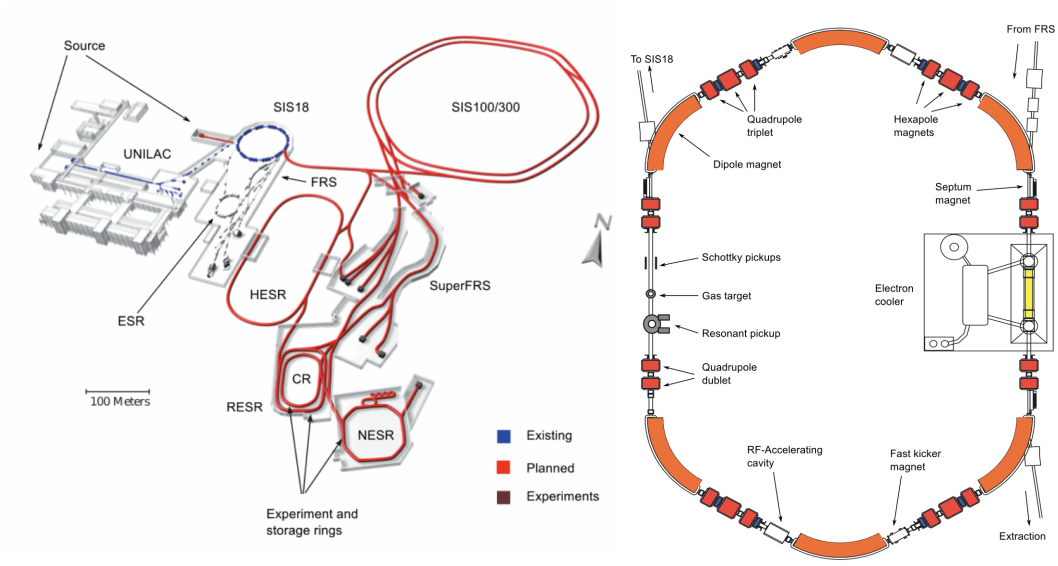

(a) GSI and planned FAIR facilities. (b) ESR schematic layout.

Fig. 1.1: The scheme of the ESR together with linear accelerator UNILAC, synchrotron SIS 18 , and a fragment separator FRS.

1.2 Nuclear Mass and Lifetime Measurements

Nuclear mass is an observable of the interaction of the three fundamental (electromagnetic, strong, and weak) forces inside nuclei. Usually, it is used to test the reliability and validity of nuclear structure theories [8]. As a result of these tests, the difference between predicted and measured masses may reveal new insight into the existing theories. For example, nuclear shell

closure was discovered at magic numbers of 20, 50, 82, 126 [9] by comparing results from the liquid drop model with measured masses [10].

One characteristic mass measurement which was conducted at ESR was ^{208}Hg ion. There was only one ion produced in ESR during the two weeks of beam time [11]. That measured mass was the last quantity needed for the calculation of the proton-neutron interaction strength of ^{210}Pb. It was found that proton-neutron interaction strength for ^{210}Pb was approximately 2.5 times smaller than for ^{208}Pb which is a doubly magic nucleus. This number is consistent with the theoretical prediction.

The main motivation for construction of the ESR was the study of the β^- decay of highly charged nuclei [12]. This knowledge is particularly necessary for an understanding of the stellar nucleosynthesis processes. Taking into account hot stellar interiors conditions (30-100 keV) one can say that only a few or even zero electrons are bound to the nucleus [13]. This affects the decay channels in comparison to the those in a neutral atom. For example, orbital electron capture (EC) channel does not exist for bare ions whereas bound state β -decay ($\beta_b{}^-$) could energetically become possible [14].

A series of experiments dedicated to nuclear lifetimes of exotic nuclei was conducted at ESR. Due to the large momentum acceptance of the ESR different decay channels can be observed simultaneously and the branching ratio of a certain decay can be determined [15]. Some experiments are listed below:

- The first $\beta_b{}^-$ decay was observed in 1992 for ^{163}Dy^{66+}. Despite the fact that neutral ^{163}Dy is stable a bare ion ^{163}Dy^{66+} has a $\beta_b{}^-$ decay to its K or L electron shell of ^{163}Ho^{66+} [16]. The half-life of ^{163}Dy^{66+} of 48(3) days set the upper limit (275 eV) for the mass of the electron neutrino [17].

- The ratio between bound state $\beta_b{}^-$-decay to continuum state $\beta_c{}^-$-decay was measured for ^{207}Tl [18]

- Pure β^+ branch was measured for bare ^{52g}Fe and ^{53g}Fe and the sum of the β^+ and γ branch was measured for bare ^{52m}Mn and ^{53m}Fe [19]

- The cross sections of the ^{118}Te^{52+}(p,γ), ^{118}Te^{52+}(p,n), ^{124}Xe^{54+}(p,γ) and ^{124}Xe^{54+}(p,n) have been measured. For Te this was the first time this proton capture has been measured using a stored radioactive beam. The measured cross-sections are important to fully understand the production of the neutron-deficient stable isotopes [20]

- The lifetime of the bound state $\beta_b{}^-$-decay for bare ^{205}Tl^{81+} ions has been measured. It plays an important role for the ^{205}Pb/^{205}Tl pair as an s-process cosmochronometer and for the LOREX experiment designed for the measurements of the pp solar neutrino flux [**sidhu_rs__measurement_2021**].

1.3 Schottky Measurements at Storage Rings

The revolution frequency of the particles in a storage ring depends on their mass-to-charge ratio m/q and speed v. The equation, which quantitatively defines the difference in mass-over-charge ratios of the two different particles is given below:

$$\frac{\Delta f}{f_{rev}} = -\frac{1}{\gamma_t^2}\frac{\Delta(m/q)}{(m/q)} + \frac{\delta v}{v}\left(1 - \frac{\gamma^2}{\gamma_t^2}\right) \tag{1.1}$$

where Δf is the frequency difference between the central frequencies of the peaks, γ is relativistic factor and γ_t is the transition energy of the ring which is defined by the optics of the

ring. As one can see from equation (1.1) revolution frequency of any particle in the ring f_{rev} is defined not only by its mass-to-charge ratio but also by its speed. In order to conduct precision mass-spectrometry measurements, one has to eliminate the influence of the second term. There are two common approaches leading to this point: beam cooling (reducing the velocity spread δv) or adjusting the ring optics in such a way that the transition energy γ_t of the ring is equal to the relativistic factor γ of the ions. The first method allows conducting Schottky Mass Spectrometry (SMS), whereas the second one is utilized for needs of the Isochronous Mass Spectrometry(IMS). The measurements of the EC-decay of $^{142}Pm^{60+}$ ion using the SMS are shown in Fig. 1.2. Successful installation of two intensity sensitive and capable of time-reloved measurements Schottky cavities at ESR [21, 22] allow it to conduct SMS and IMS. Measurements of masses and lifetimes at ESR now have a lower time limit of around 30 ms set by the sampling rate in that specific experiment (Fourier limit) and no upper limits which cover necessities of the IMS as well as SMS. One of the experiments with a Schottky detector at ESR is shown in Fig. 1.2.

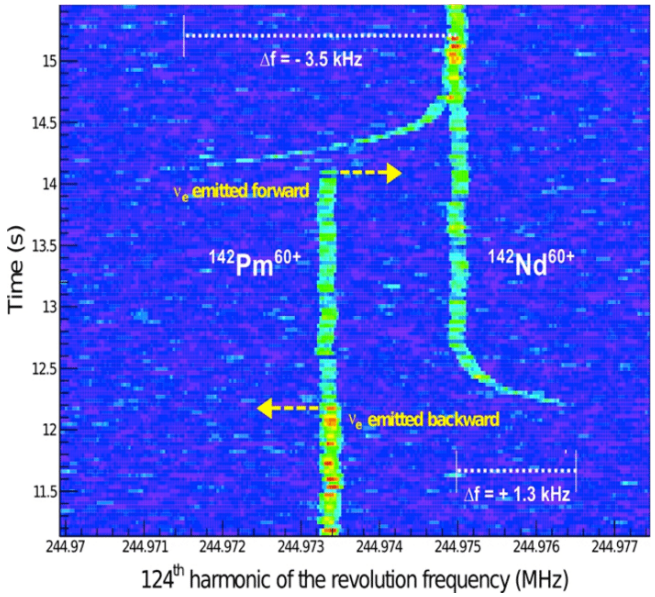

Fig. 1.2: Illustrarion of β^+-decay of $^{142}Pm^{60+}$. Picture taken from [23].

As one can see, during the experiment [23] a 245 MHz Schottky resonator allowed observation of the EC-decay of $^{142}Pm^{60+}$ with a time resolution of 32 ms and frequency resolution of 31.25 Hz.

1.3.1 Schottky Mass Spectrometry

Walter Schottky discovered a new kind of noise during studies of electron current in a vacuum tube [24]. This noise was caused by the finite amount of randomly distributed electrons in the current. In modern SMS noise caused by the ion beam in a storage ring couples with the pickup in a non-interceptive way (this process will be covered in Chapter 2), propagates through the amplification chain and is analyzed in the frequency domain. The most important values which one could get from the Schottky noise is the revolution frequency of the ions and their corresponding momentum spread [25]. To improve the precision of mass-measurement, it is desired that ions in the ring must have low momentum spread which can be achieved by utilising laser cooling [26], the electron cooler [27, 28] or stochastic cooling [29, 30, 31].

1.3.2 Isochronous Mass Spetrometry

The above-mentioned methods for mass-spectrometry are useful only for relatively long-lived nuclei because the cooling process usually takes several seconds. This amount of cooling time is unacceptable for short-lived nuclei. Another possibility is to use isochronous mass spectrometry. In order to perform IMS, the storage ring must be calibrated so that the transition energy matches the relativistic factor of the given species. For the ions that fulfill the condition of the isochronocity ($\gamma = \gamma_t$) change of their velocity will be compensated by changing their orbit, leading to the conservation of the revolution frequency [32]. However, during the IMS the dispersion function is larger which decreases momentum acceptance of the storage ring up to one order of magnitude in comparison to the SMS [33]. In 2011 two different ions were stored and measured by means of IMS. An illustration is given in Fig. 1.3.

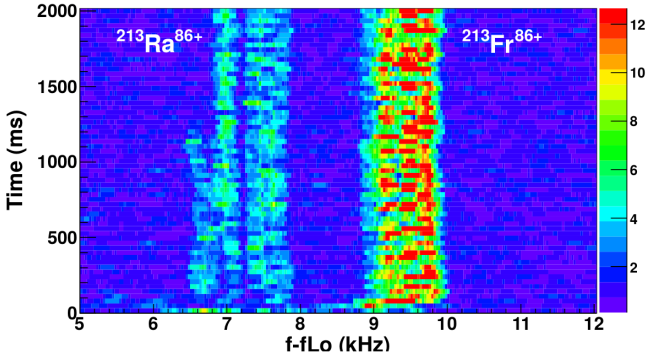

Fig. 1.3: Frequency dispersion of two species $^{213}Ra^{86+}$ and $^{213}Fr^{86+}$, which are injected into the ESR operated in isochronous mode. Local oscillator frequency here is 245.9245 MHz. Taken from [34].

From this figure it is clear that the resolution of the Schottky detector is sufficient to resolve similar ion species despite the larger dispersion introduced with IMS.

1.3.3 Anisochronism Effect and its Corrections

From the isochronicity condition $\gamma = \gamma_t$ one can see that this condition could be satisfied only for a certain species because the velocity of the particle depends on its mass and charge. This causes so-called anisochronism effect [35]. This effect makes peaks broader in the frequency domain and if the ion relativistic factor is too far from the transition energy this effect can even distort the Gaussian shape of the peak [36]. This means that precision measurements in isochronous mode demand corrections for the anisochronism effect. The main contributors to the anisochronism effect are imperfections of the ion optics and the range of mass-to-charge ratios of the ion species stored in the ring [37]. The revolution times for all other ions which do not fulfill isochronicity conditions will be smeared due to the momentum spread. Some other distortions in ion distribution can be caused by the production and transmission processes. One technique to reduce the range of injected ions is to filter incoming ions by their magnetic rigidities by installing a slit in a dispersive location prior to the injection into the ring. Despite the fact that this method decreases the transfer efficiency it was successfully tested at ESR, increasing mass-resolving power by up to one order of magnitude and doubling accuracy [35]. Another approach is to measure the speed of each ion together with its revolution time [33]. It was implemented in CSRe using the two time-of-flight (TOF) detectors. This method does not decrease the transmission efficiency and has an advantage in the case of experiments with nuclei with very low yields.

1.4 Motivation

The results achieved using the ESR Schottky cavities inspired the idea of cavity-based anisochronicity correction. A position-sensitive cavity that is placed at the location with the largest horizontal dispersion can record information about the ion orbits which will allow it to distinguish their magnetic rigidities. According to the definition of the magnetic rigidity $B\rho$ (1.2) if one measures the magnetic rigidity of the particle and its mass-to-charge ratio its speed can be calculated. Consequently anisochronisity correction can be applied using the position-sensitive and intensity-sensitive cavities.

$$B\rho = \gamma v \frac{m}{q} \tag{1.2}$$

Equation 1.2 shows the definition of $B\rho$. Here, B is a magnetic field of the dipole magnet and ρ is a gyroradius of the particle, which can be measured using the position-sensitive cavity.

The advantage of the cavity doublet is its non-interceptive beam interaction which leads to fewer losses of particles and allows for simultaneous measurement of the particle's lifetime. The efficiency of the TOF technique can also be strongly suppressed by several ions passing the foil at once because the arrival time of each ion is extremely difficult to to identify from the superposed multi-particle signal [38]. A very intense beam can even destroy the foil. These restrictions are not applicable to the cavities. This allows them to be used in high-intensity beams to take advantage of the greater yield. To surpass the limits of the double-TOF technique, the feasibility of using a cavity doublet for the isochronous mass measurements has been explored. The principle of the position detection using a cavity and the method of correction for the anisochronism effect were investigated in [39, 40] and [41]. In this work, we made simulations and design of a position-sensitive cavity doublet for the Rare-RI ring in RIKEN. The very first test of the Software-Defined Radio (SDR) as a data acquisition system (DAQ) for future Schottky cavities has been conducted in this work. Additionally, we simulated, designed, constructed, manufactured, and tested a smaller position-sensitive cavity doublet together with its DAQ based on SDR, both in the lab and at S-DALINAC at Darmstadt Technical University. All of these topics will be covered in corresponding chapters.

2 Theoretical Description

When charged particles travel through the beam pipe the time and position dependent electromagnetic field is produced. This field induces mirror charge distribution on the pipe walls which travels with the particle due to the high conductivity of the beam pipe material. A flat pipe has a small quality factor(Q-factor), approximately defined as the ratio of the initial energy stored in the resonator to the energy lost in one cycle of oscillation which means that the charge density fluctuations caused by the particle dissipate much faster than the period of particle revolution. This approach finds its place in beam position detectors such as parallel plates. However, the sensitivity of parallel plates is not sufficient for precision mass-spectrometry. If we introduce a structure with a high quality factor, such as a cavity detector, in the beamline, a portion of the beam energy will be trapped in the form of oscillations of the surface charge density; this can be investigated using Fourier analysis. Detailed theoretical description of the beam-cavity interaction is given in [39] and [42]. An ideal model of the cavity is a space enclosed by conducting walls that confine electromagnetic fields (EM-fields) inside. Usually, cavities consist of a prismatic shape of different cross-sections (cylindrical, elliptical, rectangular, etc.). In contrast to the ideal mathematical model, a practical cavity contains a hollow segment designed to match the beam-pipe aperture, allowing the beam to travel through without interruption. Additional objects which have to be taken into account are couplers, tuners, and detuners (if necessary). These cavities are often called radio frequency (RF) cavities and are essential components within experimental nuclear physics facilities. Their task is to interact with the beam using electromagnetic fields. There are many different classifications of cavities around the world, categorised based on their wave modes, the orientation of the energy flow through the couplers, conductivity, and so on. In this work, we will concentrate on a cavity that can be used as a position-sensitive detector. This necessitates a standing wave cavity utilising a fundamental TM mode, described further in section 2.1

2.1 Electrodynamics of a Cavity

Before introducing the complicated structure of a cavity let us review a simpler model. Firstly, we will assume that the cavity is fuly enclosed. Then, according to the classical electrodynamics, EM-field distributions will be described by the homogeneous Maxwell's equations

$$\nabla \cdot \vec{E} = 0 \tag{2.1}$$

$$\nabla \cdot \vec{H} = 0 \tag{2.2}$$

$$\nabla \times \vec{E} = -\mu_0 \frac{\partial \vec{H}}{\partial t} \tag{2.3}$$

$$\nabla \times \vec{H} = -\epsilon_0 \frac{\partial \vec{E}}{\partial t} \tag{2.4}$$

Here $\vec{E}$ is the electric field, $\vec{H} = 1/\mu_0 B$ is the magnetic field, ϵ_0 is an electric permittivity in vacuum and μ_0 is a magnetic permeability in vacuum. To set the boundary conditions we

assume that the electrical conductivity of walls is zero. This gives us:

$$\vec{n} \times \vec{E} = 0 \tag{2.5}$$

$$\vec{n} \cdot \vec{H} = 0 \tag{2.6}$$

where $\vec{n}$ is the normal vector to the boundary. Writing general solutions for the EM fields inside even a simple cavity is a challenging task. However, taking into account the linearity of Maxwell's equations one can use the superposition principle which states that every linear combination of solutions is also a valid solution. By knowing this, one can use only the simplest solutions for the simple shapes (for example cylindrically-symmetrical) which are named modes or eigenmodes. Later on, any solution can be expressed by using a proper superposition of these modes [43]. As stated before, we will work using the fundamental TM mode, meaning that the longitudinal component of the magnetic field vanishes. At the same time, the longitudinal component of the electric field is large and has a strong coupling with the beam. The boundary conditions (2.5) and (2.6) demand that for the standing wave inside the cavity volume the electric field must be perpendicular to the wall, whereas the magnetic field has to be tangential. For cases which cannot fulfill these requirements, oscillations will be strongly damped and no standing wave will exist. Because of this, only modes with certain frequencies can survive in the cavity for a sufficient time and these frequencies are defined by the geometry of the cavity. The electric field oscillates synchronously with the magnetic field which is phase shifted by $\pi/2$. Energy is transferred between these two fields so that the total energy of the field is conserved. These oscillations could be infinite if there were no losses in the cavity walls which will be discussed below.

The cavity can contain different oscillation modes. We are interested in the first two modes: the monopole and dipole mode. The monopole mode of a typical cylindrical Schottky cavity is more strongly excited whereas the dipole mode allows for position measurements due to its spatial distribution. Illustrations are given in Chapter 7 in Fig. 7.4 and Fig. 7.5. In this work we are suggesting to use the monopole mode of an elliptical-shape cavity for performing the position measurements.

2.2 Shunt Impedance

The cavity material has finite conductivity, which means that power dissipation in the cavity walls is unavoidable. To take these losses into account we introduce an effective shunt impedance. According to [43] it is defined as:

$$\hat{R}_{sh} = \frac{|U_{acc}|^2}{P_{diss}}, \tag{2.7}$$

where P_{diss} is a power, dissipated on the walls of the cavity, and U_{acc} is the acceleration voltage across the cavity gap. This voltage is the one a particle sees when transiting through the cavity [44]. The oscillation of the EM field inside the cavity has to be taken into account because these oscillations have a much higher frequency than the revolution frequency of the particle and the longitudinal component of the electric field $\vec{E_z}$ could be directed opposite to the direction of the particle momentum. To describe this effect we can calculate the U_{acc} as integral of the $\vec{E_z}$ over the cavity depth d:

$$U_{acc} = \int_{-d/2}^{d/2} \vec{E_z}(x) e^{-i\omega_0 t}\, dz \ , \tag{2.8}$$

where ω_0 is the first resonant frequency.

In reality, EM-fields do not vanish immediately on the cavity borders. Due to the aperture of the beam pipe, they may propagate a small distance into the beam pipe, potentially interacting with the EM-field of another accelerator element. This is an important effect which will be described in detail in Chapter 3. Strictly speaking, integral borders have to be from $-\infty$ to $+\infty$, but one can choose an arbitrarily distant point from the cavity borders where EM-fields extensions are negligible. The longitudinal component of the electric field $\vec{E}_z$ is also position-dependent, as is $\hat{R}_{sh}$.

The total energy stored in the mode is described as [40]:

$$W = \frac{W_{max}}{4Q_0^2(\delta\omega/\omega_0)^2 + 1}, \tag{2.9}$$

where W_{max} is the maximum energy of the EM field. Equation (2.9) defines the resonance curve of the cavity which is a Lorentzian distribution with width $\delta\omega$ centered at ω_0.

One of the most important parameters of the cavity is its quality factor, Q_0. This value shows the ability of the oscillating system to preserve the stored energy [45]. It can be described as:

$$Q_0 = \frac{W}{T_0 P_{diss}} = \frac{\omega_0 W}{P_{diss}}, \tag{2.10}$$

where T_0 is a period of one oscillation, and P_{diss} is amount of power which has been dissipated on the cavity walls and can be expressed as $P_{diss} = -dW/dt$. There are three types of quality factors of the cavity. The described above unloaded quality factor Q_0 is a quality factor for a standalone cavity. The loaded quality factor Q_l is a quality factor of the cavity connected to the readout electronics, for example network analyzer. External quality factor Q_{ext} is a value which shows degradation of the unloaded quality factor due to the connected electronics. In this chapter we will use the unloaded quality factor Q_0. All these values are connected with a simple equation:

$$\frac{1}{Q_l} = \frac{1}{Q_0} + \frac{1}{Q_{ext}}. \tag{2.11}$$

A more detailed description of the quality factor concept related to the cavities can be found in [46]. The unloaded quality factor Q_0 of the cavity can be described as the relation between the resonant frequency (frequency of the point of the largest amplitude on the peak) and full width at half maximum of that peak:

$$Q_0 = \frac{\omega_0}{\Delta\omega_{FWHM}}. \tag{2.12}$$

However, if this plot is received not from the numerical calculations but from the real measurement device, then this equation will give us the loaded quality factor Q_l if we know the coupling factor.

In order to describe the asynchronism effect of the cavity on a particle, we will use a transit time factor τ. It is defined as the modulus of the acceleration voltage normalized to a a theoretical case where the particle sees a static electric field [44]:

$$\tau = \frac{|\int_{-d/2}^{d/2} \vec{E}_z e^{-i\omega_0 t}\, dz\,|}{\int_{-d/2}^{d/2} \vec{E}_z\, dz}. \tag{2.13}$$

We consider that for a simple mode, such as the monopole or dipole mode, $\vec{E}_z$ is uniform in the longitudinal direction and thus (2.13) will look as:

$$\tau = \frac{T_0}{\pi t_{tr}} \sin\left(\frac{\pi t_{tr}}{T_0}\right), \tag{2.14}$$

where $T_0 = 2\pi/\omega_0$ is the oscillation period of the EM-field and t_{tr} is the time needed for the particle to transit through the cavity. Illustration of equation (2.14) is given on Fig. 2.1

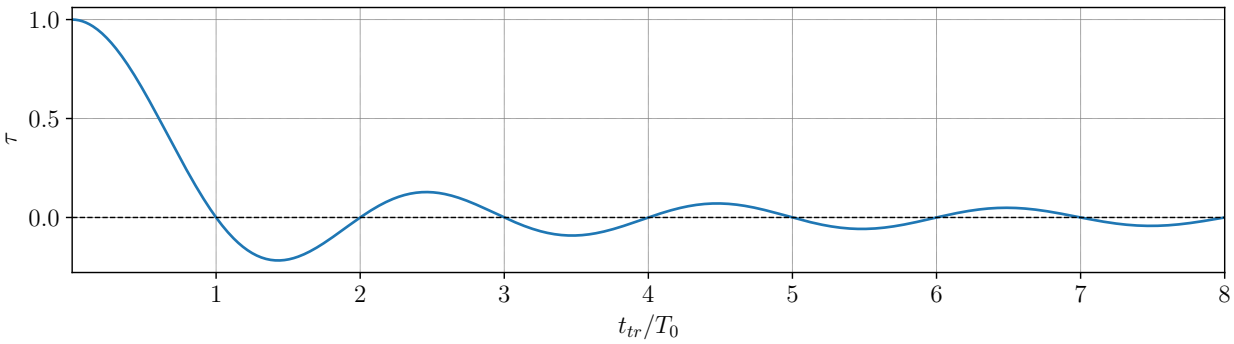

Fig. 2.1: Dependency of the transit time factor of a cavity on the normalized transit time of a particle

According to Fig. 2.1, for short transit times, the transit time factor is close but never equal to 1 which means higher efficiency of the interaction between the particle and EM-field inside the cavity. A negative transit time factor results in a decceleration of a particle. To achieve short transit times for a greater transit time factor τ, the cavity must be "thin" along the axis of the beam pipe.

Combining equations (2.7), (2.8) and (2.13) gives us an equation which connects effective shunt impedance with transit time factor:

$$\hat{R}_{sh} = R_{sh}\tau^2 \tag{2.15}$$

where the shunt impedance R_{sh} is defined as

$$R_{sh} = \frac{\left(\int_{-d/2}^{d/2} \vec{E}_z \, dz\right)^2}{P_{diss}} \tag{2.16}$$

From (2.16) one can see that R_{sh} depends mainly on the cavity geometry, whereas $\hat{R}_{sh}$ depends also on the velocity of the particle because of the transition time factor. To compare different cavities one has to use a quantity that does not depend on the losses in the material: this is the characteristic shunt impedance R_{sh}/Q_0, which depends only on the cavity geometry. It describes the coupling strength between the beam and EM-field inside the cavity in terms of energy transfer [40]. The characteristic shunt impedance R_{sh}/Q_0 is expressed as:

$$\frac{R_{sh}}{Q_0} = \frac{\left(\int_{-d/2}^{d/2} \vec{E}_z \, dz\right)^2}{W\omega_0} \tag{2.17}$$

2.3 Couplers and Coupling Factor

Oscillations of the EM-field inside the cavity are enclosed by the walls of the cavity. To read the information about interaction between the beam and the field inside the cavity one has to introduce a coupler which will connect the EM-field oscillations to the readout electronics. There are three kinds of couplers: an electric coupler, a magnetic coupler and a waveguide [47]. Depending on the frequency and power of the oscillations different coupling schemes are used. In case of low frequency and low power, a coaxial line (electric or magnetic coupler) can be

used. For high powers or high frequencies waveguides are instead utilised. An illustration of different coupling systems are shown in Fig. 2.2 :

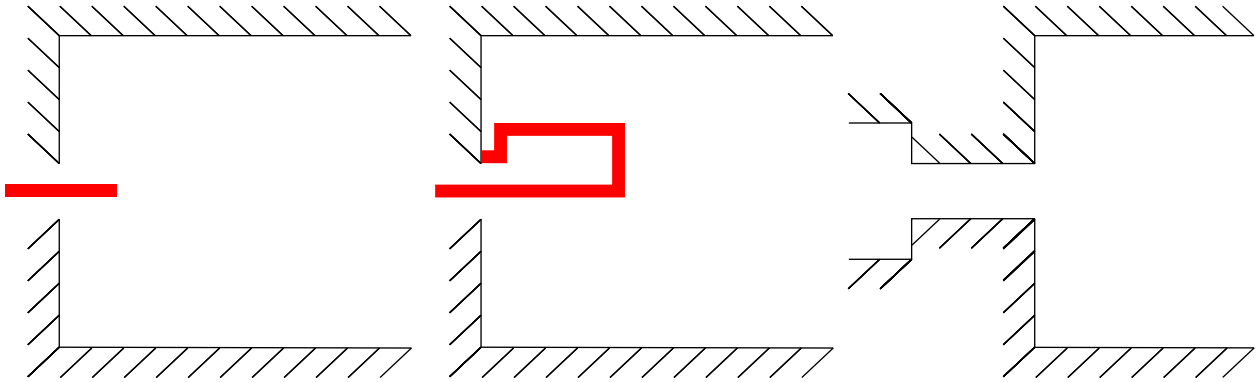

(a) Electric coupler (b) Magnetic coupler (c) Waveguide

Fig. 2.2: Different types of power coupling systems.

An electric coupler usually consists of a small probe which interacts with the electric field of the cavity. The electric field generates a signal in the probe, causing a potential difference between the connected signal and ground wires. The amplitude of the generated signal will be proportional to the electrical field intensity at the point of the electrical coupler placement. To collect the necessary information from the dipole mode, the electric coupler must be installed on the face of the cavity at the point where the intensity of E_z is the largest. An illustration of the cavity which utilizes all three kinds of couplers is shown in Fig. 2.3:

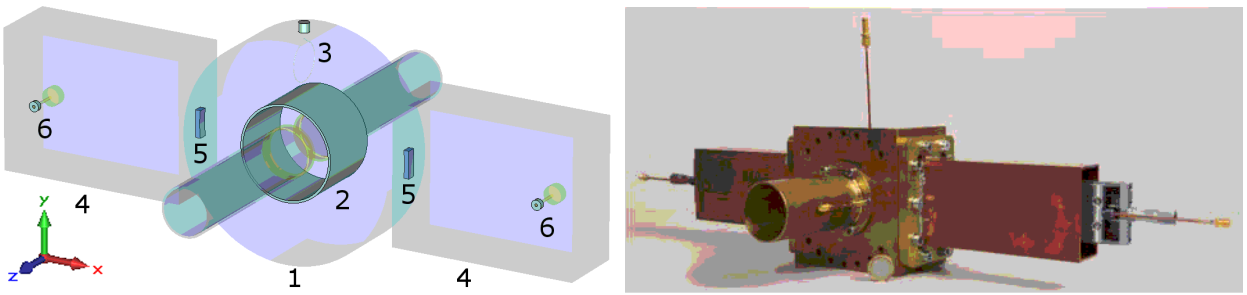

(a) Electric coupler. (b) Magnetic coupler.

Fig. 2.3: An example of utilizing of the different types of power coupling systems. 1-pillbox cavity, 2-ceramic vacuum shielding, 3-magnetic coupler, 4-waveguide structures, 5-coupling slots, 6-electric couplers. Picture taken from [48].

A magnetic coupler is a loop of conductive material which is placed inside the cavity with one end connected to the body and another one to the readout electronics signal wire. The signal in this coupler is created by the oscillations of the magnetic field flux through the area under the loop. This change in flux will induce a current in the loop which is proportional to the changes of the magnetic field flux, leading to a change in potential difference between the signal wire and grounding. Their arrangement must be in a place where the flux of the magnetic field through the area under the loop will be the largest. However, introducing too much metal into the cavity volume will lead to the the redistribution of EM-field modes within the cavity, possibly leading to large distortions of the signal. The best case for the cavity, which should generate the necessary information using the monopole mode, is a coupler with a small loop placed at the point on the side wall which is the farthest away from the beam pipe aperture. We used this approach in [22, 39] and our test setup which will be described in Chapter 5. In

our case of the fundamental TM mode standing wave cavity we are using this kind of couplers which will be described in Chapters 3 and 5.

An electromagnetic coupler interacts with electric and magnetic fields simultaneously and is usually an aperture in the cavity wall which connects the cavity and a waveguide. It is mostly used for accelerating cavities due to the large amount of energy needed for their proper operation.

To describe the efficiency of the energy transfer between the EM-field inside the cavity and readout electronics one can use a so-called coupling coefficient κ. It can be expressed as $\kappa = P_{ext}/P_{diss}$ where P_{ext} is the power loss in the coupler and the following readout electronics. If these two power losses are equal then the power taken by the coupler is the same as the power dissipated in the cavity walls, no reflection of the incident waves happens and the maximum power goes to the readout circuit. Other than that, overcoupling and undercoupling can be differentiated for $\kappa > 1$ and $\kappa < 1$, respectively [47]. To satisfy this condition for a magnetic coupler, one can rotate it to change the flux of the magnetic field through the area of the loop or change the size of the loop itself. In this work and in [22] we rotated the couplers to achieve $\kappa = 1$

2.4 Tuning and Detuning

The beam in a storage ring usually contains ions of different species. Each of them has its own revolution frequency f_i which depends on its mass-to-charge ratio $[m/q]_i$ according to equation(1.1). The resulting spectrum contains peaks of the revolution frequencies of the ions together with their harmonics. A resonant Schottky cavity could be imagined as a band-pass filter for this signal. It filters all frequencies except for those close to the resonant frequency of the given mode of the cavity. For example, the new resonant Schottky cavity at ESR has the resonant frequency of 407 MHz, which allows for the measurement of the 245th harmonic of the revolution frequencies of the stored ions. Due to the narrow band nature of cavity resonators, it simultaneously covers only a part of the frequency acceptance of the ring [22]. For this reason, a mechanism which allows manipulation of the filtering properties of the cavity is needed. There are two different approaches:

- Changing the resonant frequency by introducing the metallic plungers of different shapes to change the geometry of the field and thus vary the resonant frequency of the desired mode.
- Decreasing the loaded quality factor and shunt impedance of the cavity without changing the characteristic shunt impedance which leads to a decrease in sensitivity of the cavity but increased bandwidth of the band pass region.

In our work we developed and tested a new shape of tuners which will be discussed in Chapters 3 and 5. In [22] both approaches were used simultaneously. The result of introducing the tuner will be shown in Chapter 5.

2.5 Signal from the Cavity

Consider particles circulating in the storage ring. One can say that these particles create a current. If there is only one particle in the ring we can talk about the instant current value, but usually the storage ring has the large number of particles which have a momentum spread. Such situation demands using the mean current instead of the instant current to describe the

signal in a Schottky cavity. This idea is well described in [49]. The equation for the mean square current contained in the h^{th} harmonic is:

$$\langle I_h \rangle^2 = 2(Ze)^2 f_0^2 N. \tag{2.18}$$

Here e is the elementary charge of electron, Z is the charge state of a particle, f_0 is the revolution frequency and N is the number of particles which rotate with frequency f_0. As one can see from equation (2.18), power which is contained in the Schottky band remains the same for every harmonic. But we also know that the width of the Schottky band increases proportional to the harmonic number, and thus the amplitude must decrease with $1/h$. Now let's assume that there are many particles in the storage ring and they have a momentum spread defined by the ring parameters. This means that they will have frequency spread $f_0 \pm \Delta f/2$. For a subgroup of the particles over a very narrow range df_r the total number of particles N turns into $dN/df_r \cdot df_r$. Therefore, the equation of the mean square current spectral density for the given Schottky harmonic number h and the bandwidth Δf will be

$$\frac{d\langle I_h \rangle^2}{df_r} = \frac{2(Ze)^2 f_r^2 N}{h\Delta f}. \tag{2.19}$$

When the beam passes through the cavity a portion of its power remains inside. In this case the beam plays the role of a stiff current source. A good description of the system with a beam, a cavity and a measurement device is shown in Fig. 2.4:

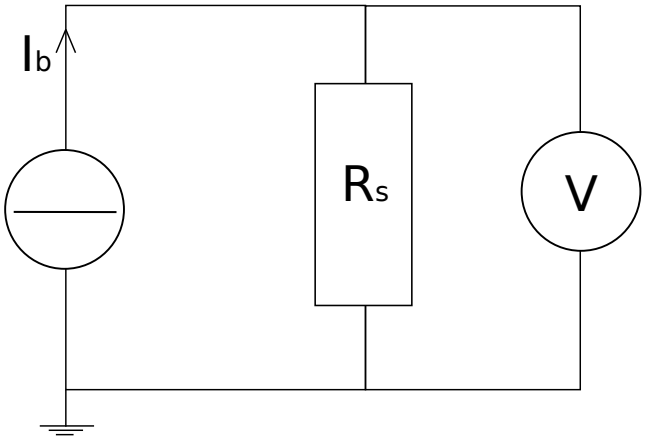

Fig. 2.4: Electric circuit for the system with a beam as stiff current source, a cavity as a resistor and a measurement device as the voltmeter.

Here I_b is the current generated by the stiff source, the resistor R_s is the shunt impedance of the cavity which already takes into account the transit time factor, Λ_β [39], the voltmeter V is a measurement device: an oscilliscope, a network analyzer or a software defined radio (see Chapter 4). A power stored in the circuit will be $P = I^2 R_s$. For Gaussian-like peaks with the same full width at half maximum and total area, the height of the signal power peak can be obtained by multiplying the expression for power, P, by the factor of $2\sqrt{\ln 2/\pi}$. Taking (2.19) into account, the equation for the power spectral density of a signal for a given Schottky harmonic number h and the bandwidth Δf can be written as

$$\frac{d\langle P_h \rangle}{df_r} = 2\sqrt{\frac{\ln 2}{\pi}} \frac{2(Ze)^2 f_r^2 N}{h\Delta f} R_s \tag{2.20}$$

To estimate the power of the signal from the particles delivered to the Schottky cavity, let's assume that a proton passes through the cavity with quality factor of $Q_0 = 2000$ and resonant frequency of 410 MHz with revolution frequency of 1,7 MHz at a place where $R_{sh}/Q_0 = 120$

Ohm/m. Then, according to equation(2.18) a power of the signal in one frequency band will be:

$$\langle P_h \rangle = 2(Ze)^2 f_0^2 N \frac{R_{sh}}{Q_0} \cdot Q_0 = -165 \text{ dBm} \tag{2.21}$$

The estimated power of the signal in one frequency band from the $^{235}U^{92+}$ ion will be about -125 dBm. Now we assume that the frequency band has a width of 50 Hz and all peaks are Gaussian. The total power delivered to the frequency band will result in an area under the peak. The height H and its full width at half maximum (FWHM) of the Gaussian peak are connected with its area S as $S = 1.064 \times H \times FWHM$ From this equation we can calculate the maximum peak power. It will be -182 dBm for the proton and the uranium will be - 143 dBm.

2.6 Correction for the Anisochronism Effect

Equation (1.1) defines the dependency of the frequency difference Δf_{rev} on the mass to charge ratio $\Delta(m/q)$ of the ions of different species. Each term has its own uncertainty which leads to the error of the mass measurement. The relative spread $\delta f_{rev}/f_{rev}$ (linewidth) of the revolution frequency distribution of each beam component is only determined by the velocity spread $\delta v/v$ of the corresponding ion ensemble and is given by [25]:

$$\frac{\delta f_{rev}}{f_{rev}} = \left(\frac{1}{\gamma^2} - \frac{1}{\gamma_t^2} \right) \frac{\delta v}{v} \tag{2.22}$$

whereas the peak position is defined by the mass-to-charge ratio of the particle. δf means the uncertainty of this position is defined by the full width of this peak at its half maximum height (FWHM).

While measurements in the standard mode utilize the electron cooler which decreases the momentum spread of particles in the ring, the isochronous mode measurements have to deal with larger momentum spreads due to absent cooling. On the one hand, the standard mode is helpful because it is possible to conduct very precise measurements with the narrowest peak shapes if the measurement time is sufficient. On the other hand, the isochronous mode measurements are better for short lived nuclei or isomeric states. These measurements can also be conducted with TOF detectors, but the idea of isochronous mass-spectrometry with Schottky detectors is to combine the best of the two approaches and enable lifetime measurements. For this reason we need a fast and sensitive detector, conditions fulfilled by the resonant Schottky cavities. And in order to increase the measurement sensitivity we also compensate for the velocity spread [1, 50].

During operation of the storage ring in the isochronous mode, each particle moves at a constant speed along its own trajectory. The momentum difference for the same ion type is compensated by the length of trajectories. An ideal particle which fulfills the isochronicity condition will always stay on the same trajectory and its revolution frequency will always be the same. However this condition can only be fulfilled with some error, meaning that every revolution of this particle will change a little and this will smear the peak in the frequency domain. The larger the difference between the Lorentz-factor of the particle γ and the transition energy γ_t, the larger the smearing, which will lead to a larger uncertainty in the mass-measurement. In this work we describe a method which allows one to decrease the uncertainty caused by the anisochronism effect.

Let's assume that we have one non-isochronous ion named "ion A" in the ring. Fig. 2.5a illustrates some possible trajectories of the ion. We envelope these trajectories with two lines to

illustrate the amount of space in the horizontal plane along the beam path δx_A, which contains all possible trajectories of this ion. Now we introduce an "ion B" which is slightly closer to the isochronous condition. As one can see from Fig. 2.5b it has a smaller envelope and both particles can fly inside the δx_B envelope. Then we introduce an isochronous "ion C" which follows almost the same trajectory every time (Fig. 2.5c). In this configuration the information about the transversal ion position is useless. However if we look at the particle trajectories in the dispersive section (for example, after a dipole magnet), we will see that envelopes of the same species trajectories are separated from each other. Illustration is given on Fig. 2.5d.

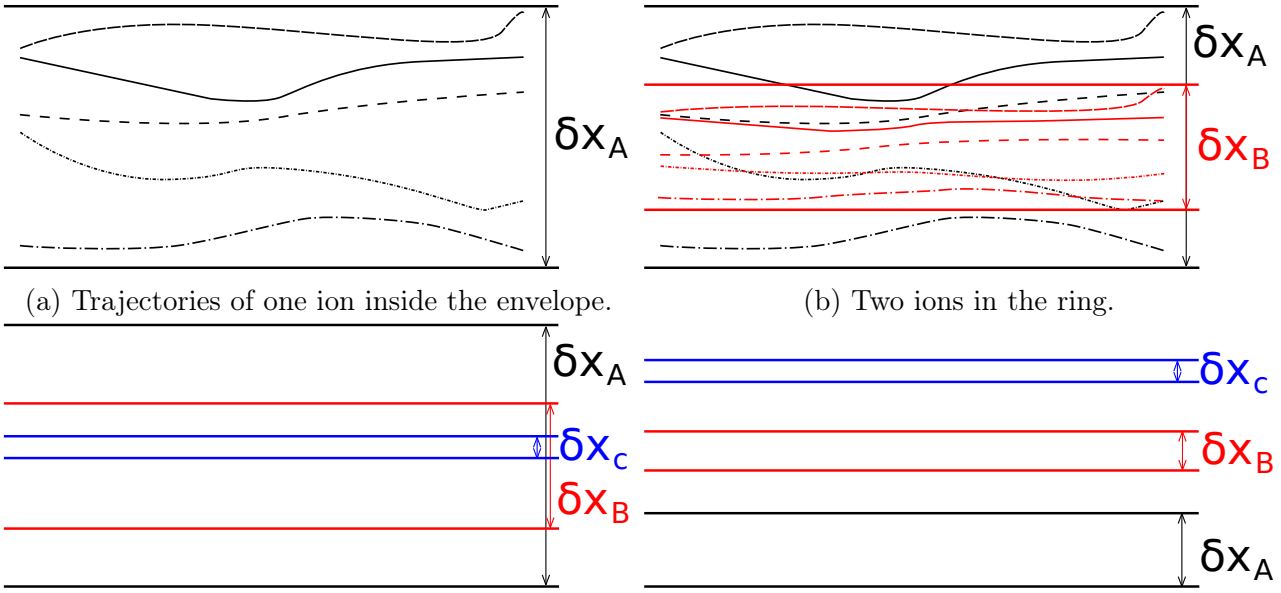

(a) Trajectories of one ion inside the envelope.

(b) Two ions in the ring.

(c) Anisochronous ion in the ring.

(d) Dispersive section.

Fig. 2.5: Schematic of the trajectories enveloping for ions with different γ.

From equation (1.2) we know that the position of the particle depends on its magnetic rigidity. The magnetic rigidity and γ are known from the ring parameters, whereas mass-to-charge ratio can be defined from (1.1). The main error in (1.1) is an error in the velocity δv [25]. As one can see from Fig. 2.5d, the dispersive section of the ring allows for an unambiguous position measurements of certain species, decreasing the uncertainty of the frequency measurements to the uncertainty of the position measurements with known coefficient which is less than the uncertainty in frequency measurements. In this section the position x corresponds to the gyroradius ρ, and we have:

$$\delta v = \delta\rho \frac{B \cdot q}{\gamma \cdot m} \tag{2.23}$$

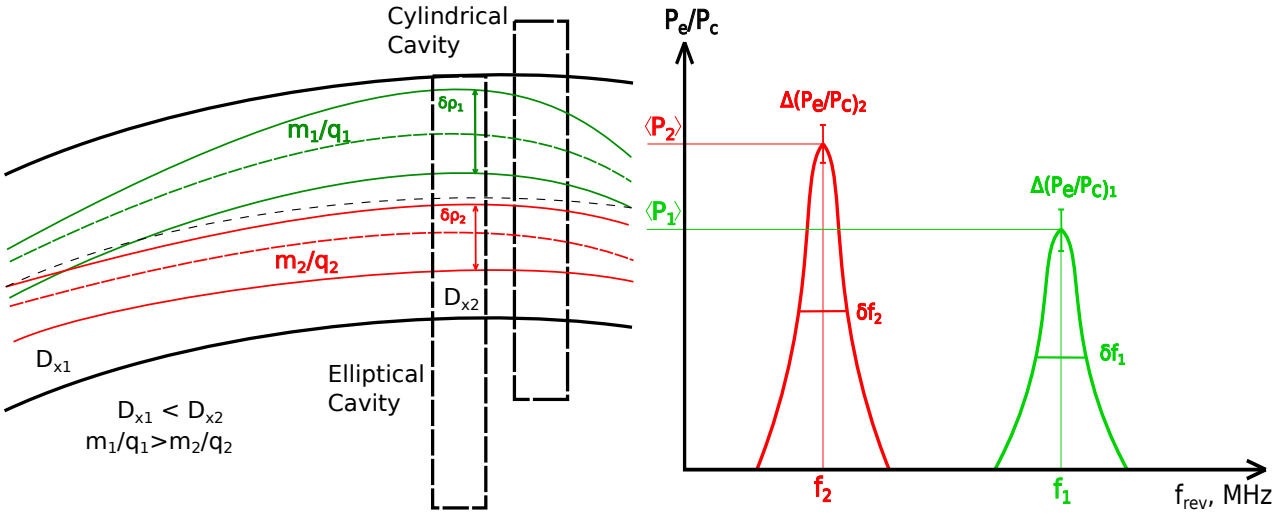

(a) Schematic illustration of particle trajectories in a dispersive section.

(b) Amplitude dependency on the particle position: the average power of the height of the peak corresponds to the centroid of the position.

Fig. 2.6: Two different anisochronous ions in a storage ring at a dispersion section. Dashed lines are the average centers. The amplitude of the peak corresponds to the center coordinate according to the responding function of the position-sensitive cavity (see 3).

As one can see from Fig. 2.6 a position-sensitive Schottky cavity doublet generates a signal whose power is dependent on the particle position. Using this method one can reduce the uncertainty, equal to one FWHM of the given peak spread of the amplitude of the signal at the central frequency of the peak (we assume that every peak has Gaussian shape) at different moments in time. One can distinguish the mass-to-charge ratio of the particles based on the central frequencies of the peaks with an uncertainty which has been discussed before. Different species will be distinguishable as long as the frequency difference Δf is larger than FWHM of the peaks. As an example of the two well distinguishable peaks, one can use the picture from the ^{72m}Br measurements we have conducted at ESR. This experiment with code name E143 was aimed at conducting a measurements of the short-lived isomeric states such as isomeric state of ^{72m}Br utilizing the isochronous mode.

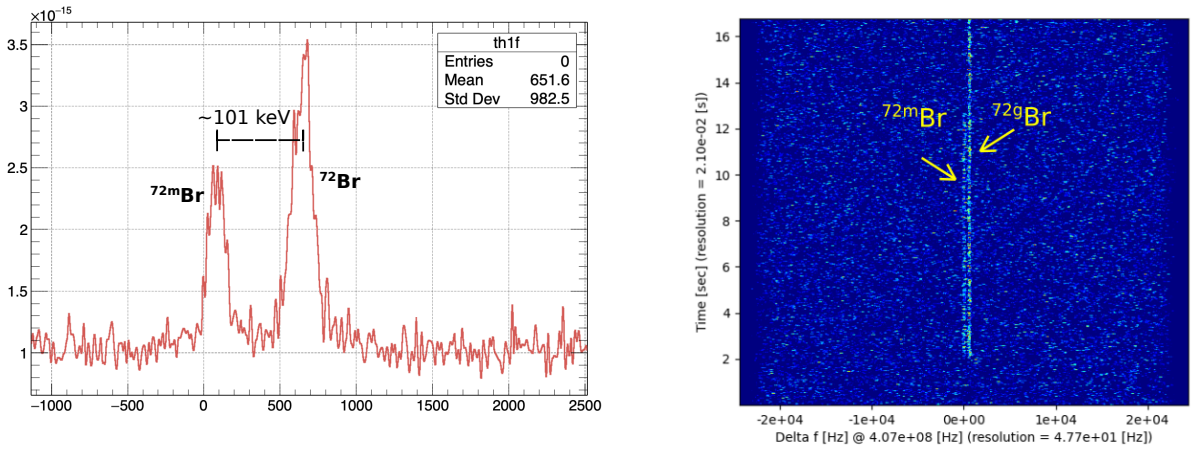

Fig. 2.7: Measurements of the 101 keV isomeric state of the one ^{72m}Br ion.

From Fig. 2.7 one can clearly see the two peaks with Δf almost 3 times larger than their FWHM which corresponds to the 101 keV difference in mass of a single ^{72m}Br ion. This spectrum shows the sensitivity and resolution of resonant Schottky cavities.

When we obtain the amplitudes of the peaks which correspond to the different ion species, we can distinguish their positions in our position-sensitive detector by applying the detector response function. In this function every amplitude of the peak corresponds to some position of the ion inside the detector after the normalization of the amplitude. The power of the signal which will enter the data acquisition system can be defined as

$$\frac{d\langle P_h\rangle}{df_r} = \beta_{c,e}\frac{d\langle P_{h0}\rangle}{df_r}$$

Here β_c is the coupling coefficient for the cylindrical cavity and β_e is the coupling coefficient for the elliptical cavity.

The normalization is done bin by bin division power of the signal from the elliptical cavity on the power signal from the cylindrical cavity. This allows us to get rid of all factors which are not position-dependent, such as charge, momentum spread and so on.

$$\frac{d\langle P_{he}\rangle}{df_r}\frac{df_r}{d\langle P_{hc}\rangle} = \frac{R_{se}\beta_e}{R_{sc}\beta_c} \tag{2.24}$$

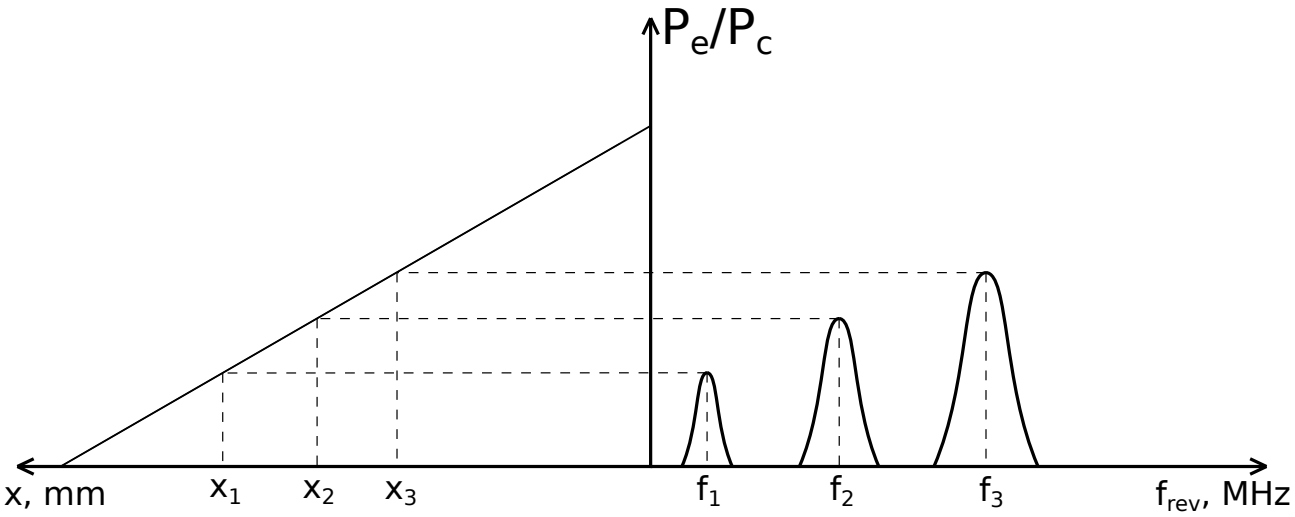

Fig. 2.8: Schematic illustration of the relation between the normalized amplitude of the peak in frequency domain and correspondent particle position. The inclined line on the left is explained in Chapter 3.

In order to have the unambiguous dependency between the particle position and power of the signal one has to have a gradient of R/Q in some direction. The usual approach is to utilize the dipole mode of the cylindrical cavity. Illustration is given in Fig. 3.3. The main idea of this work is to design a cavity which will be position-sensitive and can be operated in the monopole mode. According to the Maxwell's solutions for the enclosed volume of a simple shape [40], the monopole mode is more strongly excited than the dipole mode which has been proven by simulations in Chapters 3 and 5. This leads to increasing the signal-to-noise ratio which in turn will decrease the uncertainty of the ion position measurements. We decided to go for an elliptical shape in order to keep the field gradient constant in the horizontal direction whereas changes of the R/Q values in vertical direction should be negligible. The illustration of the signal power versus position is shown in Fig. 2.8.

After this operation we will have two sets of data: revolution frequencies of ions and their corresponding positions. These two sets of data can be plotted together as illustrated in Fig. 2.9. Each set of points which corresponds to the same ion can be fitted linearly. From this linear fit one can have 4 parameters: slope, error of the slope, crossing of the co-ordinate axis and error in that crossing. In this work we are interested in the error of the slope, however the slope itself tells us about the dependency between the mass-to-charge ratio difference and the corresponding change of the anisochronous effect.

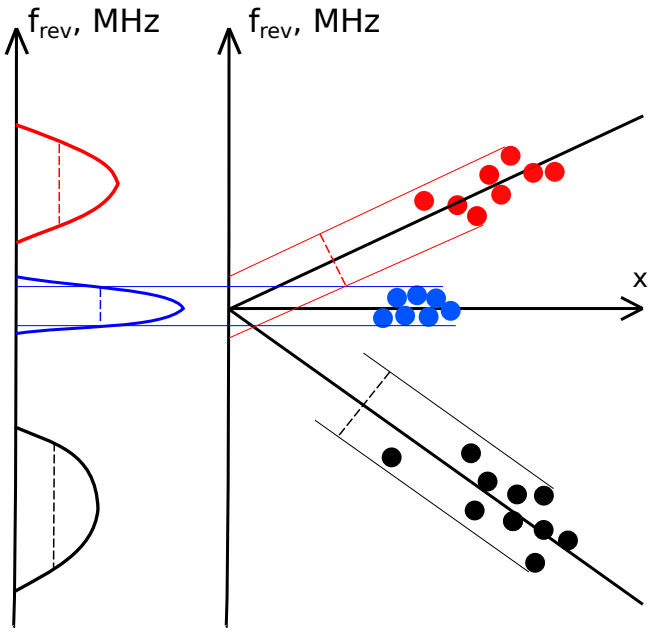

Fig. 2.9: The methods of decreasing the error of mass-to-charge ratio based on using the linear fit for the points which correspond to ions of the same kind.

The error of the slope tells us about the uncertainty of the frequency measurements which are independent of the ion's isochronicity. However, individual ions in a real storage ring are injected at different γ which do not perfectly match γ_t. Other factors such as closed orbit distortion, imperfections in the magnets and dispersion mismatching cause an additional frequency spread of δf [51]. With this method, the uncertainty of the frequency measurement for all ions of the same mass-to-charge ratio will be smaller than the initial uncertainty and equal to the uncertainty of the linear fit.

3 Design of a Position-Sensitive Cavity Doublet for R3 Ring

To create a suitable cavity, it is necessary that one has a detailed description of the section where it will be installed. Once this information is known, simulations may be conducted. In our case, the cavity will be installed in a straight dispersive section of the R3 storage ring at RIKEN. The position of the straight section is illustrated in Fig. 7.18a. An estimation of the sizes of the elliptical and cylindrical cavities is taken from the blueprints of this section, given in the Appendix in Fig. 7.18b.

The R3 ring consists of a cyclotron-like storage ring with circumference of 60.53 m specialized for isochronous mass spectroscopy of rare radio-isotope (RI) beams. It has a long injection line, which is necessary for individual injection and measurement of β with a relative accuracy of 10^{-4}. The beam energy of the R3 ring is designed to be around 200 MeV/u. The "cyclotron-like" storage ring can achieve the isochronous condition for large acceptances of $\delta x\prime = \pm$ 15 mrad and $\delta p/\mathrm{p} = \pm$ 0.5% [7].

In order to define the properties of the cavity as detector one has to know the distribution of the electromagnetic field inside. For this reason the R/Q map was calculated as well as the resolution map. All simulations as well as design were performed using CST Studio Suite 2020 [52]. There are several things which have significant influence on the field distribution and, as a result, on the resolving power of the position-sensitive cavity doublet. Influence of the pipe blending radiuses, blending radius of the connection between the beam pipe and the cavity wall, cavity extension and cavity geometry, tuners shapes and sizes have been studied in the present work. Each of these factors will be discussed in subsequent sections.

3.1 Mechanical Restrictions Based on the R3 Blueprints

As one can see from the blueprints, the inner part of the beam pipe has dimensions of 400 mm $\times$ 40 mm. This means that the elliptical cavity has to have a horizontal diameter of at least 800 mm. The distance between the floor and the center of the beam pipe is 1700 mm, so one can easily install there, for example, a 1800 mm in height cavity, because only half of this size will be between the beam pipe and floor.

A taller cavity will result in an elongation of the vertical field, leading to less error of the vertical position of the particle [39]. The elliptical cavity must have a linear gradient of R/Q in the horizontal direction in order to simplify data analysis. Extension of the field from the cylindrical cavity superposing with the elliptical position sensitive cavity will lead to deviations from the linear dependency of the R/Q value on the particle position. This is because components of these fields will have different amplitudes, phases and distributions in the volume which we want to use for positions measurements. Thus, superposition of these fields will lead to an increase of error in position measurement. Construction and installation of cavities and their elements should also be as simple as possible which means that there has to be enough space for the standard screws which will be used and for working with instruments such as keys or a network analyzer. In addition, tuners will be installed on the side of the elliptical cavity which will decrease the maximum possible dimensions.

To take these factors into account, simulations of a system which consists of consequent cylindrical and elliptical cavities were performed. The horizontal sizes of the cavities is also an important consideration because the installation section is in close proximity to a wall. We were informed that there is roughly 500 mm distance between the center of the beam pipe and the wall, so our cavities should be not bigger than 500 mm in the horizontal radius. One has also to take into account the extension of the cavity walls which is approximately 8 mm. Cylindrical and elliptical cavities were modeled according to these dimensions.

3.2 Field Propagation Simulations

Primarily, we must consider the cavity positions. There are two main restrictions other than the fact they must be situated in sequence. Firstly, cavities have to be as close as possible to each other in order to neglect the change of a particle position during flight through the system of both cavities. Secondly, the cavity is not a closed resonator but contains a beam pipe section, so the excited EM field inside the cavity will be extended along the beam pipe further beyond the cavity. This means that cavities have to be far enough from each other to avoid influence of an extension of the field from the cylindrical cavity to the field of the elliptical cavity. The R/Q value which describes intensity of the beam-cavity interaction depends on the Z-component of the EM field, E_z and this dependency is described by the equation (2.17).

We used a right-handed coordinate system where the Z-axis was pointed in the same direction as the particle momentum vector. It was suggested to model a cavity with an elliptical geometry and to use the monopole mode of the electromagnetic field for establishing the position of a particle along the X-axis. This has the additional benefit of decreasing the influence of the vertical position of the beam on the output signal [53, 54]. In order to normalize the signal from the position sensitive cavity one must use a cylindrical cavity, using this as a reference signal. These signals will provide information about mass-to-charge ratio whereas signal from the elliptical one will provide information about mass over charge ratio and particle position. Using both of these signals one can normalize signal from the elliptical cavity in order to identify positonal information independent of mass-to-charge ratio [40, 55].

To estimate influence of the field inside the cylindrical cavity on the resolution of the elliptical cavity, one must check the dependency of resolution map on the position along the Z-direction inside the cavity's beam pipe. Some high frequency waves from higher order modes can propagate through the beam pipe, because it works as a hi-pass filter. One can assume the beam pipe as a rectangular waveguide with defined geometry and its cutoff frequency can be defined from the next equation:

$$f_c = \frac{c}{2a}. \tag{3.1}$$

Here c is speed of light in the medium, a is a size of the larger side of the rectangular waveguide, f_c is a cutoff frequency, any wave with frequency lower than the cutoff frequency cannot propagate through the given waveguide. As far as we are interested in the lower order modes, such as the monopole mode, we can neglect the waves which flow through the beam pipe because their frequency is several times higher than frequency of the monopole mode which we want to use for position measurements. Additionally their energy is also much smaller as can be seen from the solutions of Maxwell equations for the EM wave inside the resonator: an amplitude of E_z oscillation is decreasing proportionally to $1/f_0$ where f_0 is a frequency of the given eigenmode. For the beam pipe with an outer width of 400 mm, height of 40 mm and wall thickness 2.5 mm, equation (3.1) gives the cutoff frequency to be $f_0 = 375$ MHz. Results of the simulation of an EM field inside the beampipe without cavities is given in Fig. 3.1.

Results of simulation of an EM field inside the beampipe without cavities is given on the Fig. 7.3

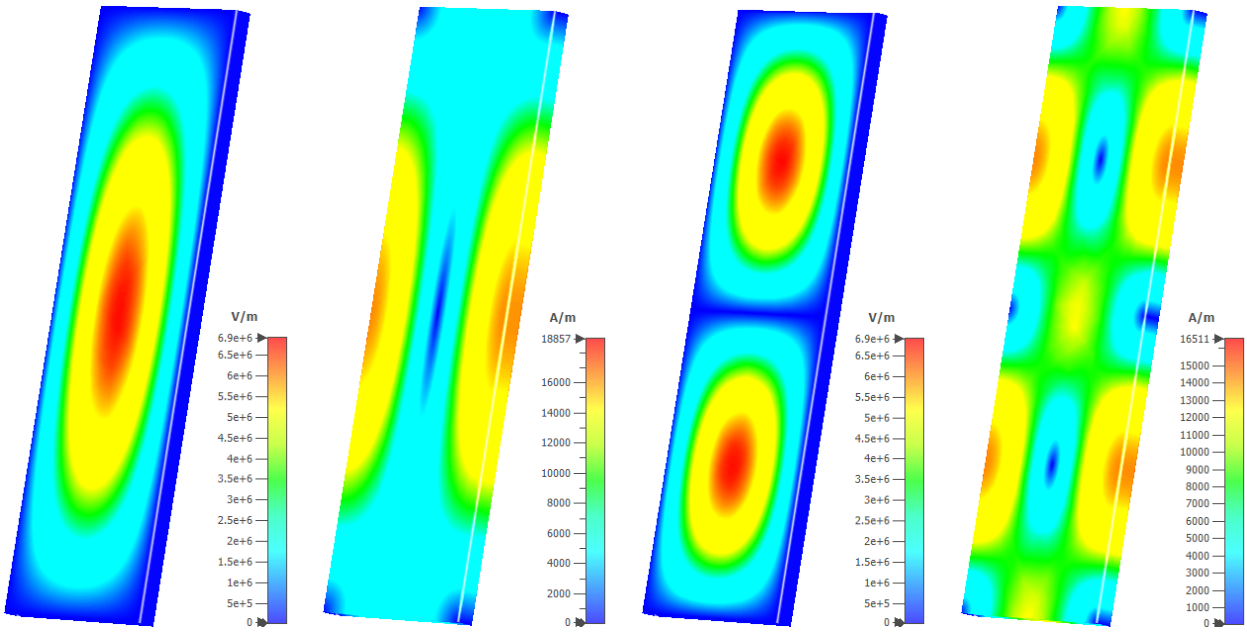

Fig. 3.1: EM field distribution for the first two eigenfrequencies for an R3 beampipe without cavities.

The resonant frequency of the fundamental mode from simulations are shown in Fig. 3.1 to be $f_0 = 395$ MHz. The difference between cutoff frequencies given by the analytical solution and simulation can be explained by the 6 mm blending radius of the edges which is taken into account in simulation but neglected during analytical calculations.

Simulations of the first two eigenmodes were carried out. The resonant frequency of the monopole mode of the elliptical cavity is around 234.5 MHz, the cylindrical cavity's first resonant frequency is found at 234.7 MHz. Diameter of the cylindrical cavity was chosen in a way to have the same or very similar monopole mode frequency to the monopole mode frequency of the elliptical cavity. Simulation results are given below:

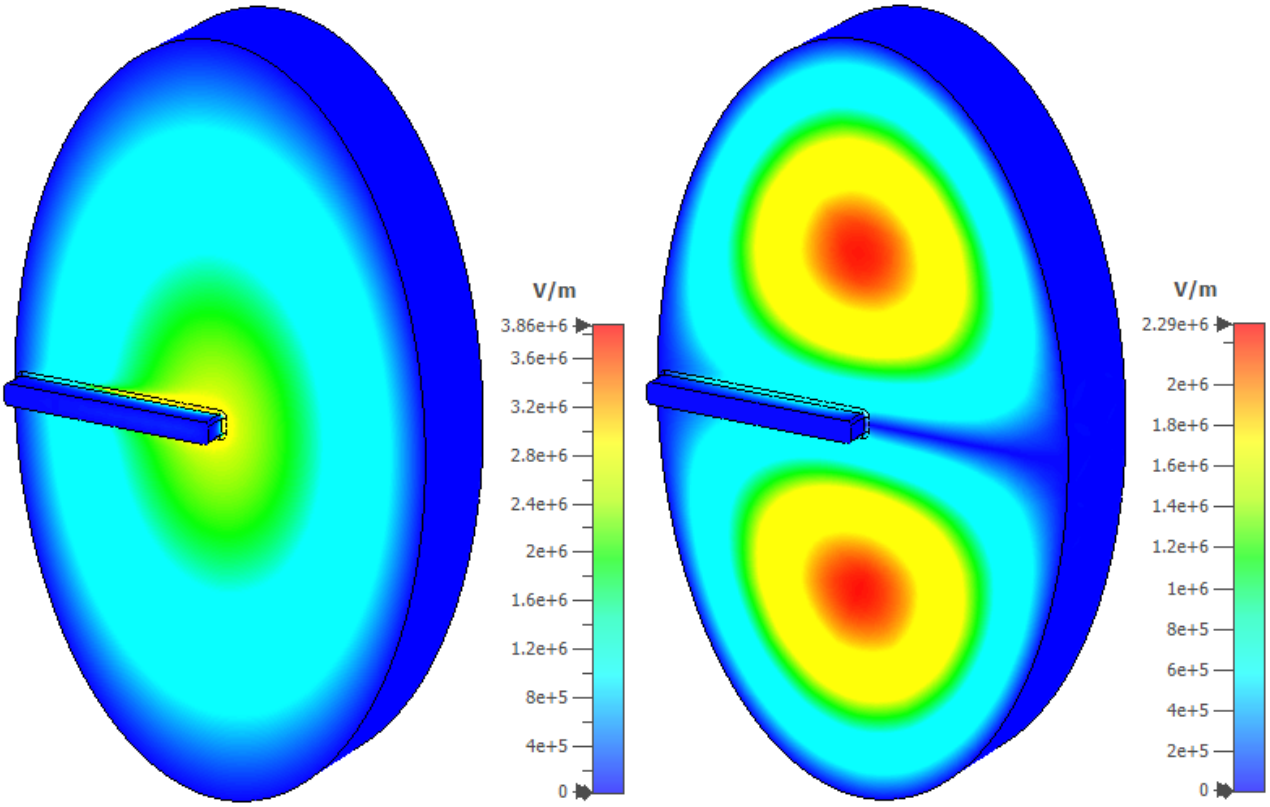

(a) Monopole mode. (b) Dipole mode.

Fig. 3.2: Field modes simulations for the elliptical cavity

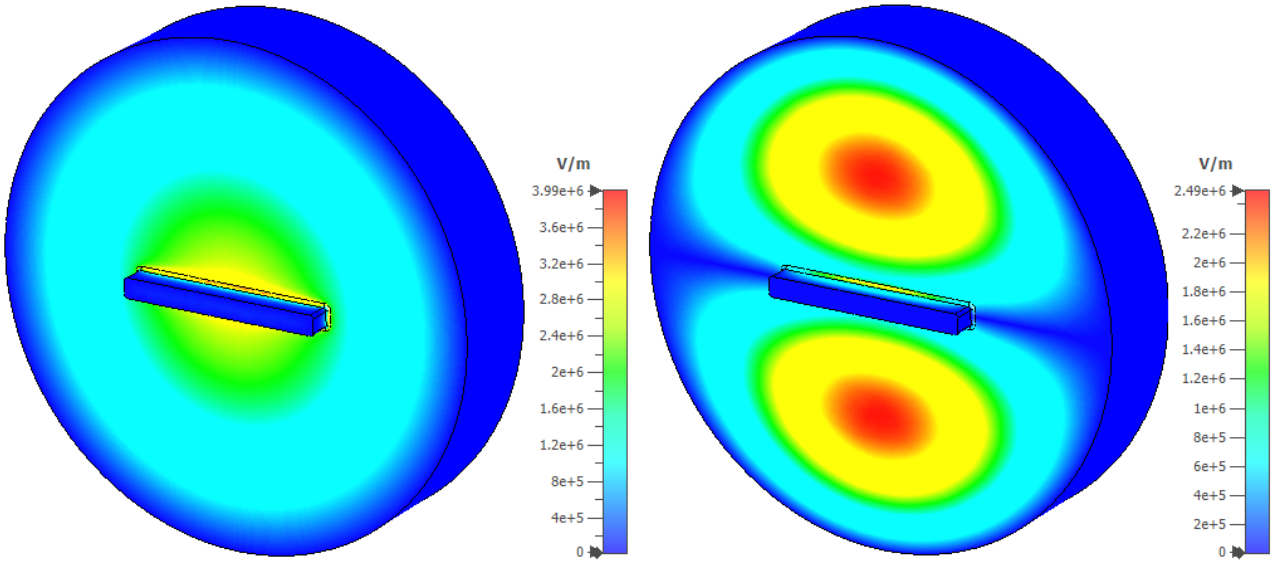

(a) Monopole mode. (b) Dipole mode.

Fig. 3.3: Field modes simulations for the cylindrical cavity

From the Fig. 3.2 and Fig. 3.3 one can see that monopole mode has a lesser maximum intensity. This can be used to increase the signal/noise ratio of the Schottky signal.

In the case of the Schottky detector, the entire beam pipe is a source of excitation signal because a charged particle which travels through excites EM oscillations along its path. Another simulation approach is given in the Wakefield solver of the CST package. The Wakefield solver simulates the beam-cavity interaction by calculating the EM field distributions and the wake

fields inside both cavities as the particle passes through. This calculation is done only for one beam pass through the beam pipe, which is useful for linear accelerator RF cavities simulation but not sufficient for simulation of the Schottky cavity installed in a storage ring. In the case of measurements using a Schottky detector, one has to deal with hundreds and thousands of particles passing through the cavity. If one is interested in field propagation inside the entire system including the beam pipe and both cavities during single particle pass, one can use the Wakefield solver. For our case, the Eigenmode solver of the CST package is instead necessary due to the multiple passes of the particle through the system.

The Eigenmode solver can simulate field distribution only for one cavity at the same time. It assumes that the enitre model has only one excitation point which is sufficient for simulation of common radiofrequency devices. When modeling a system of two cavities joined with a common beam pipe, they must be placed sufficiently far from each other so that the EM field can not directly propagate from one cavity to another, therefore EM field oscillations are only calculated in one cavity at a time. This means that for every simulation one cavity is excluded from the simulation as a source of signal.

To overcome the issue with the Eigenmode solver described above, field distribution of the cavities along the center of the beam pipe was investigated. Both cavities were simulated separately, but the model considers the same beam pipe with a cylindrical and elliptical cavity in place. All sizes were constant during all simulations. The profile of the Z component of the EM field along its respective axis in the middle of the beam pipe was taken and the zero point for each plot is the center of the corresponding cavity. This simulations issue is illustrated in Fig. 3.4. Field distributions for both cavities are shown in Fig. 3.4c. Distribution of the normalized field intensities with a maximum in the same Z-point are shown in Fig. 3.5.

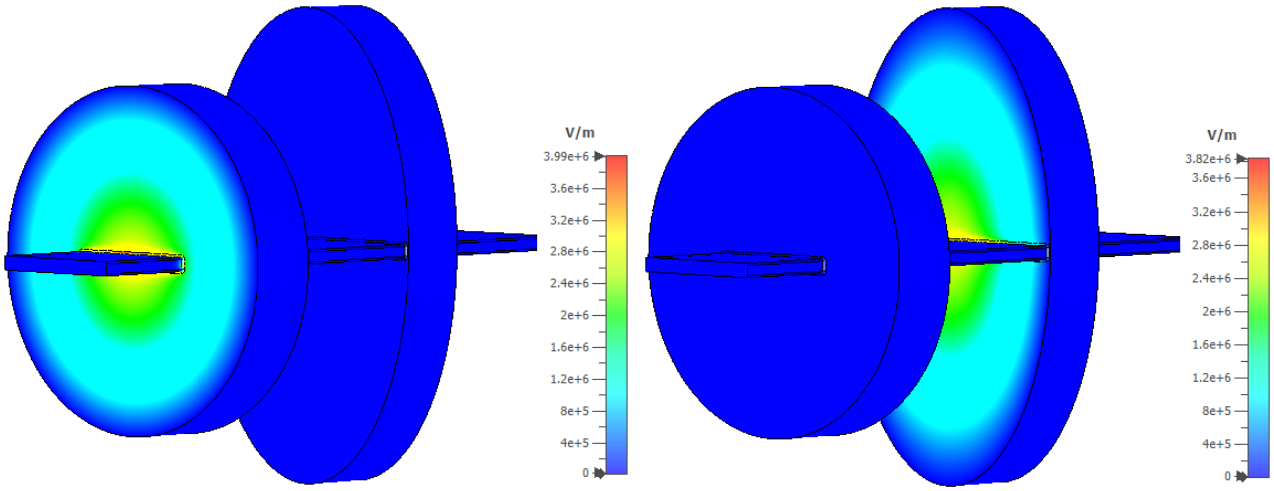

(a) Simulations of the EM field distribution in the cylindrical cavity.

(b) Simulations of the EM field distribution in the elliptical cavity.

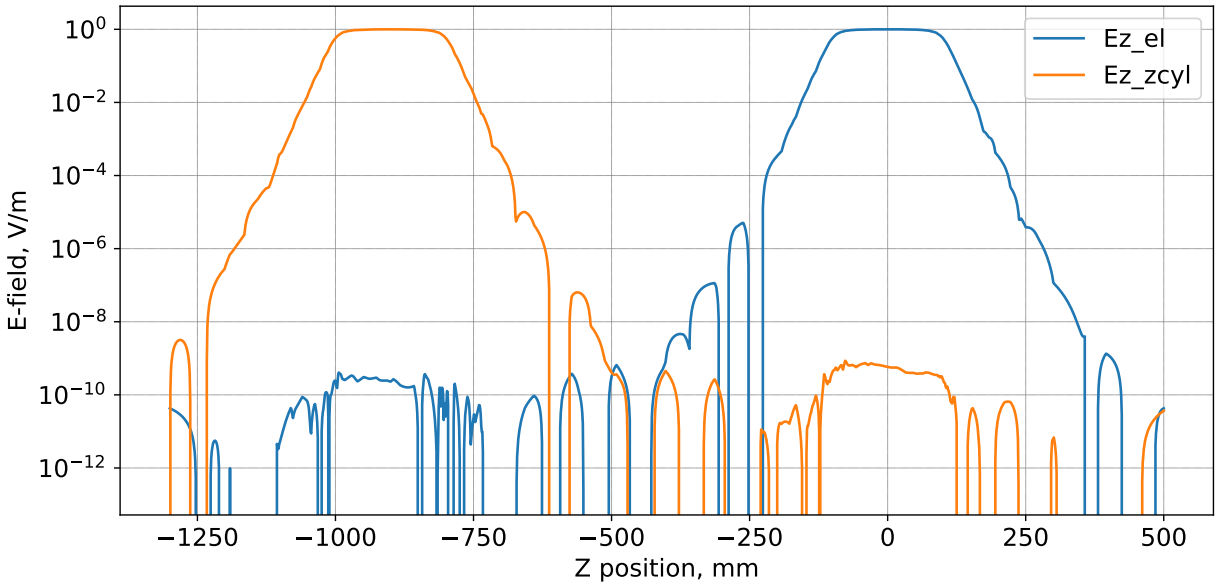

(c) Superposition of the EM field distributions.

Fig. 3.4: Field modes simulation for a structure containing two cavities.

As one can see from Fig. 3.4c, intensity of the longitudinal component of the electric field significantly drops with distance. Based on this plot we decided to check at which distance we can neglect the cross-talking effect. For better understanding it was decided to plot both intensity distributions on the same plot but overlap one with another by bringing their maximum points to the same x-coordinate. Results are shown in Fig. 3.5:

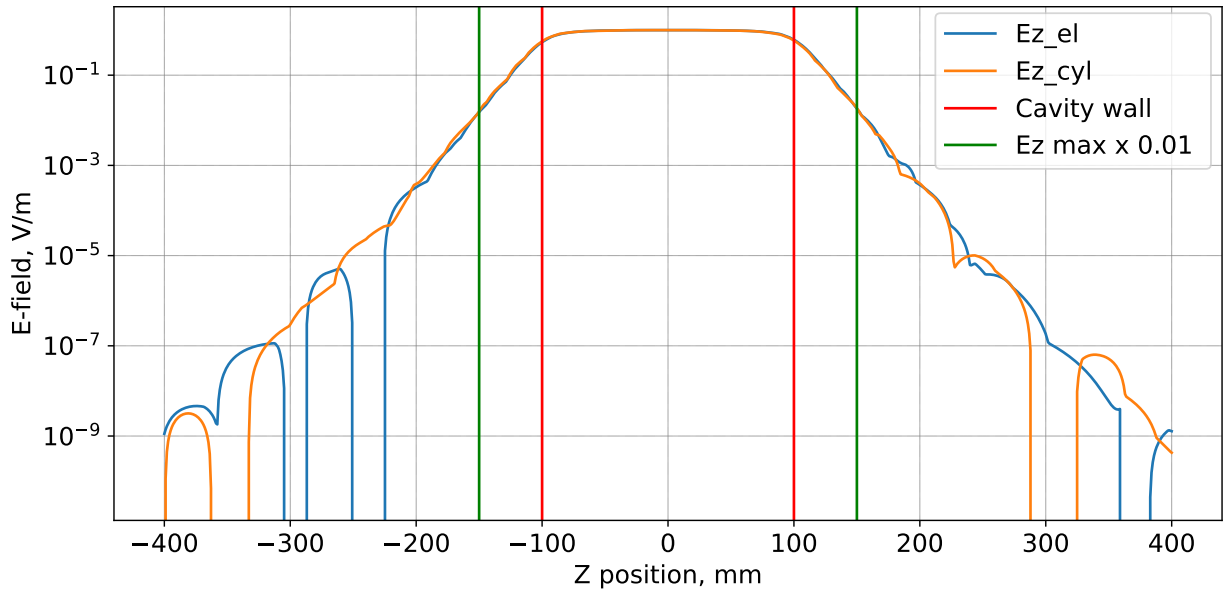

Fig. 3.5: Longitudinal field distribution along the center of the beam pipe. Cavity walls are shown on the plot with red lines.

As shown in Fig. 3.5 we decided that if the field intensity of the cylindrical cavity reduces 2 orders of magnitude along the longitudinal symmetry axis of the beam pipe, one can neglect its influence on the resolution of the position sensitive cavity (green lines in the plot). Field distribution error caused by the interaction between EM fields of the cylindrical and elliptical cavities on the distance between cavities centers more than 300 mm is negligible.

3.3 Longitudinal Extension of the Cavity

When the particle travels through the cavity it induces a mirror charge on the cavity walls. Distribution of this charge depends strongly on the particle's charge and velocity. Perturbation of the electromagnetic field caused by the particle excites oscillations of the electromagnetic field inside the cavity at the resonant frequency defined by the cavity size. These oscillations are a superposition of all possible oscillation modes. In this work we will focus on the fundametal Transverse Magnetic mode TM_{010} because it has the largest part of the energy stored in the electromagnetic field. The TM mode means that the component of the magnetic field along the particle trajectory $\vec{H}_z$ equals to zero and the other two components are perpendicular to it. Another fundamental mode is TE_{111}, but it has much higher frequency than TM_{010}.

In the case of a cylindrical cavity with inner radius of 490 mm, the TM_{010} mode will have frequency $f_0 \approx 235$ MHz, whereas the TE_{111} mode will have $f_0 = 1.5$ GHz. The TM_{010} mode will be the first fundamental mode if the cavity extension L is less than $2.03 \times R$ where R is radius of the cavity [39].

Our cylindrical cavity has R of 490 mm, which limits our extension L to be smaller than 1000 mm. A lower limit of the cavity extension is set by the inner radius of the DN40CF flange at 38 mm. This must be applied to allow us to read the signal from the oscillations inside in order to tune f_0.

The frequency of the field oscillation defines period of time when the field changes its phase. Let's imagine that we have a cavity with length of 1000 mm and TM_{010} mode with frequency $f_0 = 300$ MHz. If an ultra-relativistic particle travels through this cavity with the speed of light in vacuum c_0 it will move 500 mm with a co-directional $\vec{E}_z$. But for the next 500 mm $\vec{E}_z$

will be directed opposite to the direction of propagation. This will lead to lower R/Q value, decreasing the signal amplitude. Thus, the cavity extension should be such that particle leaves the cavity volume with the smallest possible energy losses caused by the interaction with the field inside the cavity.

Our cylindrical cavity has resonant frequency of around 235 MHz. The distance which will be covered by a particle with the speed of light for one period will be 1270 mm. This means that even for ultrarelativistic particles, the cavity extension L has to be no more than 635 mm otherwise signal will have a reduced power. For slower particles the cavity extension has to be even smaller. In our simulations we calculate the extension of the cavity to have the biggest R/Q value and resolution for the different $\beta = v/c_0$ values where v is velocity of the particle. Simulation results are shown in Fig. 3.6

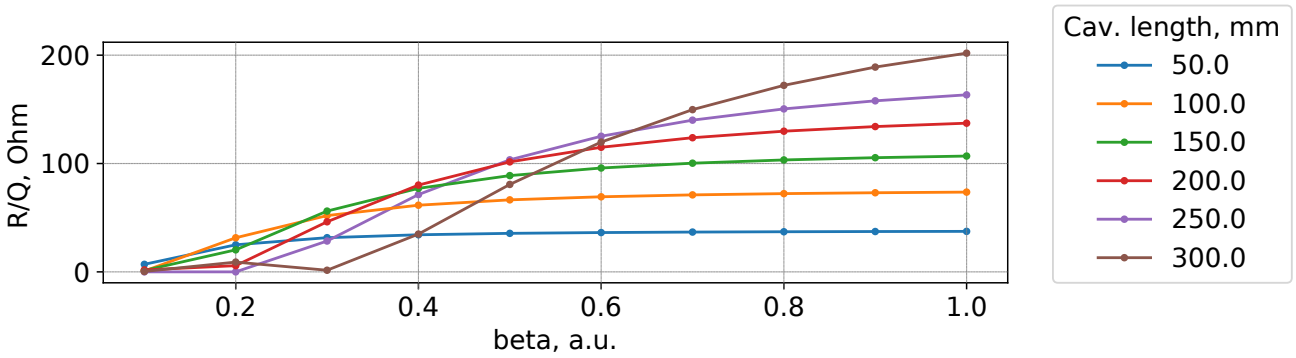

(a) R/Q-beta dependency for cavity extensions between 50 and 300 mm.

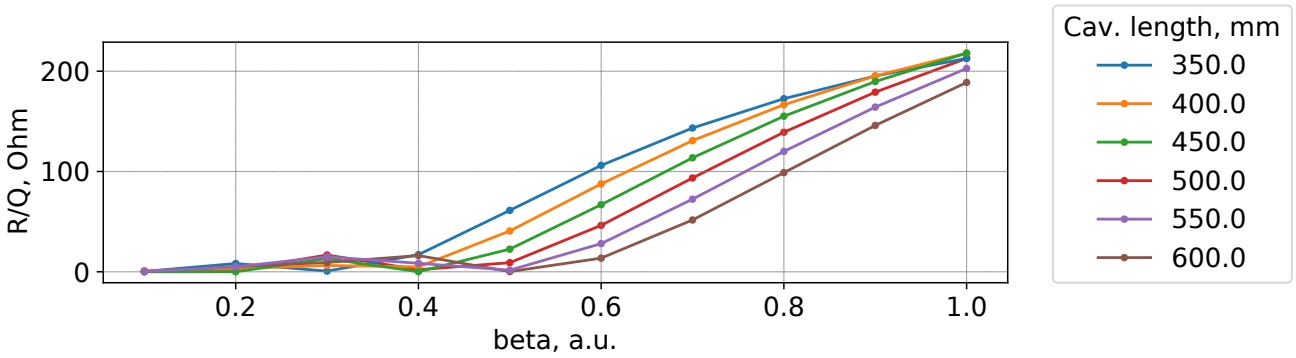

(b) R/Q-beta dependency for cavity extensions between 350 and 650 mm.

Fig. 3.6: R/Q dependency on beta for different extension of the elliptical cavity

From Fig. 3.6 one can see that there is a dependency between the shunt impedance of the cavity and its extension and this dependency is different for the different energies of ions. The velocity of the particles which will pass through the cavity in a storage ring is not fixed. So we will follow the most general approach and choose the cavity which will have the best output for every particle speed. To figure out which extension is the most suitable we will calculate the area under the curve in R/Q-beta dependency plot for every extension by using trapezoidal method. Details can be found in Table 3.1

Table 3.1: Cavity response comparison for different cavity extensions.

Cavity length, mm	Area under curve
50	29.58
100	53.42
150	70.13
200	80.58
250	85.84
300	85.79
350	81.10
400	74.46
450	67.02
500	59.44
550	51.61
600	43.54

As one can see from Table 3.1, simulations of R/Q for different β values show that the best cavity extension which will be suitable for most of the particles velocities is 250 mm. However, taking into account that the highest energy achieved at R3 was 345 MeV/u [56, 57] and corresponding $\beta = 0.68$ we decided to go for a extension of 200 mm. This is the same extension as the existing cylindrical Schottky cavity at RIKEN [58]. Next simulations were done for the 200 mm cavities with resonant frequencies of around 235 MHz. Sketches of the cavities are presented in Fig. 3.7:

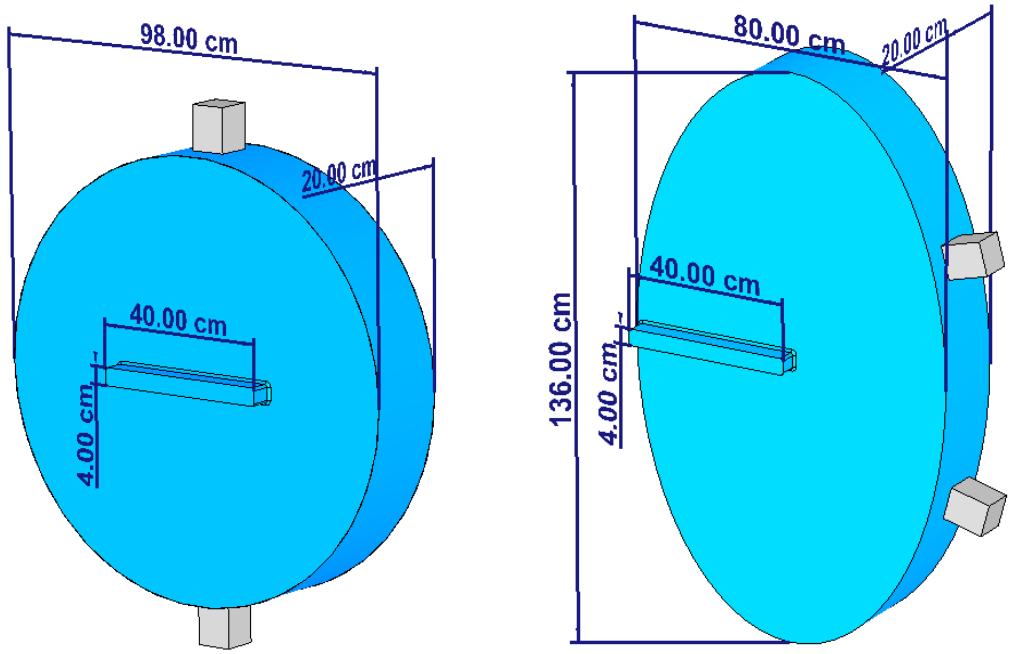

(a) Cylindrical cavity. (b) Elliptical cavity.

Fig. 3.7: Sketches of the R3 suitable cavities modeled in CST Microwave Studio.

3.4 R/Q Distributions for Different Cavity Geometries

There were two main influence behind R/Q studies. Firstly, vertical lines of equal R/Q have to be as straight as possible in the area of interest (the beam pipe area in the elliptical cavity

along the particle path for the full extension of the cavity). Secondly, the gradient of the R/Q distribution along the horizontal plane perpendicular to the particle trajectory has to be linear. Based on these two linearities we will talk about resolution and resolution error. These two variables allow us to compare which cavity is the best for position measurement purposes. An R/Q map and resolution plot are shown in Fig. 3.8. All simulations were done for $\beta = 1$.

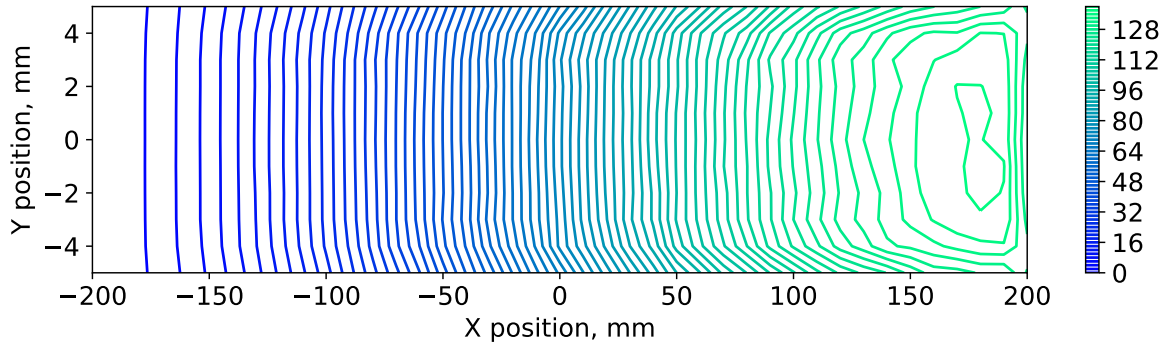

(a) Lines of the equal R/Q inside the beam pipe. R/Q values are in Ohms.

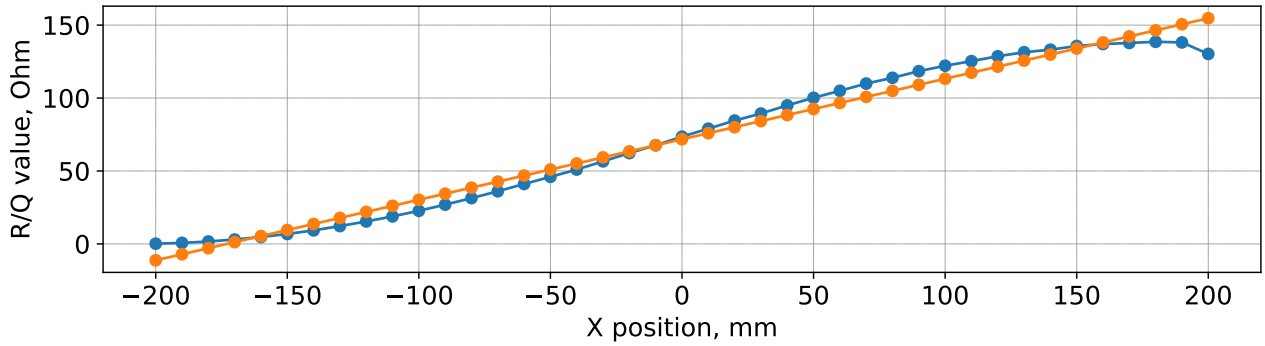

(b) Linearity of the R/Q gradient in horizontal direction at the middle of the beam pipe. Blue dots are simulation results, orange dots are taken from linear fit at the same X-point of the plot.

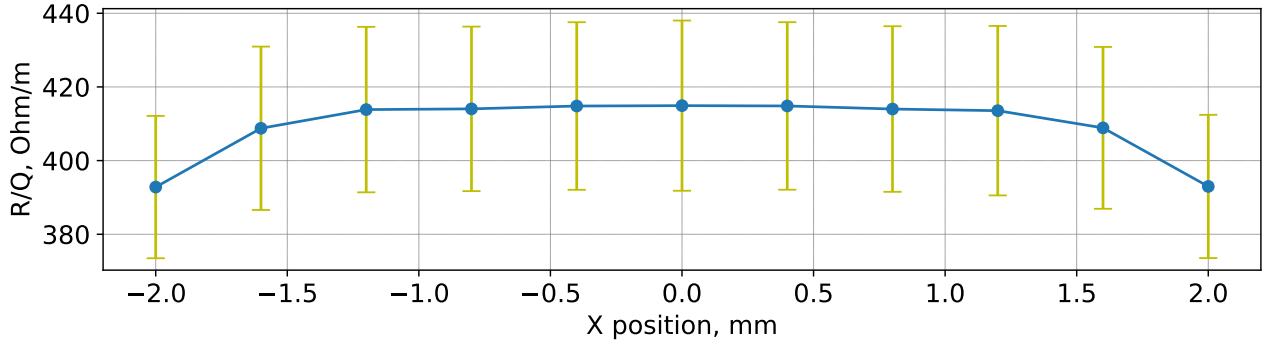

(c) Resolution map for the beam pipe area.

Fig. 3.8: Simulation of the EM field intensity in the R3 elliptical cavity. All dimensions are in mm.

In Fig. 3.8 under the resolution of the cavity we understand the slope of the linear fit over the data points gathered for a horizontal line transverse to the particle path at a given height. The resolution error is a Root Mean Square (RMS) calculation between the fit made by Least Squares Method (LSM) and actual data points in Y-axis. The numbers are given in Table 3.2.

Table 3.2: Cavity response comparison for different cavity extensions. All R/Q values are in Ohms.

Pos, mm	R/Q	Fit R/Q	Pos, mm	R/Q	Fit R/Q	Pos, mm	R/Q	Fit R/Q
-200.0	0.16	-11.22	-60.0	41.09	46.85	80.0	113.9	104.93
-190.0	0.72	-7.07	-50.0	45.98	51.0	90.0	118.43	109.08
-180.0	1.67	-2.92	-40.0	50.99	55.15	100.0	122.13	113.23
-170.0	3.01	1.22	-30.0	56.6	59.3	110.0	125.31	117.37
-160.0	4.74	5.37	-20.0	62.25	63.45	120.0	128.65	121.52
-150.0	6.81	9.52	-10.0	67.65	67.6	130.0	131.4	125.67
-140.0	9.3	13.67	0.0	73.51	71.74	140.0	133.16	129.82
-130.0	12.22	17.82	10.0	79.02	75.89	150.0	135.7	133.97
-120.0	15.41	21.97	20.0	84.55	80.04	160.0	137.02	138.11
-110.0	18.87	26.11	30.0	89.39	84.19	170.0	137.77	142.26
-100.0	22.7	30.26	40.0	94.98	88.34	180.0	138.57	146.41
-90.0	26.92	34.41	50.0	100.17	92.48	190.0	138.15	150.56
-80.0	31.39	38.56	60.0	104.97	96.63	200.0	130.26	154.71

Based on Fig. 3.8 and the data from Table 3.2 we can make some expectations about the signal power from the elliptical cavity according to the particle position, charge and other parameters which are used in equation (2.20).

3.5 Blending of the Pipe Walls Edges

One important factor which has a large effect on the resolution of the position-sensitive cavity doublet is the blending of its beam pipe corners. We have to be aware of any sharp edges and corners which will create field distortions because of the high frequency nature of our signals. To avoid irreducable distortions caused by sharp corners we use blending of the beam pipe corners. Several simulations have been conducted in order to figure out which blending radius will generate less distortions of the electromagnetic field inside the cavities. For these simulations the pipe-cavity connection blending radius was chosen to be 2 mm. The difference in R/Q map distributions for the cavities with and without blendings are given in Fig. 3.10

As one can see from Fig. 3.10 blending of the pipe decreases the amount of distortions caused by the sharp corners. The best blending radius has been chosen by comparing the resolution to the resolution error ratio for the line of the horizontal symmetry of the cavity which is perpendicular to the particle path. We also desire the resolution to be the same for every vertical position inside the beam pipe with the smallest possible error. From these constraints, we chose a blending radius of 6 mm. Illustration of the resolution comparison is given in Fig. 3.9

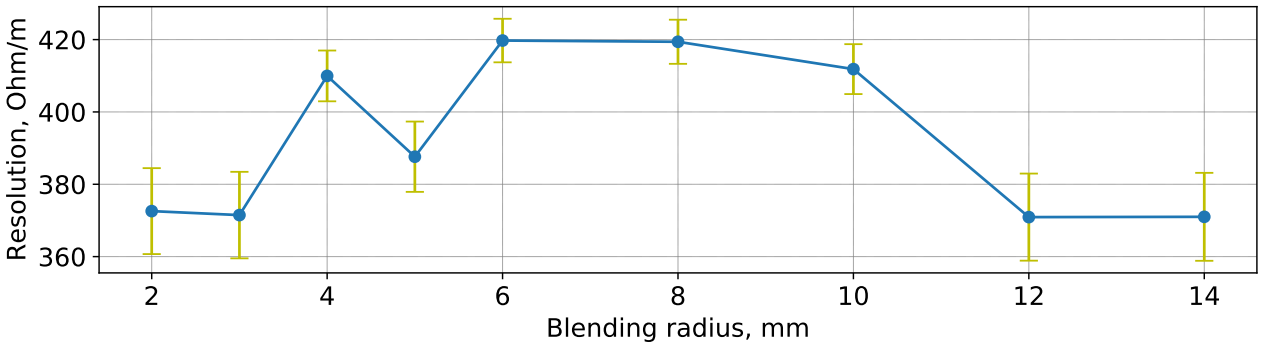

(a) Resolution dependency on blending radius.

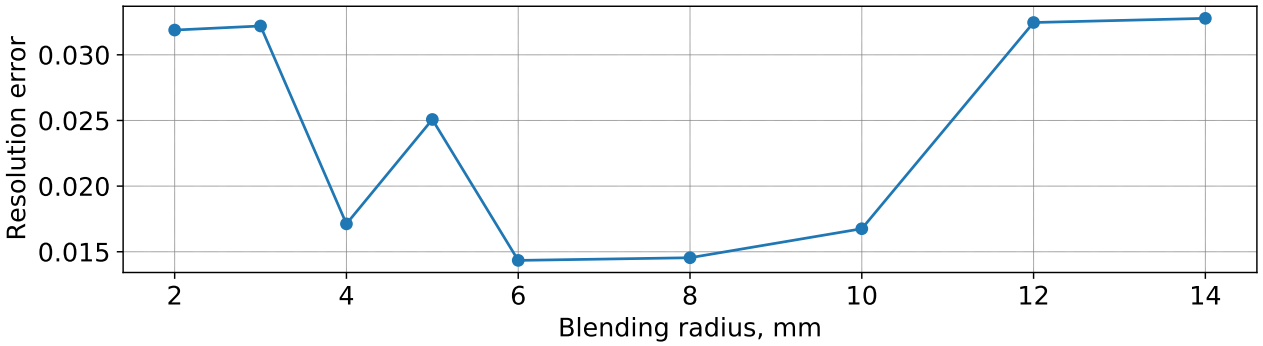

(b) Resolution error dependency on blending radius.

Fig. 3.9: Resolution dependency on blending radius for the elliptical cavity.

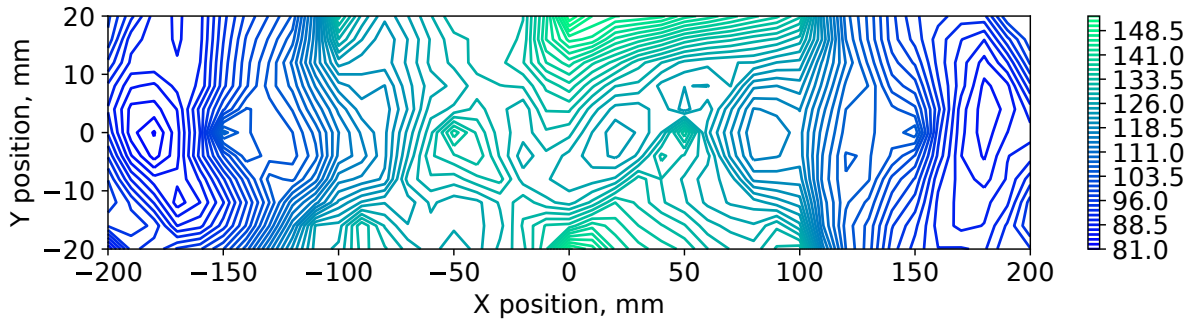

(a) Cylindrical cavity. No blending.

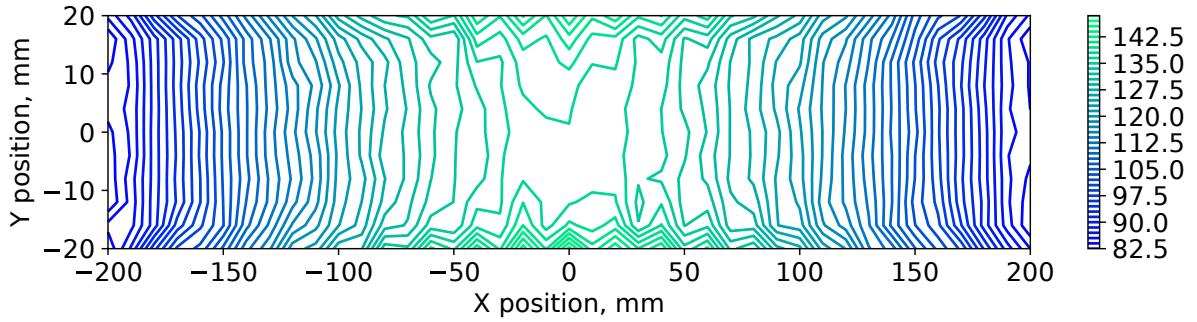

(b) Cylindrical cavity. Blending radius 6 mm.

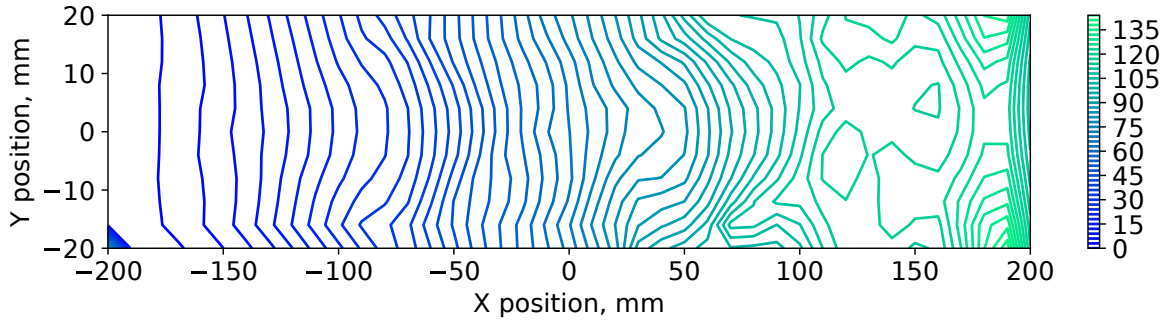

(c) Elliptical cavity. No blending.

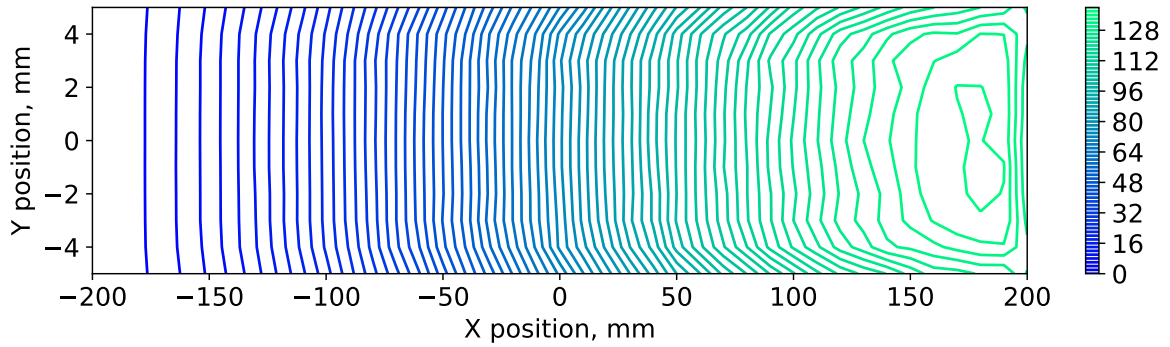

(d) Elliptical cavity. Blending radius 6 mm.

Fig. 3.10: Dependency of R/Q maps distributions in Ohms on blending radius.

According to Fig. 3.9 we decided to choose the blending radius of 6 mm. The same depen-

dency is also valid for the cylindrical cavity. So one can choose the same pipe blending radius for both cavities.

Table 3.3: Resolution and error to resolution ratio dependencies for different blending radiuses.

Blending, mm	Resolution, Ohm/m.	Error, Ohm/m	Ratio	Res.error
2	372.58	11.88	31.36	0.032
3	371.48	11.96	31.06	0.032
4	409.96	7.02	58.4	0.017
5	387.62	9.72	39.88	0.025
6	419.74	6.02	69.72	0.014
8	419.4	6.1	68.75	0.015
10	411.84	6.9	59.69	0.017
12	370.92	12.04	30.81	0.032
14	371.0	12.16	30.51	0.033

Table 3.4 shows that the resolution error is the smallest for the blending radius of 8 mm. However, taking into account error/resolution ratio, we chose 6 mm blending radius.

3.6 Blending of the Pipe-Cavity Connection

Another factor which can affect the resolution of the cavities is blending of the connection between the cavity and the beam pipe. To check this dependency simulations similar to those in Section 3.5 were conducted. All simulations were done for pipe wall edge blending of 6 mm. Difference in R/Q maps distributions for the cavities with and without blendings are given in Fig. 3.12

In Fig. 3.12 areas of interest look much less distorted in the case of the blending of the cavity-pipe connections. This means that even this blending is important because no sharp edges can be near the beam pipe to avoid large resolution errors. However, the walls of the cavity can be welded together without much blending because they are further away from the beam pipe. The resolution error to the resolution ratio dependency on the blending radius of the beam pipe connection to the cavity is shown in Fig. 3.11

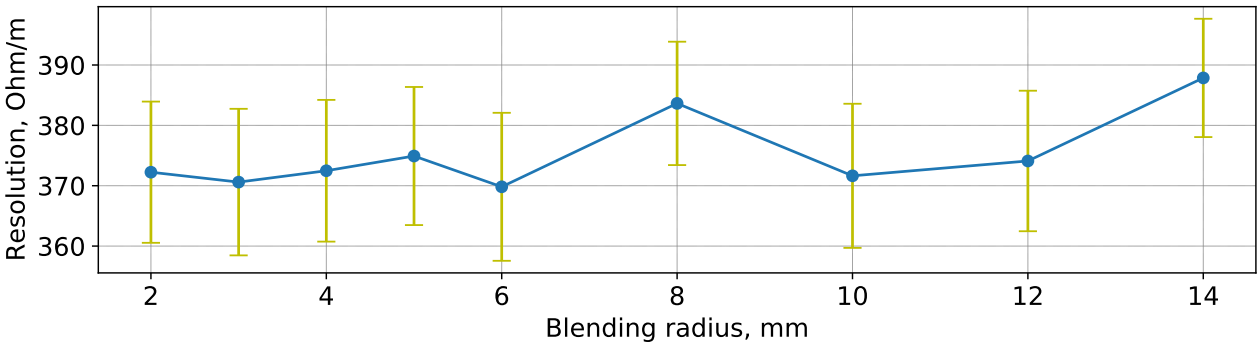

(a) Resolution dependency on the blending radius.

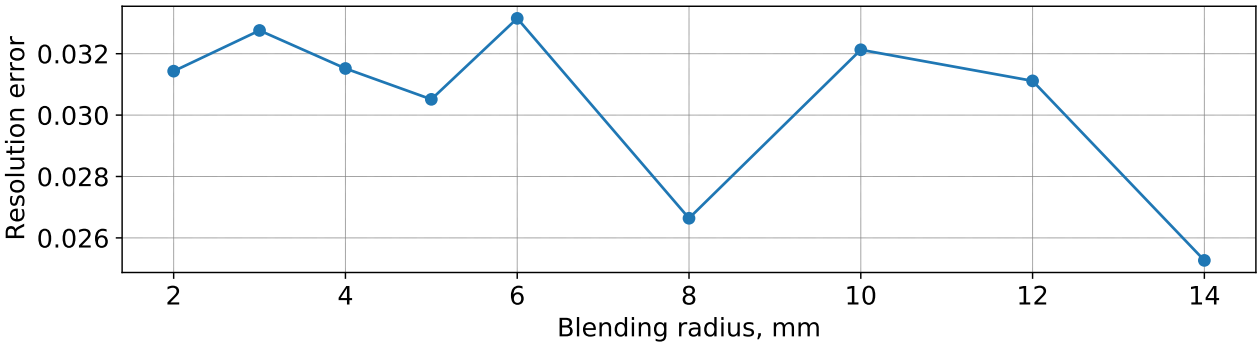

(b) Resolution error dependency on the blending radius.

Fig. 3.11: Resolution dependency on the blending radius for elliptical cavity.

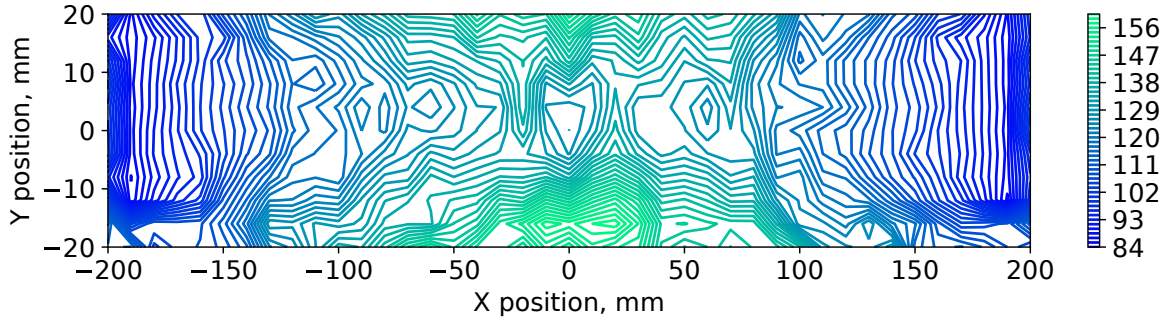

(a) Cylindrical cavity. No blending.

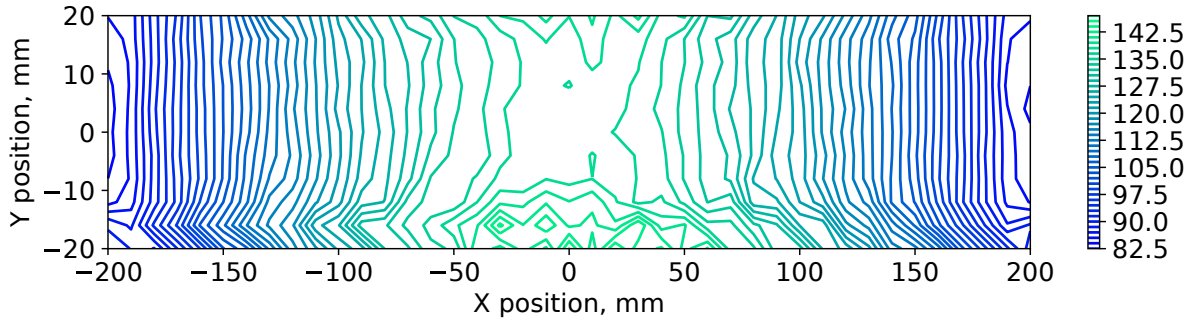

(b) Cylindrical cavity. Blending radius 6 mm.

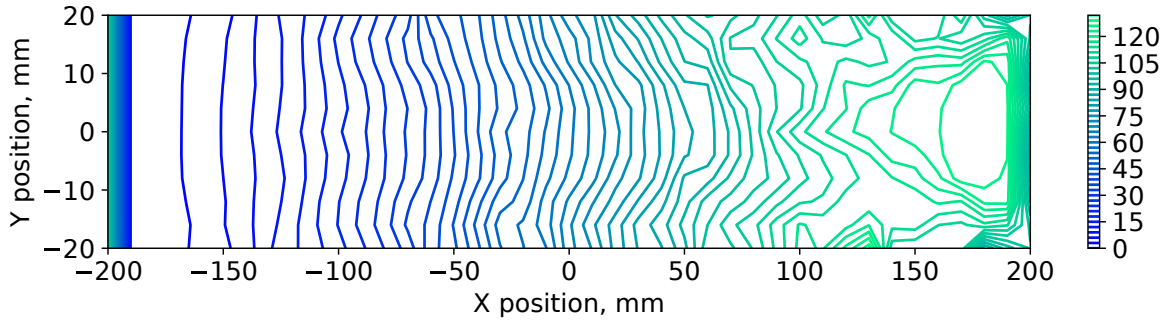

(c) Elliptical cavity. No blending.

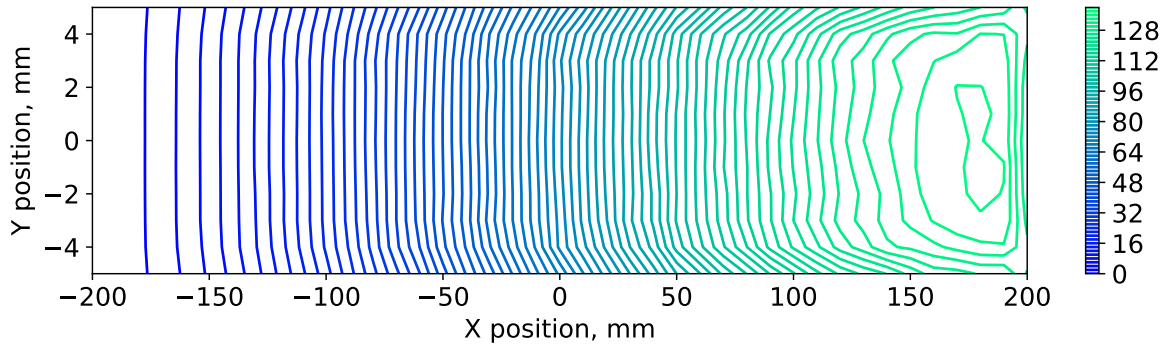

(d) Elliptical cavity. Blending radius 6 mm.

Fig. 3.12: Dependency of R/Q maps distributions in Ohms on blending radius.

Table 3.4: Resolution and error to resolution ratio dependencies for different blending radiuses.

Blending, mm	Resolution, Ohm/m.	Error, Ohm/m	Ratio	Res. error
2	372.24	11.7	31.82	0.031
3	370.6	12.14	30.53	0.033
4	372.48	11.74	31.73	0.032
5	374.92	11.44	32.77	0.031
6	369.82	12.26	30.16	0.033
8	383.64	10.22	37.54	0.027
10	371.64	11.94	31.13	0.032
12	374.1	11.64	32.14	0.031
14	387.86	9.8	39.58	0.025

The drop in the resolution as well as the resolution ratio for blended connections shown in Table 3.4 happens because of the slope of the linear fit. Indeed, the slope in the case of non-blended connections is larger due to the distortions of the field which leads to a higher R/Q value at the edge of the pipe. However, this configuration is undesirable due to the fact that we demand linear change of the R/Q in the horizontal plane and we can sacrifice higher R/Q values for the sake of linearity. A 14 mm blending radius of pipe-cavity connection together with 6 mm blending radius of the pipe corners leads to a position error of 2.5%. Further increasing of the blending radius does not affect the resolution error by more than 0.2% but increases the complexity of manufacturing and is therefore undesireable.

3.7 Tuners Simulations

To simplify signal processing and to avoid errors caused by the difference in fundamental frequencies, it is necessary to have tuners for the cavity which will change the effective field volume by introducing a plunger made of conducting material. This will change the resonant frequency of the electromagnetic field inside the cavity. This effect has been discovered in [59] and later adapted by [60]. The most convenient plunger shapes are rectangular and cylindrical. As an example, for the elliptical cavity of 340 $\times$ 910 mm the cylindrical tuner with the diameter of 38 mm can manipulate the frequency range by around 1 MHz and freely move inside the DN40CF flange which is widely used for coupler connections. However, for the larger cavities different tuners have to be used mostly because of their manufacturing processes. In addition, the tuner has to be operated by a motor therefore its weight must be manageable. In the case of a large tuner, the structure must be hollow. Thus a large rectangular tuner is easier to produce than a large cylindrical one.

Placement of the tuner has to be as far as possible from the beam pipe to avoid field distortions but must be placed at a point of high efficiency. In the case of an elliptical cavity, the tuner has to be in the middle of the arc between the top point and the horizontal line which goes through the center of the beam pipe. It has to be placed opposite to the beam pipe side of the cavity. The two tuners have to move simultaneously to keep the field profile symmetric, so the second tuner has to be placed symmetrically on the bottom half of the cavity. The tuners of the cylindrical cavity can be placed directly on the very top and bottom. In this Chapter we will compare different tuner shapes and sizes. An illustration is given in Fig. 3.13. Lines with negative tuner position are related to plungers of rectangular shape whereas positive tuner position relates to the plungers of cylindrical shape. In both cases plungers were moving 250 mm deep into the cavity volume and the zero point was taken at the cavity wall.

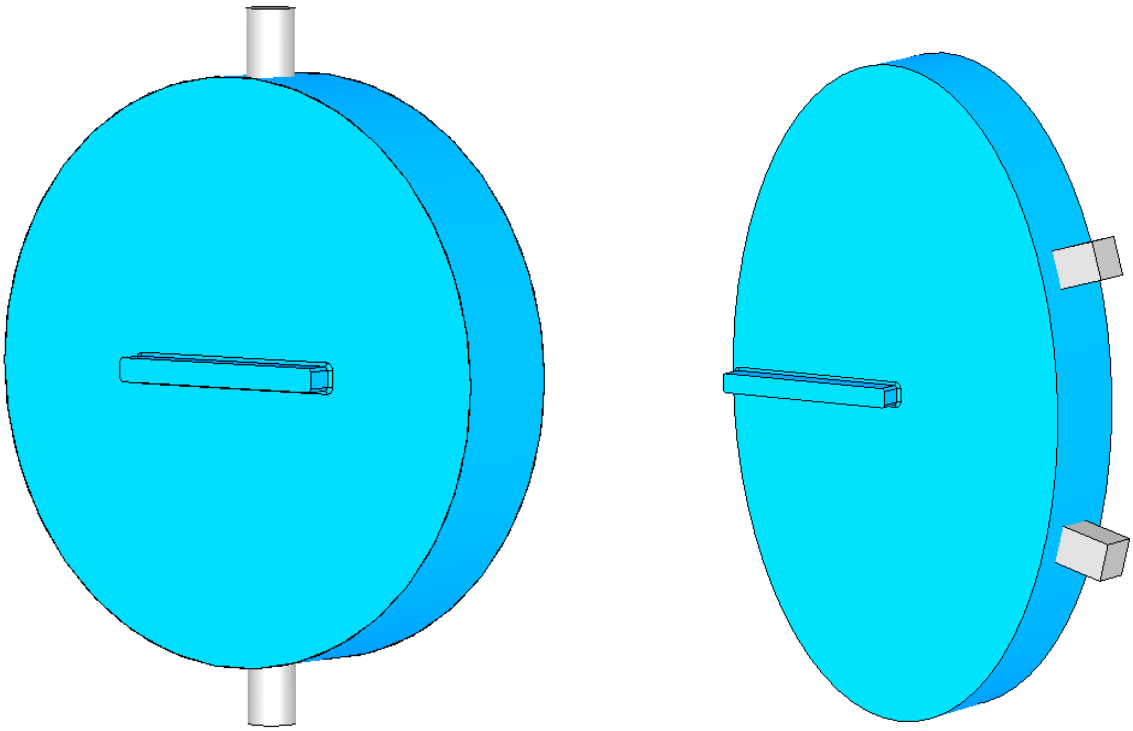

(a) Tuners on top of the cylindrical cavity. (b) Tuners on the side of the elliptical cavity.

Fig. 3.13: Cavities with tuners. Tuner placement for both rectangular and cylindrical geometries were simulated.

At first we want to know which shape and size of the tuner will be the most efficient. To compare different tuners sizes and placements we will use the difference between fundamental mode frequencies for the cases when the tuner is fully retracted and at maximum possible insertion without perturbation of the fundamental mode. On the plot, the point related to the largest plunger depth is the point at the highest frequency. After this point distortions caused by the presence of the plunger rearranges the field modes such that the fundamental mode is damped by higher-order modes which is destructive for beam position measurements. Also introducing a large volume of metal in the cavity changes the capacitance of the cavity-coupler system which leads to a significant change of the resonant frequency. Results for the different radii of cylindrical and rectangular tuners placed at the top of the cavities are shown in Fig. 3.14. Details are given in Table 3.5 and Table 3.6. The fundamental resonant frequency for an empty cavity was found to be 234.56 MHz for the elliptical and 234.70 MHz for the cylindrical one.

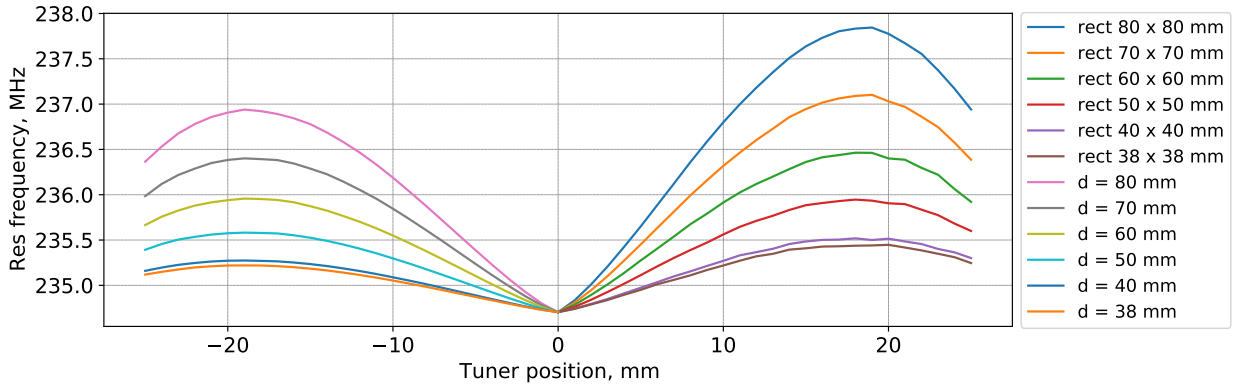

(a) Tuners on top of the cylindrical cavity.

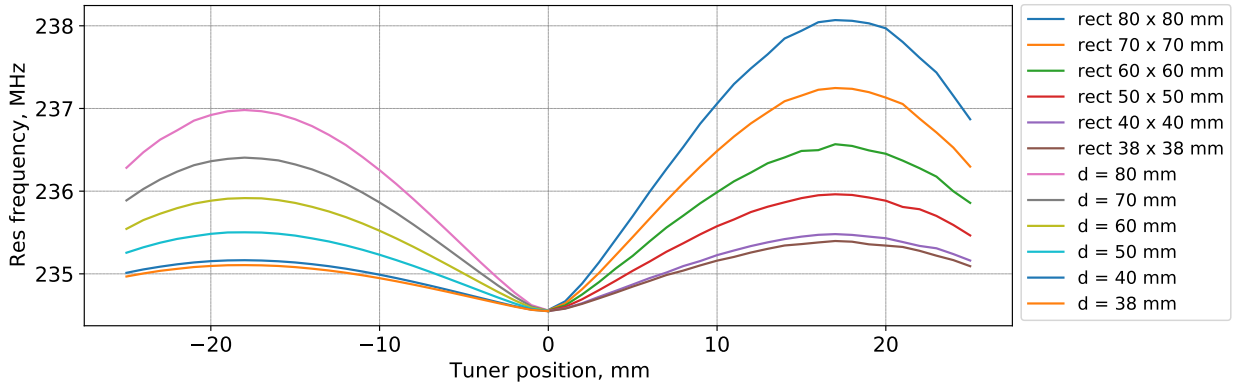

(b) Tuners on top of the elliptical cavity.

Fig. 3.14: Dependency of fundamental mode frequency on tuner size and depth for both cavities.

Table 3.5: Comparison of the tuner's efficiency depending on the shape of a tuner for cylindrical cavity.

Tuner shape	Tuner size, mm	f_{max}, MHz	Δf, MHz
Rectangular	80 × 80	237.84	3.1
Rectangular	70 × 70	237.1	2.36
Rectangular	60 × 60	236.46	1.73
Rectangular	50 × 50	235.95	1.23
Rectangular	40 × 40	235.52	0.8
Rectangular	38 × 38	235.45	0.73
Round	80	236.94	2.24
Round	70	236.4	1.7
Round	60	235.96	1.25
Round	50	235.58	0.88
Round	40	235.27	0.57
Round	38	235.22	0.52

Table 3.6: Comparison of the tuner's efficiency depending on the shape of a tuner for elliptical cavity.

Tuner shape	Tuner size, mm	f_{max}, MHz	Δf, MHz
Rectangular	80 × 38	238.07	3.51
Rectangular	70 × 40	237.25	2.69
Rectangular	60 × 50	236.57	2.01
Rectangular	50 × 60	235.96	1.41
Rectangular	40 × 70	235.48	0.93
Rectangular	38 × 80	235.4	0.85
Round	80	236.98	2.42
Round	70	236.41	1.85
Round	60	235.92	1.36
Round	50	235.5	0.95
Round	40	235.16	0.62
Round	38	235.11	0.56

As one can see from Fig. 3.14 and the table with simulation results, the most efficient tuner is a rectangular plunger 80 × 80 mm situated on top of the cylindrical cavity.

Another simulation has been completed to compare the influence of one plunger on the resonant frequency. Simulations were done for the rectangular plunger with dimensions 80 × 80 mm and for the cylindrical one with a diameter of 80 mm. The results are shown in Fig. 3.15.

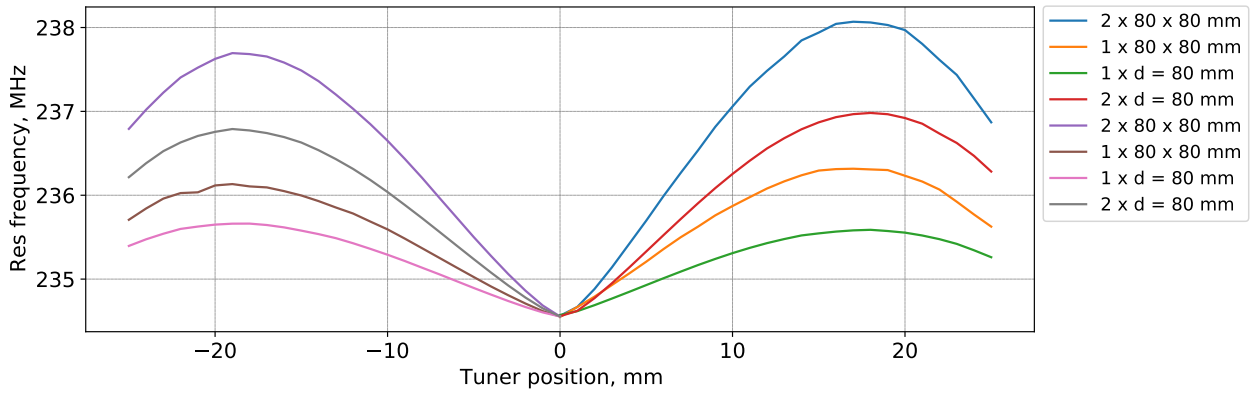

Fig. 3.15: Tuner position - frequency change dependency. Curves with positive (negative) X-coordinate correspond to the elliptical (cylindrical) cavity.

Table 3.7: Comparison of the tuner's efficiency depending on their amount.

Cavity	Amount	Tuner configuration	Tuner size, mm	f_{max}, MHz	Δf, MHz
Cylindrical	2	Rectangular	80 × 80	237.84	3.14
Cylindrical	2	Round	80	236.94	2.24
Cylindrical	1	Rectangular	80 × 80	236.28	1.58
Cylindrical	1	Round	80	235.81	1.11
Elliptical	2	Rectangular	80 × 80	238.07	3.51
Elliptical	2	Round	80	236.98	2.42
Elliptical	1	Rectangular	80 × 80	236.32	1.77
Elliptical	1	Round	80	235.59	1.02

It is clear from Fig. 3.15 and Table 3.7 that one tuner has one half as much effect on the frequency change in comparison to the two plungers which are simultaneously introduced at the same depth. Blending of the beam pipe to cavity connections is very important for maintaining a linear R/Q gradient in the horizontal direction while keeping it almost unchanged in the vertical plane in the area of interest. In this work we also simulated rectangular plungers with different blendings in order to evaluate influence of the tuner blending on the electromagnetic field distribution inside the cavity. A rectangular plunger 80 × 80 mm with blended shaft vertices, bottom face vertices and both shaft vertices and bottom face vertices were simulated. An illustration is given in Fig. 3.16. The results are shown in Fig. 3.17. We will illustrate only the R/Q map of the elliptical cavity for different tuner blendings. Results on the resolution error calculations are given in Table 3.8. For every picture plungers are symmetrically placed on top and bottom of the elliptical cavity as seen in Fig. 3.13 and every plunger is inserted 180 mm into the cavity.

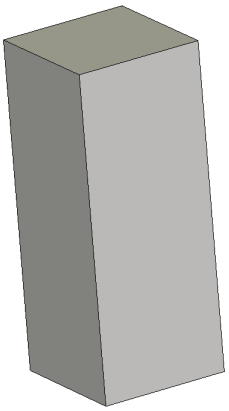

(a) No blending.

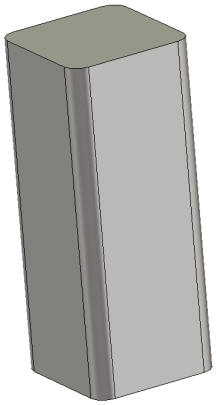

(b) Shaft vertices are blended with radius of 10 mm.

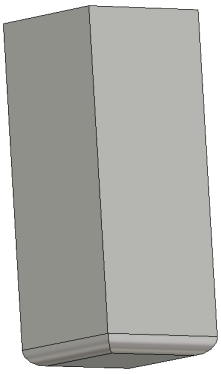

(c) Bottom face vertices is blended with radius of 10 mm.

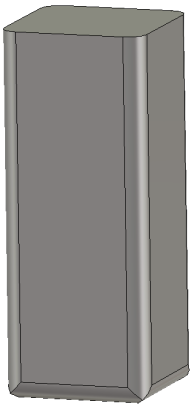

(d) Bottom face vertices and shaft vertices are blended with radius of 10 mm.

Fig. 3.16: Different blending of rectangular plungers.

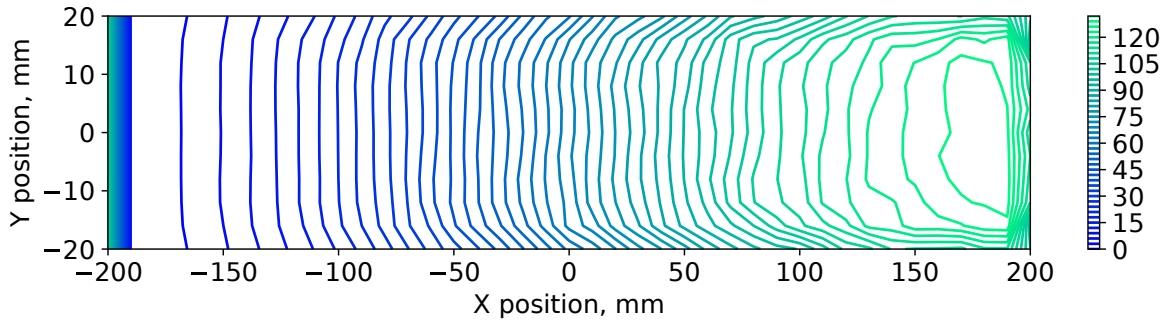

(a) No blending.

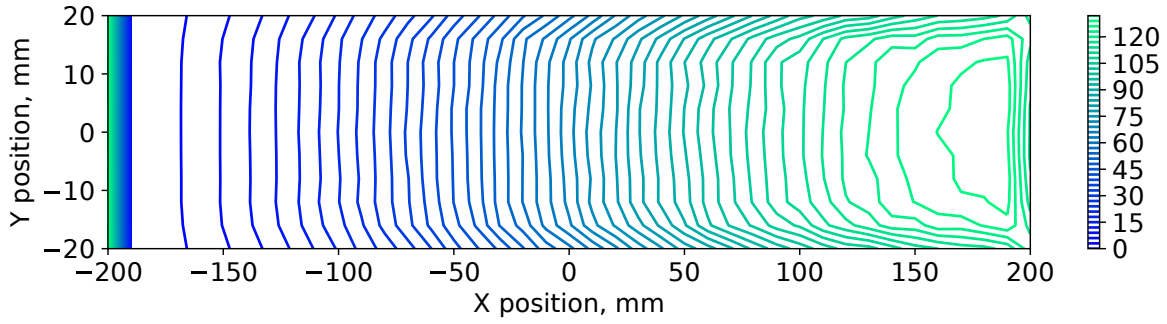

(b) Shaft vertices are blended with radius of 10 mm.

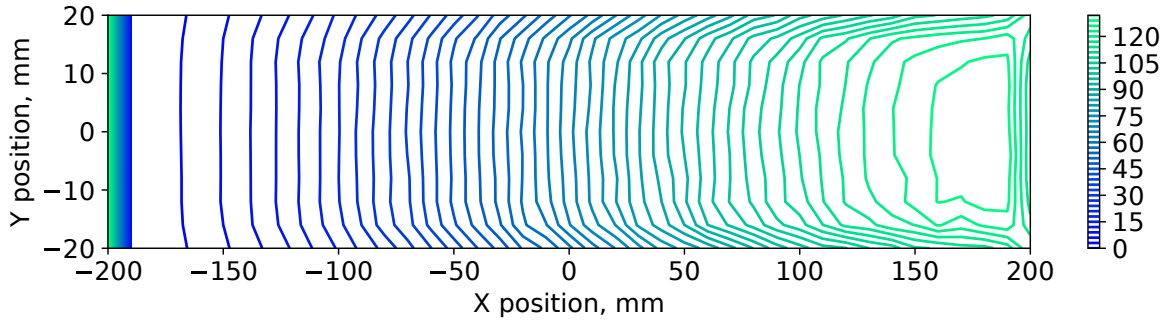

(c) Bottom face vertices is blended with radius of 10 mm.

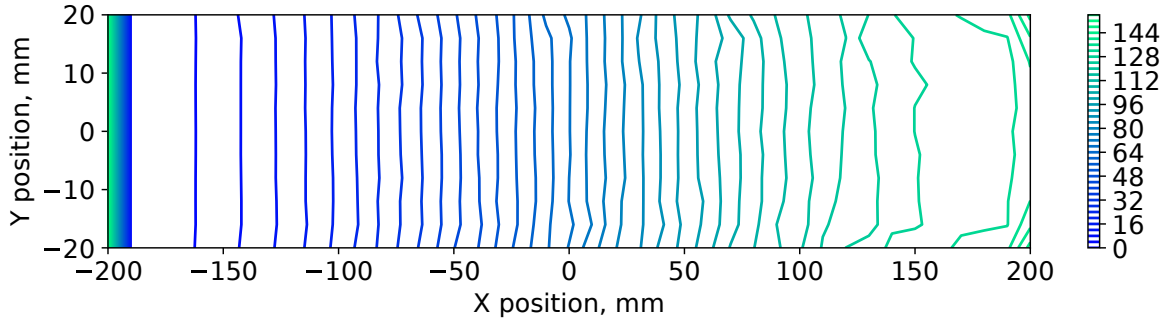

(d) Bottom face vertices and shaft vertices are blended with radius of 10 mm.

Fig. 3.17: Dependency of R/Q maps distributions in Ohms on plunger blending.

Table 3.8: Resolution and error to resolution ratio dependencies for different plunger blending.

Blending type	No blending	Bottom side	Walls	Both
Resolution, Ohm/m.	326.55	318.75	320.31	317.67
Error, Ohm/m	9.32	10.52	10.64	11.04
Resolution/Error	35.04	30.30	30.10	28.77

From Fig. 3.17 and Table 3.8 we can see that blending changes resolution to resolution error ratio. However for the large cavity there is no strict necessity to blend the plunger with a certain radius because of the distance between the beam pipe and the plunger.

An alternative plunger position is the position on the side of the cavity. Large cavities allow this configuration because distance between the beam pipe and plunger is sufficient to neglect distortions caused by the plunger to the field in the area of interest, especially if the plunger is not fully inserted into the cavity. We made a simulations of the R/Q distribution for the tuners which are situated on the side of the cavity which is opposite to the side where beam pipe moved. Here we talk only about the elliptical cavity because we assume that cylindrical cavity is symmetric and there is no reason to change positions of the tuners, it is sufficient to keep them as far as possible from the beam pipe. Illustrations are shown in Fig. 3.18

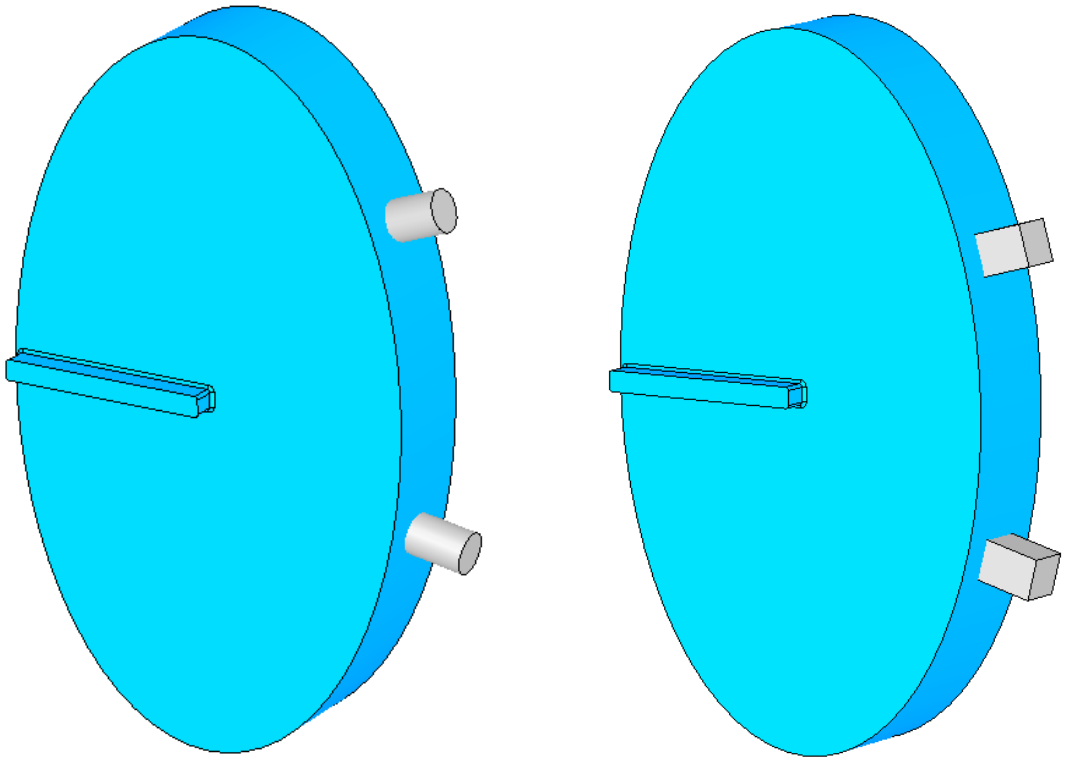

(a) Rectangular plungers.

(b) Cylindrical plungers.

Fig. 3.18: Plungers of different shapes placed on the side of the elliptical cavity

On the R/Q map we can see the influence of the plungers' shape on the field distribution. R/Q maps for both plunger shapes together with frequency dependency are shown in Fig. 3.19.

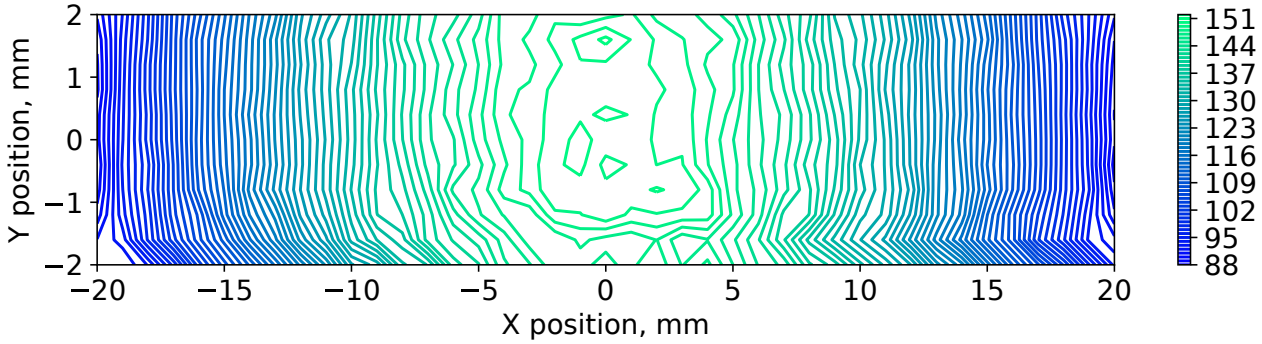

(a) Rectangular plungers.

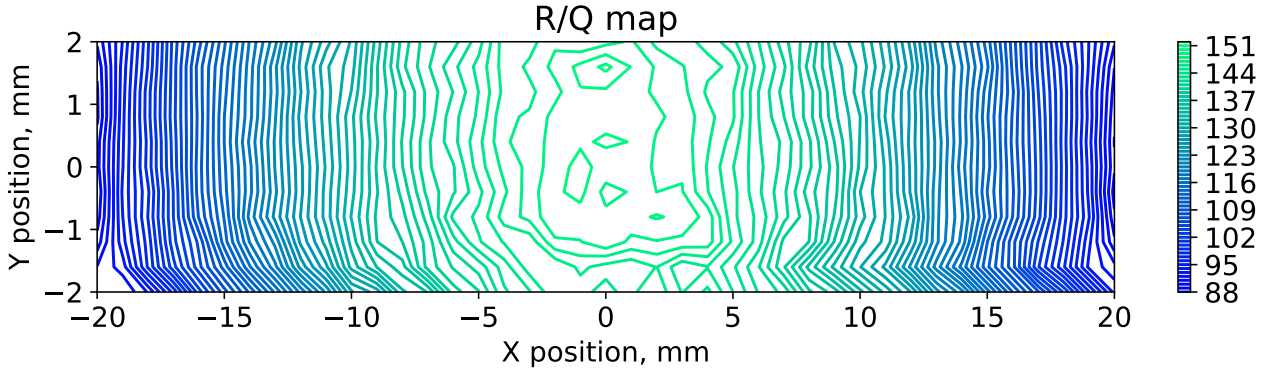

(b) Cylindrical plungers.

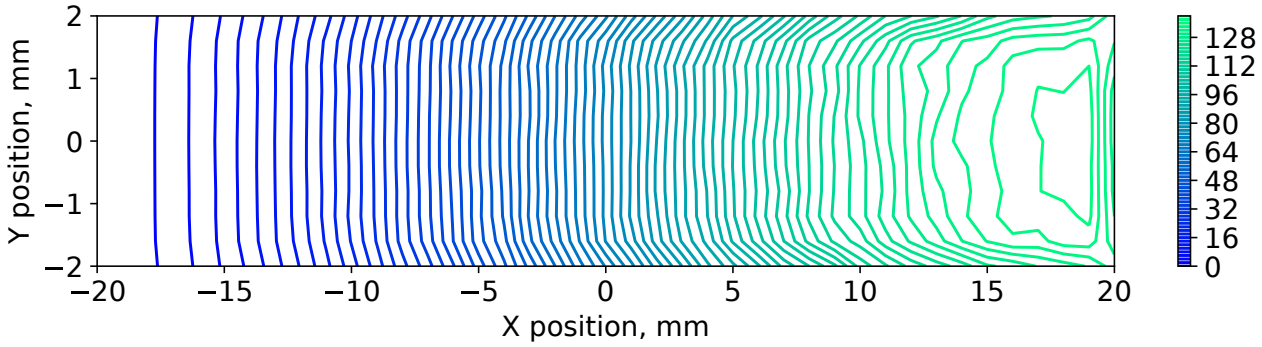

(c) Rectangular plungers.

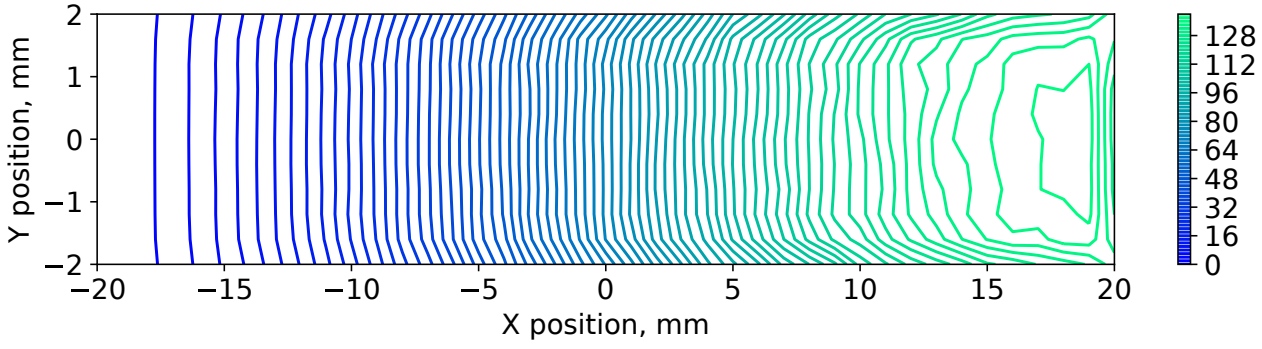

(d) Cylindrical plungers.

Fig. 3.19: Comparison of the plungers of different geometries placed in both cavities. R/Q values are in Ohms.

As one can see from the plots, resolution is not only affected by the shape of the tuner but also by the size of the tuner. The only significant changes are observable in the resonant frequency. The unloaded quality factor also drops around 2-3%. Test measurements of the quality factor and the resonant frequency of the cylindrical cavity will be shown in Chapter 5.

Next we will estimate the signal power for the elliptical cavity based on a typical measurement at R3. The calculations and assumptions will be the same as in example in Chapter 2. We will use a single $^{78}Ge^{32+}$ ion at an energy of 345 MeV/u [57]. In a 60.35m circumference ring, it will have a revolution frequency of 3.4 MHz. R/Q is 120 Ohm at a Q-factor of around 2000. Then, the total power of the signal at the point which is the closest to the side wall of the cavity will be (according to (2.20) -173 dBm, whereas for the point near the center of the cavity it will be about -152 dBm. The difference in power of the signal will be 21 dB. The signal-to-noise ratio after the amplification chain will be 1.60-1.85 times smaller. The concepts of the amplification and the signal-to-noise ratio will be explained in Chapter 4.

3.8 Couplers

A coupler is just a conducting loop that generates a signal due to the oscillation of the electromagnetic field inside the cavity. The flux of the magnetic field through the loop changes with time and this generates a current in the wire of the loop. One side of the loop is connected to the signal wire of the DAQ, whereas the other end is connected to the DN40CF flange with a screw. This ground connection which is also the earth is sufficient for delivering a signal. In the ideal case, one has to have electrical loops as small as possible which means that the antenna and all electronics have to have the same ground potential. One limitation of the magnetic couplers that needs to be considered is a foot-point impedance which is caused by the capacitance of the coupler and the flange.

Different couplers generate different signals and change the resonant frequency of the cavity together with its quality factor (Q-factor). This can be used for reading data from the detector (large Q-factor of the cavity) or to minimise influence of the cavity on the beam quality. For our experiment at the linear accelerator (see Chapter 5), changing of the Q-factor of the cavities was not needed, however it is necessary for the Schottky cavity at ESR [22]. We made couplers similar to the one which is used now for 410 MHz Schottky at ESR. They are shown in Fig. 3.20.

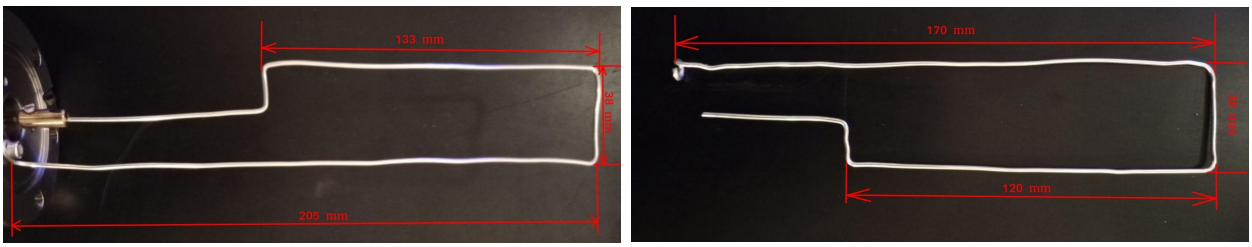

Fig. 3.20: Examples of employed couplers.

These couplers were tested using the adapted position-sensitive prototype for the S-DALINAC tests. Description of the test setup and results will be discussed in Chapter 5.

As a result of the simulations we discovered important factors in the design of the position-sensitive Schottky cavity doublet:

- The cylindrical cavity has to have extension of 200 mm and diameter of 980 mm.
- The elliptical cavity has to have extension of 200 mm, an elongated side diameter of 1360 mm and a narrow side diameter of 800 mm.

- The blending of the beam pipe has to have radius of 6 mm.
- The blending of the beam pipe to cavity connection has to have radius of 14 mm.
- To minimize cross-talking effect from the monopole modes the distance between the cavities has to be larger than 300 mm.
- The blending of the tuners side and bottom vertices have to have radius of 10 mm.
- The most efficient plunger shape and configuration are two symmetrical rectangular plungers with size of 80 × 80 mm.
- A pair of couplers have been produced as test devices and their shapes and sizes are shown in Fig. 3.20.
- According to the simulations the difference in the signal for a single $^{78}Ge^{32+}$ ion at an energy of 345 MeV/u at extreme points will be 21 dB.
- A DAQ based on SDR is suggested to be used as a modern and versatile possible substitution of the existing DAQs.

Based on our design a position-sensitive cavity doublet has been constructed. It is illustrated in Fig. 3.21

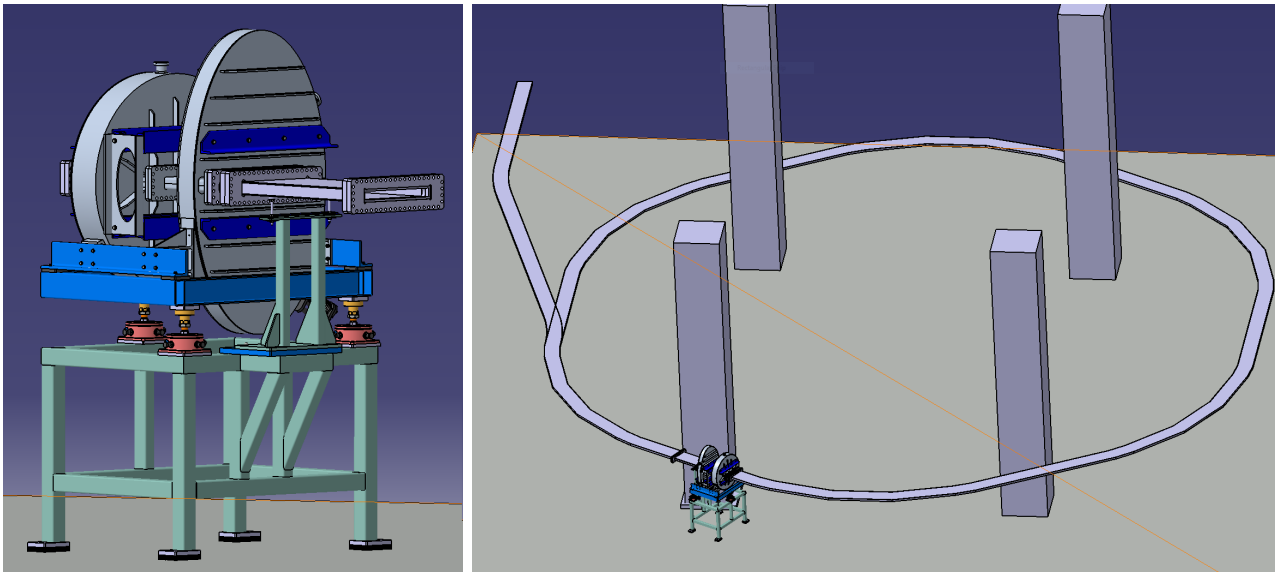

Fig. 3.21: A construction based on our design for R3. Drive units for plungers are not shown in this picture. Construction made by P.Doll @ GSI [61]. On the right side illustrated the installation place inside the R3 ring. The left picture shows the vertical building columns.

As one can see in Fig. 3.21 we also performed finite element analysis of the vacuum pressure to make sure the huge structure can withstand the pressure. Certain actions have been taken to make the structure vacuum tight and stable such as calculations of the horizontal bars geometry and position. The construction has been carried out by P. Doll @ GSI [61] and the FEM calculation was performed by K. Dermati @ GSI [62]. The illustration also shows the restrictions on the cavity sizes due to the close presence of a supporting column.

The total volume of the cavities together with the beam pipe in between is ≈ 0.325 cubic meters or ≈ 325 liters. This volume can be easily pumped out with modern vacuum systems.

We suggest making a DN160CF connection on the beam pipe behind the cavity doublet and connecting it to a turbomolecular pump. The cavity doublet with this pumping setup can reach the vacuum up to the $\approx 10^{-9}$ mbar near the pump connection and $\approx 10^{-8}$ mbar in the far points in the elliptical cavity. In case of the necessity of the uniform pressure distribution, one can remove one of the tuning plungers and install there a second pump however the work of this pump during the measurements will harm the measurement results due to the vibrations.

4 Software Defined Radio Based Data Acqusition System

A Software Defined Radio (SDR) is a digital device for processing, sending, and/or receiving radio waves with fixed hardware but variable parameters that are set entirely using programming. This makes SDR very versatile for many application fields. Apart from its original and main application in communications, they are used in diverse fields of science and programming. The reason for using SDR in our work is the scalability of a DAQ based on SDR. Because SDR is a small, versatile device, which can be easily programmed and replaced, necessary software can be written once and used for as many SDRs as necessary. Together with its simplicity, it allows us to record data with efficiency comparable to DAQs of previous generations (for example, TCAP or NTCAP at ESR [63, 64]). SDR allows recording radio signals with frequencies from 100 kHz to 3800 MHz with a maximum bandwidth of 56 MHz. It has 6 radiofrequency(RF) inputs and 4 RF outputs. More information is given in [65, 66]. A comparison of different SDRs is given in [67]. Comparison of TCAP, NTCAP, and SDR is given in Table 7.1.

SDR is the main device used to read RF signals from cavities in this work. It saves data in I/Q format. I is referred to as "in-phase" whereas Q is referred to as "quadrature". In any event, "in-phase" and "quadrature" refer to the two sinusoids that have the same frequency and are 90 degrees shifted in phase. Later on, this data is saved to a binary file which is formatted as such: "I1 Q1 I2 Q2 ...". Every number uses 16 bits of memory. This data can be processed by any means but we are using the *iqtools* library [68].

To operate the SDR one has to write a program which later will be executed on the SDR chip. This is possible due to the library of low-level drivers for a wide variety of SDR named SoapySDR. We used this library to create a program which initializes a certain SDR, starts the calibration routine and executes a measurement with user-defined parameters such as central frequency, sampling rate, time of measurement, bandwidth, channel and filename for the file where binary data will be written. SDR is able to record data from two channels simultaneously, but only with the same frequency because of only one local oscillator. The program for the SDR can be found in Appendix 7.9

4.1 Test measurements at ESR

We conducted test measurements using a signal generator HAMEG HM8135 and Lime SDR connected directly to it. The signal generator swept frequencies from 499 MHz to 501 MHz. The sweep was done in 200 kHz steps. Sweep time, as well as recording time, was 1 second. The central frequency was 500 MHz, the bandwidth was 4 MHz and the sampling rate was 62.5 MSamples/second. Signal power was as low as -90 dBm where steps are barely visible in contrast to the local oscillator signal at -20 dBm where the local oscillator signal is invisible. Testing setup and results of measurements are illustrated below.

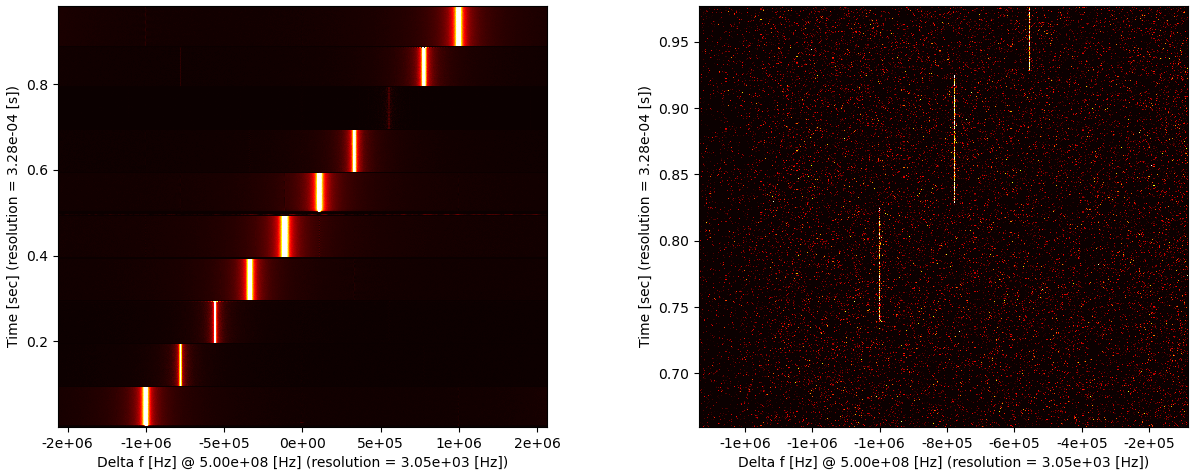

Fig. 4.1: Frequency sweep recorded by SDR at -20 dBm (left) and -90 dBm (right)

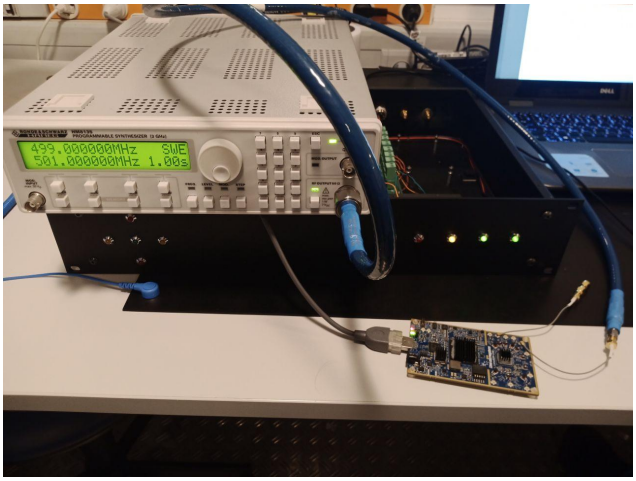

Fig. 4.2: Testing setup.

As one can see from Fig. 4.1 even when the signal is around -90 dBm, one can succesfully detect it utilizing the SDR.

The second part of the test measurement was conducted using a $^{235}U^{73+}$ beam at ESR with an intensity of $\approx 10^7$ particles at energy of 193.2 MeV/u. The SDR has been connected to the ESR 245 MHz Schottky cavity through the cascade of two amplifiers which generate amplification of 57.5 dB [39]. Results of the measurements and comparison to the NTCAP results are shown in Fig. 4.3 and Fig. 4.4

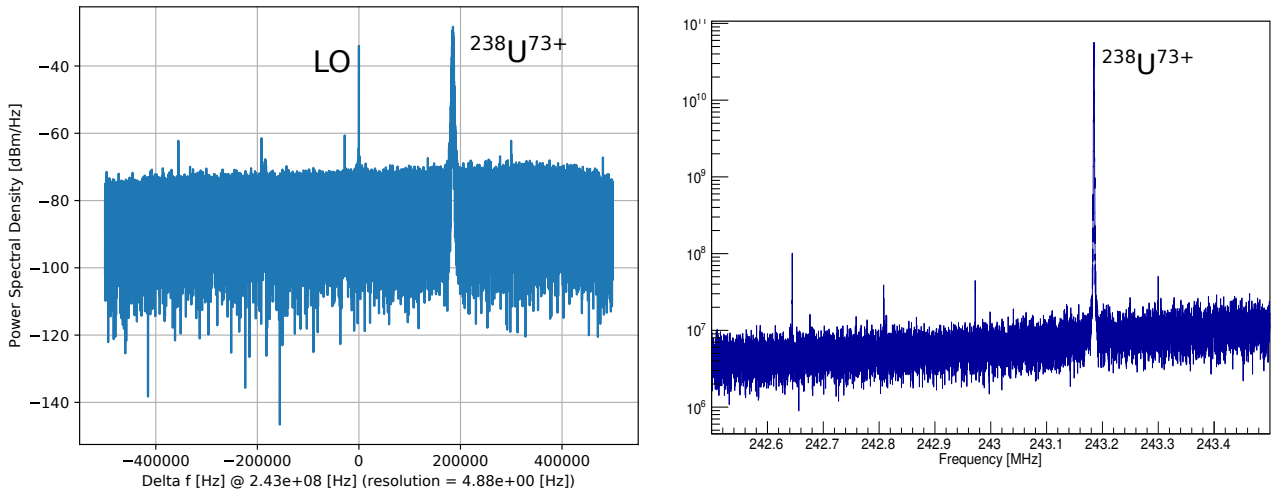

Fig. 4.3: 1D logarithmic scale spectrum of the uranium beam measured by SDR(left) and NTCAP(right). Peak in the middle of the left spectrum is a peak of oscillator of the Lime SDR.

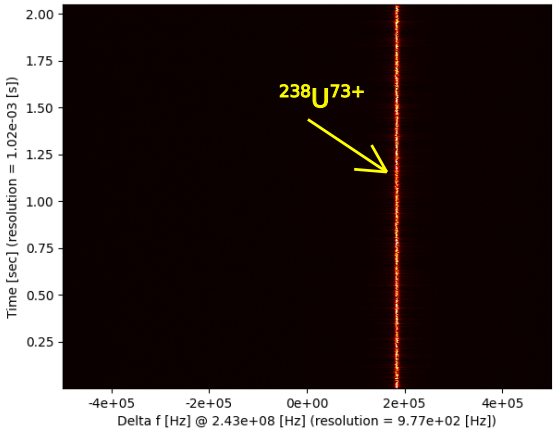

Fig. 4.4: 2D waterfall spectrum recorded by the software written for SDR.

Fig. 4.3 and Fig. 4.4 are strong evidence that SDR can be succesfully utilized for recording the data from beam despite the fact that data aquisition routine needs some adjustments in comparison to the existing NTCAP system. But the versatility of SDR is far better than the versatility of NTCAP.

During the above mentioned E143 experiment the application of the SDR as a DAQ for measurements in the isochronous mode has been investigated. The data has been recorded by NTCAP and SDR. The results of the SDR measurements together with captions of supposed elements are shown below:

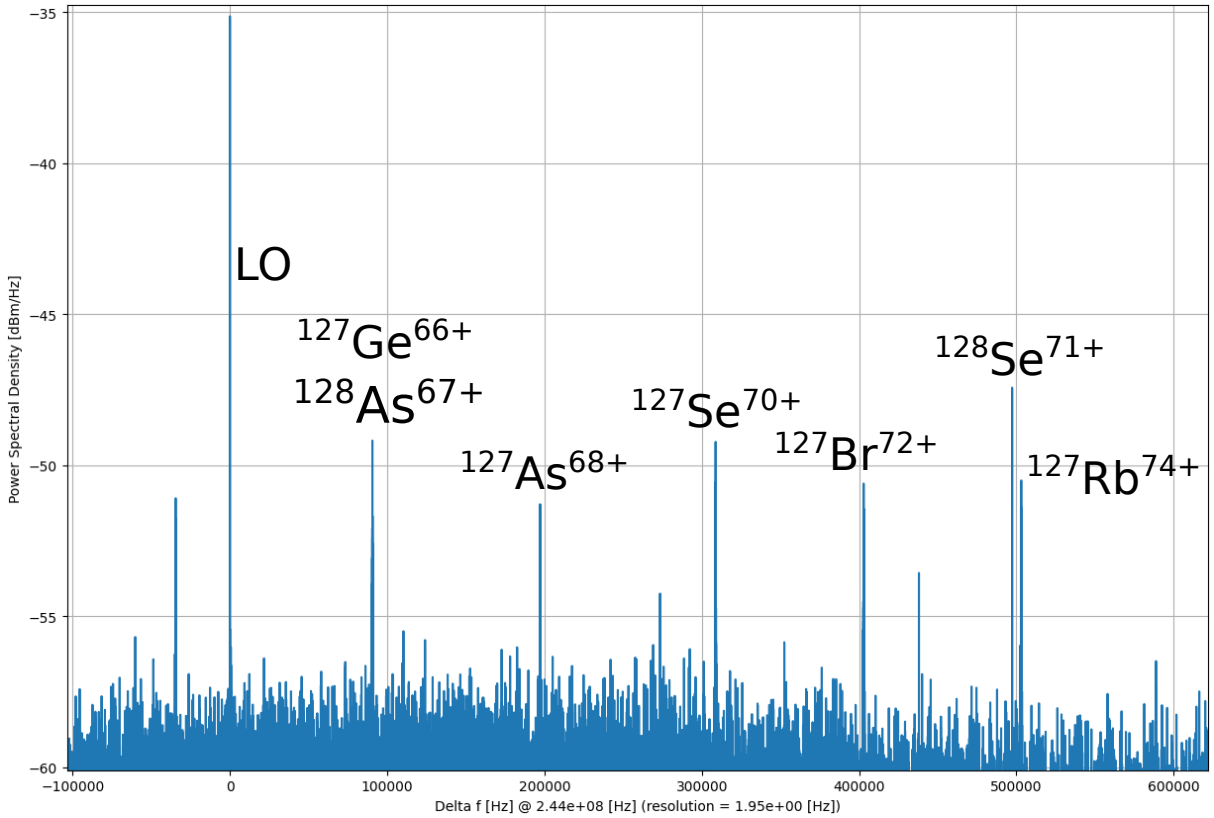

Fig. 4.5: Single ions broadband spectrum based on the data from E143 experiment. LO is a frequency of the local oscillator of the SDR.

Fig. 4.5 shows that Lime SDR can be used also for recording data during the experiments with isochronous mode which is the most important mode for this work. We emphasise that we have a broadband measurement of short-lived single ions. 22A preliminary identification has been done by comparing the theoretical frequency calculations with the peaks in the SDR spectra.

4.2 Noise Sources

In signal processing, noise is a general term for unwanted (and, in general, unknown) modifications that a signal may suffer during capture, storage, transmission, processing, or conversion [69]. There are several sources of noise in our chain. The most general noise is that caused by the thermal movement of electrons in employed materials. This thermal noise has been calculated as:

$$\frac{d\langle P_n \rangle}{df} = k_B \cdot T_K \tag{4.1}$$

where $\frac{d\langle P_n \rangle}{df}$ is a power of noise per unit of frequency, k_B is the Boltzmann constant and T_K is the absolute temperature in Kelvin. This noise power is uniform and approximately equal to -174 dBm/Hz.

In addition to the thermal noise which is present everywhere, there are other noise sources. In case of low frequency signals (below 50 MHz) noise which is caused by computers, electric instruments and switches could be higher than the thermal noise level. However, even a large Schottky cavity operates at frequencies above 100 MHz (245, 410 MHz for ESR Schottky cavities, 234 MHz for simulated cavities in Chapter 3, 502 MHz for the toy model in Chapter

5) and these noises could be neglected and damped by introducing bandpass filters oriented for the resonant frequency of the given cavity.

A signal from the Schottky cavity is rather small (according to equation (2.20) and needs an additional amplification. It is worth considering that each device in the amplification chain does not only amplify the noise on its input but also adds its own noise. To evaluate possible noise levels every amplifier has an important parameter: Noise Figure (NF). It shows degradation of the signal-to-noise ratio (SNR), caused by components in a signal chain. It is a number by which the performance of an amplifier or a radio receiver can be specified, with lower values indicating better performance. The noise factor (F) is a ratio of the output noise power to the input thermal noise power. The noise figure is simply the noise factor expressed in dB.

To evaluate the resulting noise factor one can refer to the Friis equation for noise factor:

$$F_{total} = F_1 + \frac{F_2 - 1}{G_1} + \frac{F_3 - 1}{G_1 \cdot G_2} + \ldots + \frac{F_n - 1}{G_1 \cdot G_2 \ldots G_n} \tag{4.2}$$

The consequence of the Friis equation is that the overall noise figure is primarily defined on the first stage of the amplification chain. This means that the first stage of amplification should always be a Low-Noise Amplifier (LNA). Then one can apply other amplifiers, bandpass filters, etc. If the gain is sufficiently high, then the total noise figure is mostly defined by the noise figure of the LNA. As an example of the amplification chain we may look to the suggested amplification chain for the R3 cavity. The first stage is an LNA ZX60-P103LN+ [70] from Mini-Circuits which has NF of 0.57-0.81 dB and gain of 24.04-22.75 dB in frequency range between 200 and 300 MHz. The second amplification stage is an operational amplifier ZKL-1R5+ [71] with NF of 2.83 dB and gain of 40.18 dB. The total gain is around 60.75-62.04 dB, and F is between 1.60-1.85.

To evaluate the change of the SNR we would use the same amplification system which consists of the amplifiers ZX60-P103LN+ [70] and ZKL-1R5+ [71]. In this example we will assume that the bandwidth of interest is 50 Hz. In the beginning the only noise which goes to the amplification chain will be a thermal noise with a total power of -157 dBm/Hz. The total power in the band of the signal from the single $^{78}Ge^{32+}$ ion will be -134 dBm/Hz with a peak height of -152 dBm. At this point the SNR is 3.3. Now we process the higher harmonic of the Schottky band and the signal of interest has the frequency of 200 MHz. The noise factor at this frequency is 1.60 and the total gain is 60.75 dB. The power of the peak now will be -96.25 dBm, and SNR will be 2.06.

Another source of the signal is the digitization of the continious signal. Assume that we record a continious signal with a sampling rate f_s and record M points. FFT processing can be seen as sending a time signal through a bank of M filters, each with bandwidth Δf (bin spacing) and determining the power at every filter output. $\Delta f = f_s/M$. As the number of frequency bins or M(or filters respectively) is increased, the filters become narrower and the power at each bin (power at the "filter output") becomes smaller. For exapmle, if M is doubled then Δf is halved, and the average noise level drops by 3 dB. According to the calculations of the SNR in Chapter 3, the spectral noise density will be -99.38 dBm/Hz. Now let's assume that we digitize this signal with the sampling rate of 1 MSamples/second and record it for one second. If we will do FFT over the entire amount of points, which defines our maximum frequency resolution, the average noise level N_o will be:

$$N_o = N_i \times \frac{M}{f_s} \tag{4.3}$$

According to equation (4.3), the average noise level will be -99.38 dBm. If we perform the FFT over a twice smaller amount of points then each bin will correspond to the twice larger amount of power due to the constant power density but twice larger width of the bin. In this configuration the noise level will be -96.38 dBm. An illustration is given in Fig. 4.6

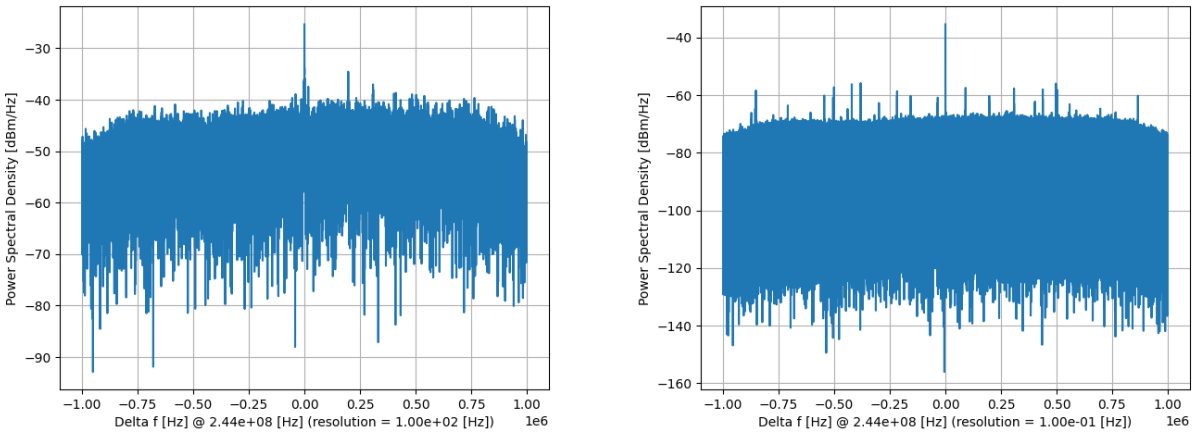

(a) FFT over $2{\times}10^4$ points.

(b) FFT over $2{\times}10^7$ points.

Fig. 4.6: The difference in SNR for different ranges of points for the FFT. Increasing the amount of the FFT bins by 1000 times decreases the overall noise level by approximately 30 dB. The spectrum has been measured during the E143 experiment.

As one can see from Fig. 4.6 increasing of the amount of bins by 1000 times led to a -30 dB drop of the average noise level which is the confirmation of the relation between the FFT points and the average noise level in equation (4.3).

5 Automated Measurement System and an Adapted Position-Sensitive Cavity Doublet Model

In this Chapter we describe the development of an automated motor-driven system which performs vertical and horizontal movements and has a feedback feature. This system can be used in conjunction with the SDR-based DAQ which was described in Chapter 4, or a vector network analyzer depending on the intended measurement. This system can be used for field profiling of future cavities by performing perturbation measurements using beads, rods and excitation measurements using wires as well as particle beams. By means of powerful motors with three degrees of freedom, this system can move the cavity doublet or individual cavities instead of moving the rod or bead which increases the accuracy of the measurements by reducing the vibrations. In a beam line setup, this would eliminite the need for beam steering elements or magnets.

In order to put ideas from the design in Chapter 3 to the test using the automated measurement system, a simplified toy model was designed and mounted on the motor-driven system. The design parameters of this cavity have been chosen such that the whole setup can additionally be tested in the S-DALINAC electron beam accelerator at the Technical University in Darmstadt.

S-DALINAC can generate electron beams at various in energies from 3 to 120 MeV with currents up to 60 μA. The frequency of the beam is 3 GHz [72].

As a result the time between two consequent bunches is 330 ps. Taking into account that electrons travel very close to the speed of light at the energy of 80 MeV ($\gamma = 158, \beta = 0.99998$), we calculate the size of the bunch to be 99 mm. An illustration is given in Fig. 5.1

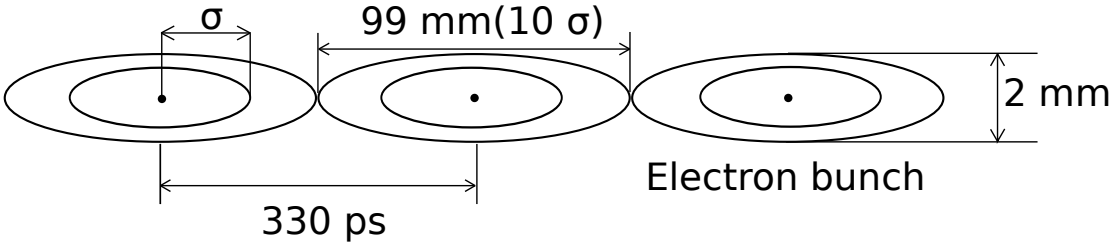

Fig. 5.1: Schematic illustration of the beam parameters at S-DALINAC.

As one can see from Fig. 5.1 the majority of electrons are travelling inside the bunch. The amount of electrons in the bunch for the current of 1 μA equals to 2000. We assume the bunch has Gaussian distribution and all electrons are within a range of 10 σ. Then we can calculate the length at one σ which is 33.66 mm. This value is crucial as it defines the size of the beam in the simulations as will be discussed below.

The idea of the experimental setup was to excite the cavity modes with the beam and to assess the dependency of the signal power on the cavity position relative to the beam. A bunch of electrons can be the source of a pulse signal which corresponds to the uniform band of frequencies. If a train of pulses is generated as a result of infinitely thin bunches of particles,

then their energy will gather around multiples of frequency regions, also known as bands. This effect is known from the storage rings, with the sole exception that in a storage ring the same particle arrives after a revolution, whereas in a linear accelerator different bunches arrive at fixed intervals. Mathematically speaking, due to the 3 GHz frequency of the electron beam we will have the first such frequency band at 3 GHz and no excitation of the cavity at lower frequencies is expected. But due to finite energy and imperfection in practical systems, there will be a fraction of the particle energy in lower parts of the spectrum as well.

For such beam parameters described above, the best solution would be to design a cavity with the fundamental resonant frequency at 3 GHz. On the one hand, a 3 GHz cavity will have a small radius of 100 mm and it would be unsuitable for making a transversal cavity for a beam pipe with the inner diameter of 40 mm. The latter is used at S-DALINAC. Additionaly the close proximity of the walls near the coupler will create a large capacitance between the cavity and couplers. As a result obtaining a clear signal will be a very challenging task. On the other hand, construction of a large cavity with a low resonant frequency of around 200 MHz will be impossible due to the mechanical restrictions of the experimental hall at S-DALINAC. The chosen solution was a cavity with the resonance frequency of 502 MHz.

Simulations using the CST Microwave Studio showed that the field inside such a cavity can get excited even at lower frequencies than that of the beam of 3 GHz. The results of the simulations are shown in Fig. 5.2.

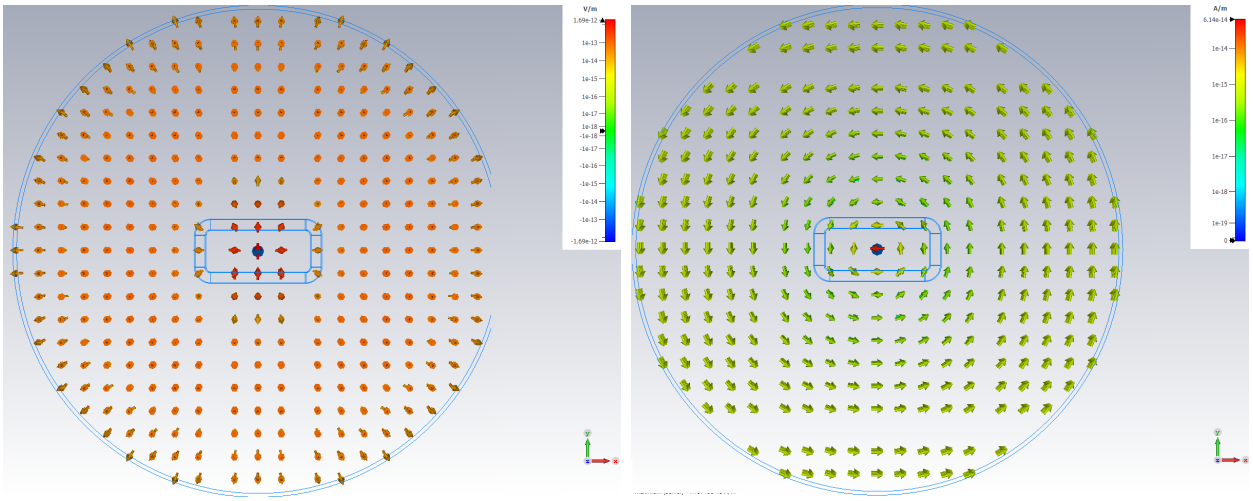

(a) Distribution of the electric field. (b) Distribution of the magnetic field.

Fig. 5.2: Excitation of the fundamental mode of the cavity. Simulations are normalized to 1 J energy in the cavity volume.

Fig. 5.2 has been created by using the Wakefield solver which calculates the wakefield potential. The longitudinal wake potential can be used to probe the interaction of the system of the cavity with the beam. The coordinate system is such that each field vector has 3 components. The wake potential can be used to describe the change of momentum on a test charge, which is at a distance s behind the excitation bunch [73]. The frequency domain representation is known as wake impedance, which itself is the measure of the response of the cavity to beam excitation. The longitudinal wake can be used as a measure for determining the frequency dependent longitudinal impedance, and hence as a measure for the expected signal power. The simulation has been carried out using a particle beam with a Gaussian distribution with a total charge of 2000 e^- and a σ of 10 mm. The simulation has been carried out at the resonance frequency 502.15 MHz and also off resonance for 100 and 1000 MHz. As one can see in Fig. 5.2, although this simulation shows the single pass limit, the excitation of the fundamental mode is visible.

5.1 Mechanical Restrictions

The position-sensitive cavity doublet has been designed to fulfill the conditions of the experimental area of S-DALINAC facility. The distance between the floor and the beam position is 945 mm which sets the maximum possible size of the cavity. Additionally two motor-driven systems were supposed to be installed directly under the cavity to allow transversal movement. Taking these points into account as well as the idea that the cavities have to have very similar resonant frequencies we used cylindrical and elliptical geometries. The produced cavity doublet is shown in Fig. 5.10.

5.2 Lab Measurements

5.2.1 Position Calculation and its Error

The uncertainty measurements were conducted utilizing the position-sensitive cavity doublet and consisted of four parts: frequency resolution of the spectrum analyzer or SDR, the error of the position measurements caused by the field distribution and coupler efficiency, precision of the motor, and error of the detector position measured by the linear resistive transducers. Linear transducers have a resolution of 0.05% which is equivalent to the error of 0.2 mm. The 12-bit ADC also has a maximum resolution of 400(stretching range of Megatron RC-35)/4096(resolution of 12-bit ADC) = 0.098 mm. The motor of the lifter does not accept the number of steps as it operates using the ISEL stepper motor which is responsible for horizontal displacement of the detector. The motor of the lifter has two states, on and off, and travels only in the vertical plane.

In order to increase the precision of the motor movement we chose to send a signal which switches it on 5, 10, or 15 times per second while reading the data about the position of the lifter's top plate from ADC. We continue making such steps until the desired position is reached (within the range of 1 mm). The mass which the lifter SwissBOY122M [74] can lift is non-linear and changes with the distance between the top and bottom plates due to its construction. Illustration of the power to distance between plates is given in Fig. 5.3:

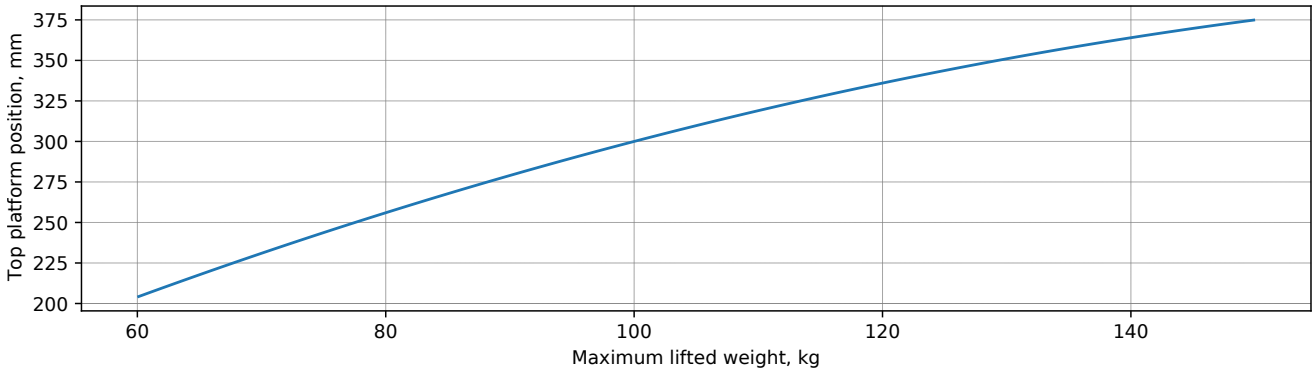

Fig. 5.3: Power over height dependency for SwissBOY 122M.

What one can see from Fig. 5.3, which has also been proven experimentally is that at lesser heights, the weight-bearing capability of the motor is reduced so it can perform very small movements upward when it has a peak but not a nominal current. This means that if we initiate a small number of steps per second there will be a delay because the peak current will only be present in the motor coils for a short amount of time. However, if the amount of steps per second is larger than 15, then the motor will not have enough time to reach the peak power needed to move the detector upwards. This issue disappears at larger heights, but the lifter

cannot be operated in this regime given the restrictions of the experimental hall. As a result, the working height of the lifter has to be between 110 and 150 mm because of the restriction that the beam pipe of the linac is placed 945 mm above the floor and we also would like to move our detector 40 mm in the vertical direction. Horizontal movement can be performed by the ISEL motor. Position error of the ISEL motor is negligible according to [40]. Results of the vertical movement errors for different speeds are given in Table 5.1.

Table 5.1: Measurements of the detector position by using data from ADC and caliper. Movement from 60 to 70 mm.

5 steps/second				10 steps/second				15 steps/second			
60 mm		70 mm		60 mm		70 mm		60 mm		70 mm	
ADC	Cal.	ADC	Cal.	ADC	Cal.	ADC	Cal.	ADC	Cal.	ADC	Cal.
58.61	58.7	70.69	71.45	60.09	60.6	70.13	70.95	60	60.2	70.1	70.5
59.47	59.7	70.67	71.3	59.58	59.85	70.09	70.85	59.98	60.4	70.4	70.5
59.45	59.3	70.66	71.45	59.89	60.35	70.17	70.85	59.92	60.1	70.01	70.5
59.29	59.6	70.38	70.8	59.59	59.80	70.12	70.7	59.95	60.0	70.02	70.4
58.83	59.0	70.77	71.5	59.78	59.8	70.06	70.6	59.94	60.3	70.02	70.4
59.51	59.5	70.73	71.3	59.85	60.05	70.03	70.5	59.98	60.1	70.02	70.6
59.26	59.1	70.32	70.8	59.89	60.3	70.2	71.0	59.96	60.0	70.0	70.5
58.86	58.7	70.78	71.4	58.48	60.5	70.13	70.4	59.88	59.9	70.05	70.7
59.4	59.5	70.49	71.5	59.68	59.5	70.07	70.7	59.81	70.59.7	70.03	70.3
59.03	59.3	70.04	70.8	59.63	59.6	70.17	70.6	59.92	60	70.01	70.35

According to the data obtained from the measurements, we chose a speed of 15 steps/second which generates the smallest error due to the smallest step size in terms of distance. Then we conducted a similar measurement but only for the speed of 15 steps per second throughout the working height range at S-DALINAC. We moved from 110 to 150 mm to cover the entire opening of the beam pipe. Results are shown in Table 5.2.

Table 5.2: Measurements of the detector position by using data from ADC and caliper. Movement from 110 to 150 mm. Speed 15 steps/second.

110 mm		150 mm	
ADC	Cal.	ADC	Cal.
109.93	111.0	150.01	152.2
109.87	110.15	150.01	152
109.95	111.3	150.02	151.7
109.9	110.7	150	151.85
109.91	111	150	152.1
109.98	111	150.01	151.7
109.96	111	150	152
109.97	110.8	150.02	152
109.9	111	150.01	151.8
109.88	111.1	150.03	151.7

Error of the position, σ was calculated as

$$\sigma = \sqrt{\frac{1}{n}\sum_{i=1}^{n}(x_i - \bar{x})^2} \tag{5.1}$$

$$\bar{x} = \frac{1}{n}\sum_{i=1}^{n}(x_i). \tag{5.2}$$

As a result real positions at 110 mm and 150 mm heights are 110.905±0.294 mm and 151.905± 0.171 mm respectively. To avoid possible problems during the measrurements with the beam we decided to lift the detector to the top position and work downwards for every set of horizontal movements needed for measurements of the field distribution inside the cavities.

5.2.2 Coupler Tests

The couplers made for the R3 cavities have been tested using the cavity doublet described in this Chapter. The measured results will be different in a future cavity for R3 compared to the results given in this Section. We placed the couplers in such a way that the flux of the electromagnetic field through the coupler loop is the largest (loop is parallel to the beam pipe). Results are shown in Table 5.3.

Table 5.3: Resonant frequencies for different cavities and simulations.

Cavity type	Resonant frequency, MHz
Cylindrical	502.935
Cylindrical sim	502.1
Elliptical	502.363
Elliptical sim	502.648

We measured the resonance frequency and quality factor for each combination of couplers for the elliptical cavity and for different couplers connected to the cylindrical cavity. According to our previous simulations [75] we can safely neglect the cross-talk effects between cavities. The results of measurements are shown in Table 5.4 and illustraded in Fig. 5.4. Words in the first two columns define the coupler. "Long" refers to the larger coupler, "Short" refers to the smaller coupler, and "Empty" refers to the blind flange instead of the coupler. Both couplers were connected to the 50 Ohm resistance, the same resistance as the vector network analyzer has. The small letter "o" means that the coupler was not connected to the 50 Ohm resistance and was left open.

Table 5.4: Comparison of different couplers for elliptical cavity.

Top coupler	Bottom coupler	Unloaded Q-factor	Coupling coeff.
Long	Empty	2015	1.884
Empty	Long	2015	0.457
Short	Empty	2019	1.276
Empty	Short	2019	0.894
Long	Long	2014	1.990
Long	Short	2693	3.309
Short	Long	2015	0.764
Short	Short	2021	2.116
Long	Long (o)	2014	1.734
Long (o)	Long	2014	0.452
Long (o)	Short	2017	1.437
Short	Long (o)	2015	0.774
Short	Short (o)	2019	1.116
Short (o)	Short	2022	1.226
Long	Short(o)	2015	0.427
Short (o)	Long	2015	0.472

To compare different couplers for the same cavity we chose to compare their coupling factor. It has to be as close as possible to 1, because in this case reflection in coupler will be the smallest. As we can see from Table 5.4, one can see that the best combination of couplers with coupling coefficient 1.116 is the short coupler connected to the network analyzer (later to SDR) on the top of the elliptical cavity and another short coupler in the open position (infinite resistance) on the bottom. However we have only two couplers, therefore we will use one small coupler on the top of the cavity and the bottom flange will be blind. A similar coupler has been created for the cylindrical cavity but due to the design of the cavity it can be placed only on the bottom position, because top position will be occupied by the tuner mechanism.

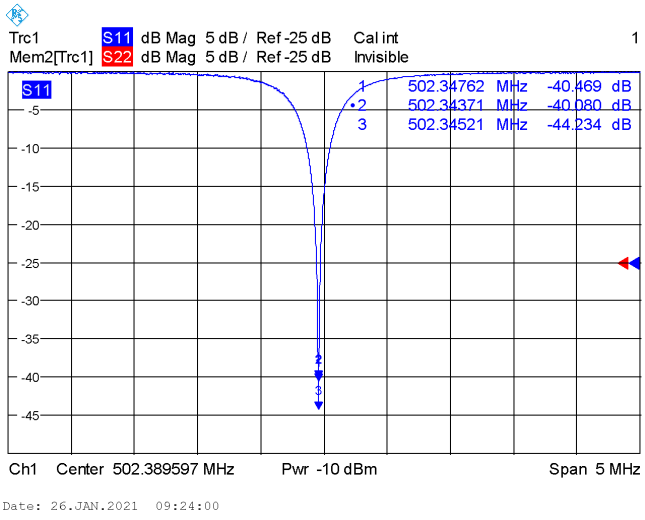

Fig. 5.4: The best combination of two small couplers. Bottom one is in open position.

As one can see from Fig. 5.4 the correct position, size and orientation of the coupler could greatly increase the loaded quality factor of the cavity.

5.2.3 Tuner Measurements

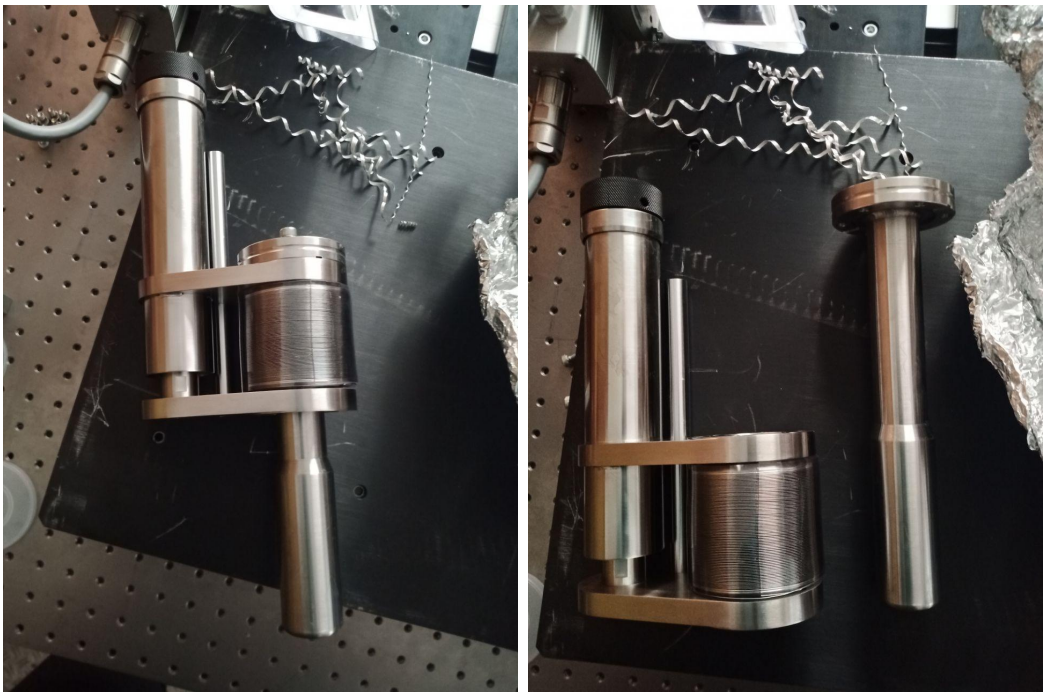

(a) Linear translator and 38 mm tuner. (b) Tuner installed in translator.

Fig. 5.5: Tuner for the cylindrical cavity.

We measured how the tuner affects the field inside the cylindrical cavity. At first, the tuner was completely inside and it was moved out with steps of 5 mm and the resonance frequency was measured together with the reflection coefficient and the quality factor. Results are shown in Table 5.5. The reference point was taken as the point of maximum insertion to agree with the scale of a linear translator. Measurements were done for the span of 1 MHz with 4001 points using the smaller tuner.

Table 5.5: Dependence of the resonant frequency on the tuner position.

Tuner position, mm	Central frequency, MHz	S11, dBm	Q-factor
0	502.935	-10.1	2247
5	502.879	-10.1	2247
10	502.77	-10.0	2259
15	502.666	-10.0	2259
20	502.556	-10.0	2283
25	502.436	-9.98	2296
30	502.285	-9.98	2296
35	502.142	-10.04	2295
40	501.996	-10.03	2307
45	501.845	-9.97	2320
50	501.7	-10.07	2319
55	501.564	-10.03	2332
60	501.424	-10.05	2332
65	501.297	-10.0	2345
70	501.192	-10.02	2344
75	501.112	-10.02	2330
80	501.06	-10.1	2385

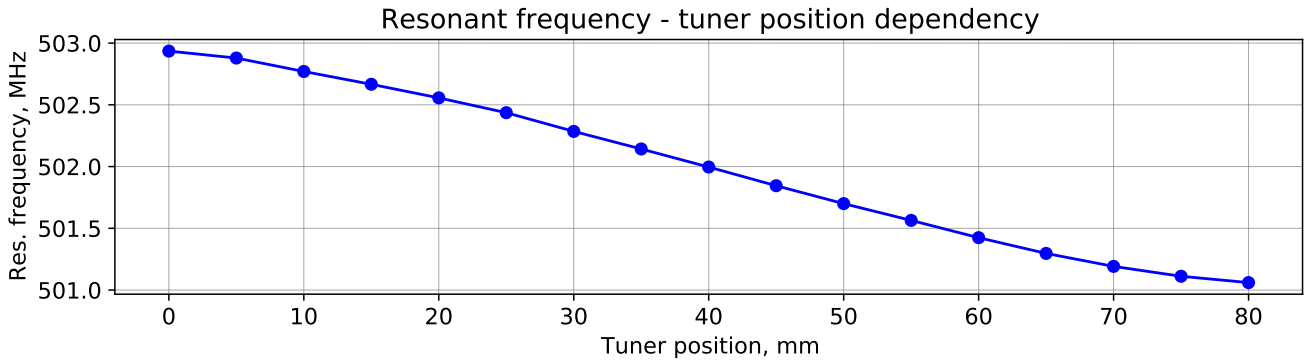

Fig. 5.6: Resonant frequency - tuner position dependency for the cylindrical cavity.

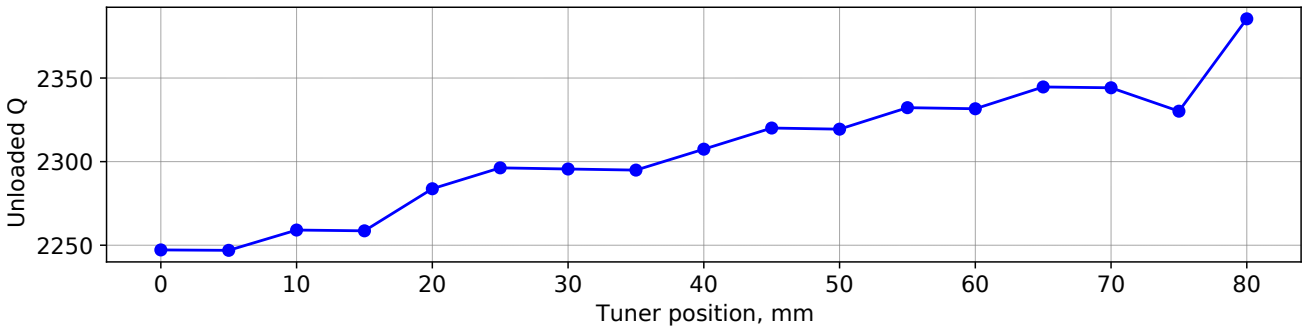

Fig. 5.7: Quality factor - tuner position dependency for the cylindrical cavity.

Fig. 5.6 and Fig. 5.7 show us that when inserting the plunger further into the cavity volume we change the volume of the field and this has unambiguous connection to the resonant frequency which agrees with theory [59, 60] and our simulations in Fig. 3.14. Also the unloaded quality

factor drops for around 0.5% due to the fact that losses on the surface become larger due to the additional metallic surface of the introduced plunger.

5.2.4 R/Q Map Measurements

One of the methods which can help to profile a transversal R/Q map is the measurement with a ceramic rod. Introducing a ceramic rod into the cavity changes the volume of the cavity. Additionally, due to material impurities (loss tangent) the rod can introduce some energy losses. But the largest influence is caused due to the material properties (ceramic has a much larger permittivity than that of air). The ceramic rod changes the local capacitance in the volume it occupies and thereby changes the distribution of $\vec{E_z}$. This in turn changes the resonant frequency of the cavity. Based on the difference between resonant frequency of the empty cavity and the cavity with ceramic rod inside one can calculate an R/Q value at the rod position, according to the equation below:

$$\frac{R}{Q} = \frac{2}{\pi^2} \frac{l_{rod}}{r_{rod}^2} \frac{1}{\varepsilon_0(\varepsilon_r - 1)} \frac{\Delta f}{f_0^2} \tag{5.3}$$

where l_{rod} is an efficient length of the rod. This effective length was measured as described in [39] using the rod itself, by slowly inserting it along the Z-axis from both sides to see where a significant change in reflection coefficient is visible. According to our measurements, it is equal to 40 mm. However, we can assume that effective rod length is equal to the thickness of the cavity because the rod is much longer than the thickness of the cavity ($l_{rod} \approx 100$) mm. r_{rod} is the radius of the rod. Δf is the difference between resonant frequencies between an empty cavity and one with a rod inserted into the center. f_0 is the resonant frequency of the empty cavity. Relative permittivity $\varepsilon_r = 9.7$ was taken from datasheet. $\varepsilon_0 = 8.85 \times 10^{-12}$ is the vacuum permittivity.

Using a tuner placed on the top of the cylindrical cavity we adjusted the resonant frequency of the cylindrical cavity close to the resonant frequency of the elliptical one (502.3(1) and 502.3(1) MHz). Then we introduced a ceramic rod into the beam pipe and checked how the resonant frequency of the elliptical cavity changes with different positions of the rod in the XY plane relative to the beam pipe. We mounted the ceramic rod on supports Vogel 341116 and moved the cavity doublet around it. For each position, we recorded a file that contains 4001 points of the frequency spectrum with a central frequency of 501.5 MHz and a span of 5 MHz. Then from each file, we extracted the resonant frequency (the frequency at which the reflection coefficient S11 is the smallest) and built a 2D surface of R/Q values. This was performed for rods with thicknesses of 3.15 mm and 5.5 mm.

We choose the coordinate system such that Z-axis is directed along the beam pipe and Y-axis is vertical. The X-axis is perpendicular to the beam pipe in the horizontal direction. At the beginning of the measurements, one has to calibrate the device to get rid of noise that could be caused by the cables and connections. Then we measured resonant frequencies of empty cavities. Due to the large quality factor of both cavities, one has to introduce a time delay between changing the position and consequent measurement of the resonant frequency. Delay in current measurements was 10 seconds. Results are shown in Fig. 5.8.

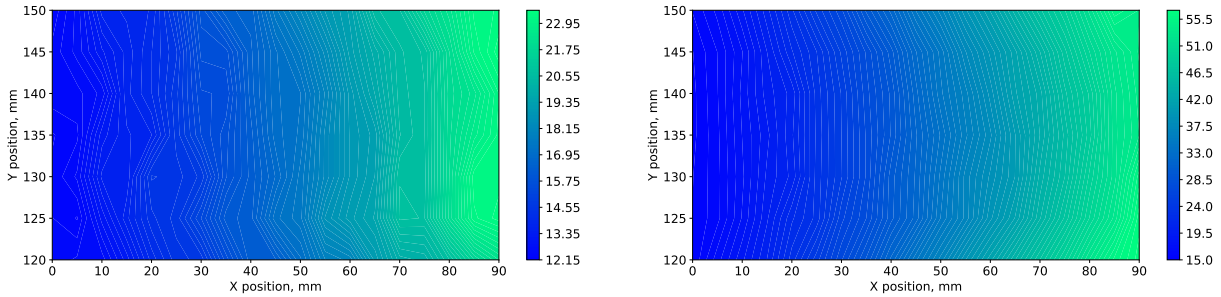

(a) 3.15 mm rod.

(b) 5.5 mm rod.

Fig. 5.8: R/Q profiling of the elliptical cavity for different rod thicknesses. The R/Q values are in Ohms.

The measurements of the field profile can generate a correct resonant frequency change only if the infinitely thin rod is introduced in the center of the cavity. The usage of the rod with diameter of 5 mm and its displacement lead to the accumulation of the error especially in the lateral direction. This experiment can prove our simulation and theoretical results only qualitatively. Change of the R/Q values in Fig. 5.8 is caused by smaller thickness of the ceramic rod which leads to a lesser change of the field volume inside the cavity and thus to a lesser change of the resonant frequency. As one can see from Fig. 5.8 the configuration of the R/Q profile qualitatively agrees with simulations. The thicker rod averages more of the field lines inside itself which leads to a less accurate but smoother picture.

5.3 Experimental Setup at S-DALINAC

On the next stage we installed the cavity doublet model including the automated motor driven setup and the SDR based data acquisition in the S-DALINAC facility at the Technical University of Darmstadt. We assembled and installed our setup in the experimental hall after the steering dipole. The schematics of the experimental hall is given in Fig. 5.9:

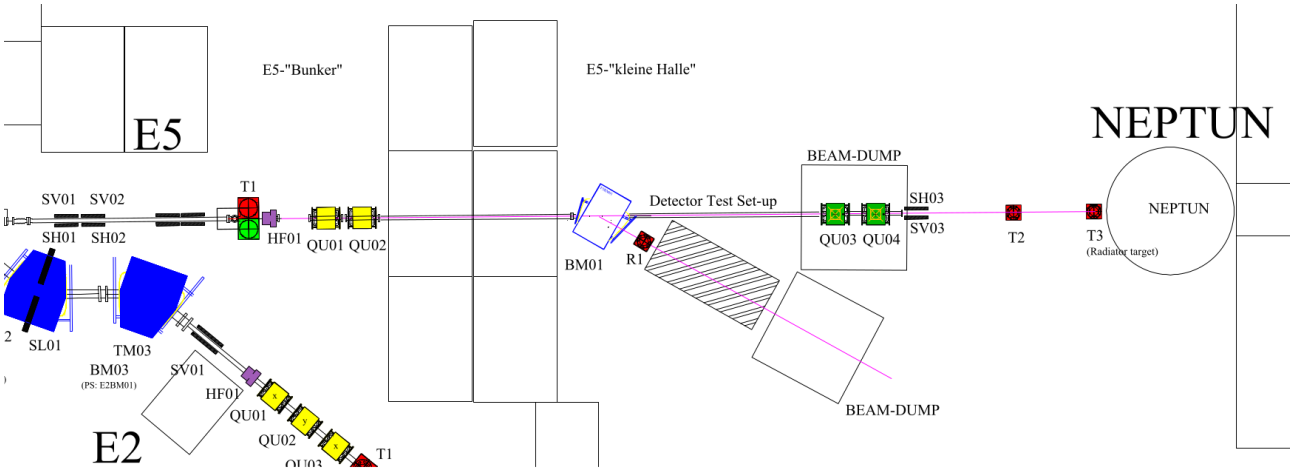

Fig. 5.9: Plan of the experimental hall.

More information about S-DALINAC accelerator and experimental setup can be found in [72, 76] and in Appendix 7.4.

The main goal of the experiment was to move the cavity doublet in lateral plane to investigate the dependency between the elliptical cavity position and an amplitude of the signal on the

oscilloscope and SDR. The fixed accelerator beam pipe does not allow any movement so to overcome this constraint we incorporated a vacuum-tight bellows. The entire setup is illustrated in Fig. 5.10

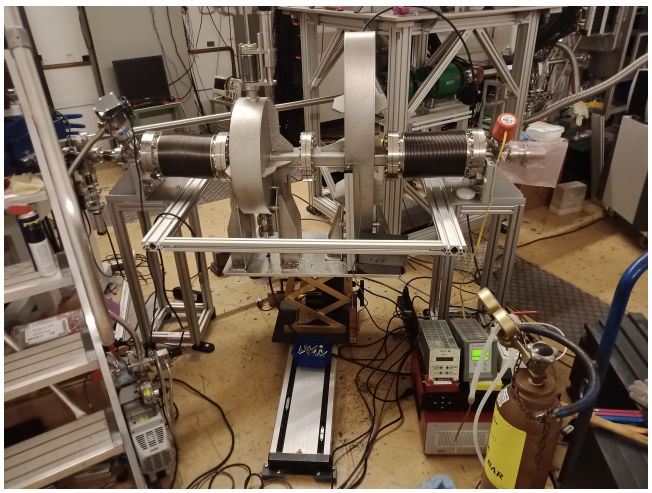

Fig. 5.10: Cavity doublet connected to the accelerator with RF chain, motors and vacuum equipment.

One can see in Fig. 5.10 the bellows sections between the cavities and outer pipes that allow us to perform the lateral movement of the cavity for 70 mm in any direction moving only the cavities. Our beam pipe has sizes of 100 mm $\times$ 40 mm and therefore the entire beam pipe opening can be covered without breaking the vacuum. The table and two green barrels behind the cavity are the beam dump and quadrupoles QU03 and QU04 related to the NEPTUN experiment [77]. We mounted both cavities on the same aluminum plate with a thickness of 20 mm in which we made a hole with diameter of 28 mm to insert RF cable with N-connector. This plate we mounted instead of the top plate of the SwissBOY M122 lifter which moves the cavities in the vertical direction. At this height it has enough power to move both the cavities and the tuner with a total system weight of $\approx$ 140 kg. The lifter we mounted on the top plate of the ISEL motorized unit which conducts horizontal movement of the cavities perpendicular to the beam trajectory. We also designed and assembled a rectangle made from ITEM profiles as well as the tables on sides to overcome the squeezing force of around 2000 N caused by atmospheric pressure. The grey vertical cylinder on the left is a turbopump and the red one on the right is a vacuum detector. On the bottom-right one can see an ISEL motor driver on the floor, SDR-based DAQ system placed on top and vacuum controllers on top of the DAQ together with the modified SwissBOY motor driver. The plastic bag on the right side covers a 40 mm opening which is connected to the 30 μm thick titanium foil which was needed for the adjacent experiment. More information about the setup can be found in Appendix 7.4.

As one can see in Fig. 5.9 a special steering dipole with name of E5BM01 has been installed to steer the beam to the necessary beam pipe. Detector tests took place in the gray shaded area between the dipole magnet and a beam dump. More information about dipole development and experimental hall layout can be found in [76].

The steering dipole has fixed position and an opening with a DN40CF flange inserted, with an inner pipe radius of 40 mm and the center of the pipe positioned at a height of 945 mm from the floor. This is the reference point for all future installations. The rectangular pipe which exits the magnet from the magnet has a reference marking which can be used for alignment of the whole setup. We made a precise alignment (1-2 mm error on the length of several meters) of the whole setup.

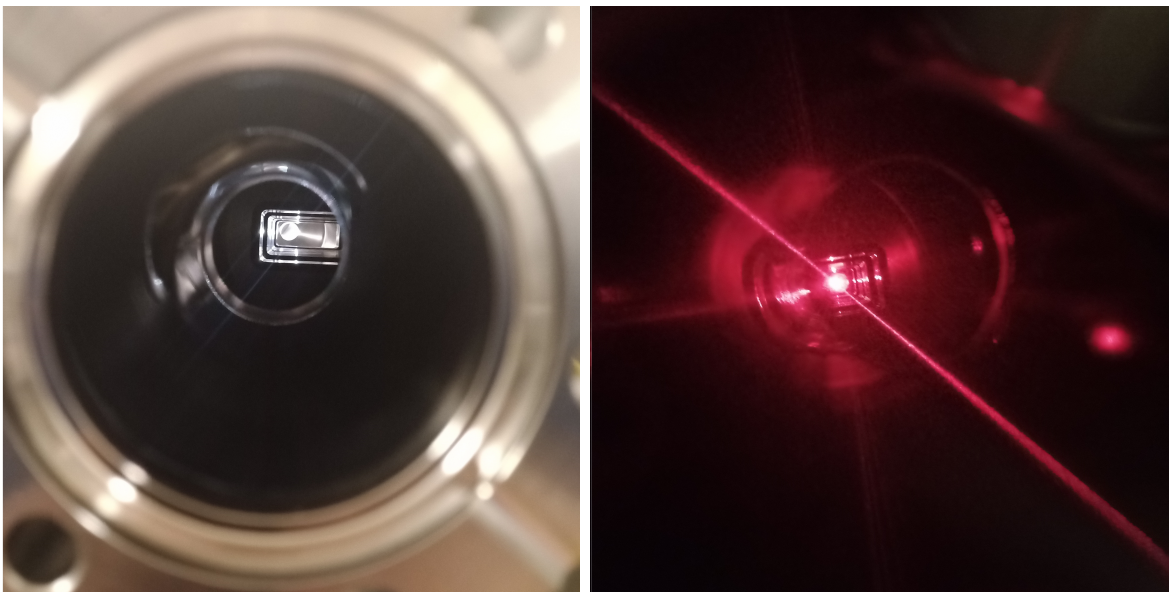

Fig. 5.11: Alignment of several sections using the point laser.

5.4 Wire Measurements at S-DALINAC

A thin wire connected to the signal generator has been put through the cavity doublet in the middle of the beam pipe for the purpose of exciting the modes of the cavity at different positions. The idea was to investigate the dependency between the wire position in the rectanglar beam pipe and signal amplitude. A similar experiment but for the dipole mode based position sensitive cavity has been done in [78].

However, due to the rather small size of the cavity, as well as the zero-impedance nature of the wire itself, the fundamental mode of the cavity could not be excited. Instead, the resonant mode acted like a planar waveguide that directly coupled the magnetic fields around the wire to the coupler. Because of this effect, the results of the measurements were unsatisfactory and the evaluation of the R/Q map was not possible.

6 Summary and Conclusion

The isochronous mass spectrometry is an efficient way to measure nuclear masses and lifetimes of exotic nuclides with half-lives down to tens of milliseconds. However this method must negotiate a larger momentum spread of particles circulating within the storage ring. For example, the electron cooler in the ESR can reduce momentum spread down to to 10^{-6}, which allows precise mass-measurements in case of particles and states which have half-lifes longer than several seconds. The isochronous mass spectrometry demands fast and sensitive detectors and these requirements are fulfilled by the resonant cavities. In the case of isochronous mass spectrometry, non-isochronous particles usually have much higher uncertainty (around 10^{-3}) caused by the anisochronism effect but this method can be utilized for the short-lived ions and states. During the measurements in the isochronous mode particles which do not fulfill the isochronicity condition ($\gamma = \gamma_t$) will have broader peaks in frequency domain.

A correction for this effect has been suggested in [55, 40] and described in this work. A new approach for the design of the Schottky cavities has been used in [39, 53, 40, 54, 22] as well as in this work. This approach allows construction of a cavity without a ceramic gap which makes it much easier to utilize together with increasing the quality factor [22]. Building on previous works, a new design of the position-sensitive cavity doublet for the R3 cavity has been created. The new position-sensitive cavity with an elliptical shape has unambiguous dependency of the signal amplitude on the position of the particle. The vertically stretched shape with an elongated side radius of 680 mm and narrow side radius radius of 400 mm allows position measurements with an error of 3% whereas the dependency of signal power on the vertical position of the particle is negligible. The idea of using the more strongly excited monopole mode instead of widely used dipole mode allows us to improve the signal to noise ratio. We fixed the sizes of the cavities according to the mechanical restrictions of the R3 facility, designed and compared different shapes, sizes and configurations of tuners for the above mentioned cavities and optimised the thickness of the cavities according to the transit time factors based on the conditions of the previous experiments at the R3 ring [18, 6, 58, 56, 57]. We concluded that for both cavities the best thickness is 200 mm. We produced the two pairs of magnetic couplers and succesfully tested them on the smaller cavity doublet. The necessary distance between the cavities in order to prevent the cross-talking effect has been calculated based on the cavity geometry and monopole mode frequency.

A new idea of the SDR-based DAQ system has been suggested in this work. The SDR is a small, versatile device which can be used alone or as an easily-scalable system in case of many detectors. It allows us to record data with sampling rates up to 61 MSamples/second and digitize them in close vicinity of the detector which will reduce signal losses in long cables. The SDR can be programmed using open-source software, in our work we used Python3 and an open-source library SoapySDR [79]. Using these two instruments we created a program which initializes the SDR, starts the calibration routine and executes a measurement with user-defined parameters such as central frequency, sampling rate, time of measurement, bandwidth, channel and filename for the file where binary data will be written. The SDR can simultaneously record data from two channels without an external trigger system which is a very useful function for the position-sensitive cavity doublet. The program for the SDR can be found in Appendix 7.9. This device and corresponding program have been tested in the lab with the signal generator as well as on several experiments in the ESR at GSI with a particle beam. A set of data

during the experiment in the isochronous mode has been gathered and a preliminary peak identification according to the theoretical predictions has been completed. The distributed Schottky detector systems at the Collector Ring in the planned FAIR facility [80] in the future can be supplemented with an SDR-based DAQ system.

A fully automated motor-driven measurement system has been developed that can be used to measure the field profiles of such cavities in conjunction with the above mentioned SDR based data acquisition system.

A toy model of such a position-sensitive resonant Schottky cavity doublet has been designed, constructed, manufactured and tested using the automated measurement system in the lab as well as at the linear accelerator S-DALINAC at Technical University of Darmstadt. Several lab tests such as ceramic rod or wire measurement have been carried out in order to qualitatively prove the transversal R/Q distribution in the elliptical toy model cavity doublet. Trends in the simulation results as well as in theoretical expectations have been successfully confirmed. Additional to lab measurements and field profiling, the toy model was installed in the beam line of the S-DALINAC in Darmstadt to be tested with an electron beam, based on the wake field simulations of possible excitation.

This toy model was installed on the automated motor-driven system and equipped with the data acquisition system. All the necessary preparations for the test with an electron beam were carried out, including alignment, vacuum tests, design of the system to compensate longitudinal atmospheric pressure, and design and assembling of the vacuum tight connection which allows transversal movements. We designed and assembled a vacuum system which was necessary to fulfil the requirements of the S-DALINAC accelerator facility.

The beam test of the toy model was delayed several times due to technical difficulties at the S-DALINAC accelerator facility and the conditions of the pandemic in the years 2020 and 2021. Finally in the designated beam time of September 2021, the accelerator could not be operated in its full potential due to a still unrecognised source of beam loss in the main accelerator section, that caused an irregular amount of radiation. The latter lead to the decision of the accelerator division to reduce the intensity of the operation during that beam time block down to a small fraction of the planned value (approx. 100 nA), which was far below any possible excitation level for our toy model cavity. As a result the toy model cavity could not deliver any measurable signal.

As an outlook on the current work, it is possible to redo the measurements with the toy model in the S-DALINAC environment in a future beam time block, given that the technical difficulties in S-DALINAC have been taken care of. Alternatively, based on the design provided in this work, we suggest to proceed with the manufacturing and testing of the cavity designed in Chapter 3 inside the R3 storage ring in RIKEN. The latter provides an additional advantage of single particle operation where the particles are known a priori as described in [81]. Based on the existing experiences of single particle sensitivity inside heavy ion storage rings [23, 82] and specifically inside the R3 storage ring [6], one can expect a rather good signal to noise ratio with respect to the sensitivity of the individual cavities (cylindrical and elliptical). Based on Fig. 3.8 and Table 3.2 and the calculation given in the Chapter 3 on the ^{78}Ge ion, it is expected that the position of the centroids will be clearly discerned. Of course a detailed understanding of the specifications and limitations of the R3 storage ring is needed to make successful use of this information in an online mass measurement experiment.

7 Appendix

7.1 Field Distributions for Different Modes in Elliptical Cavities

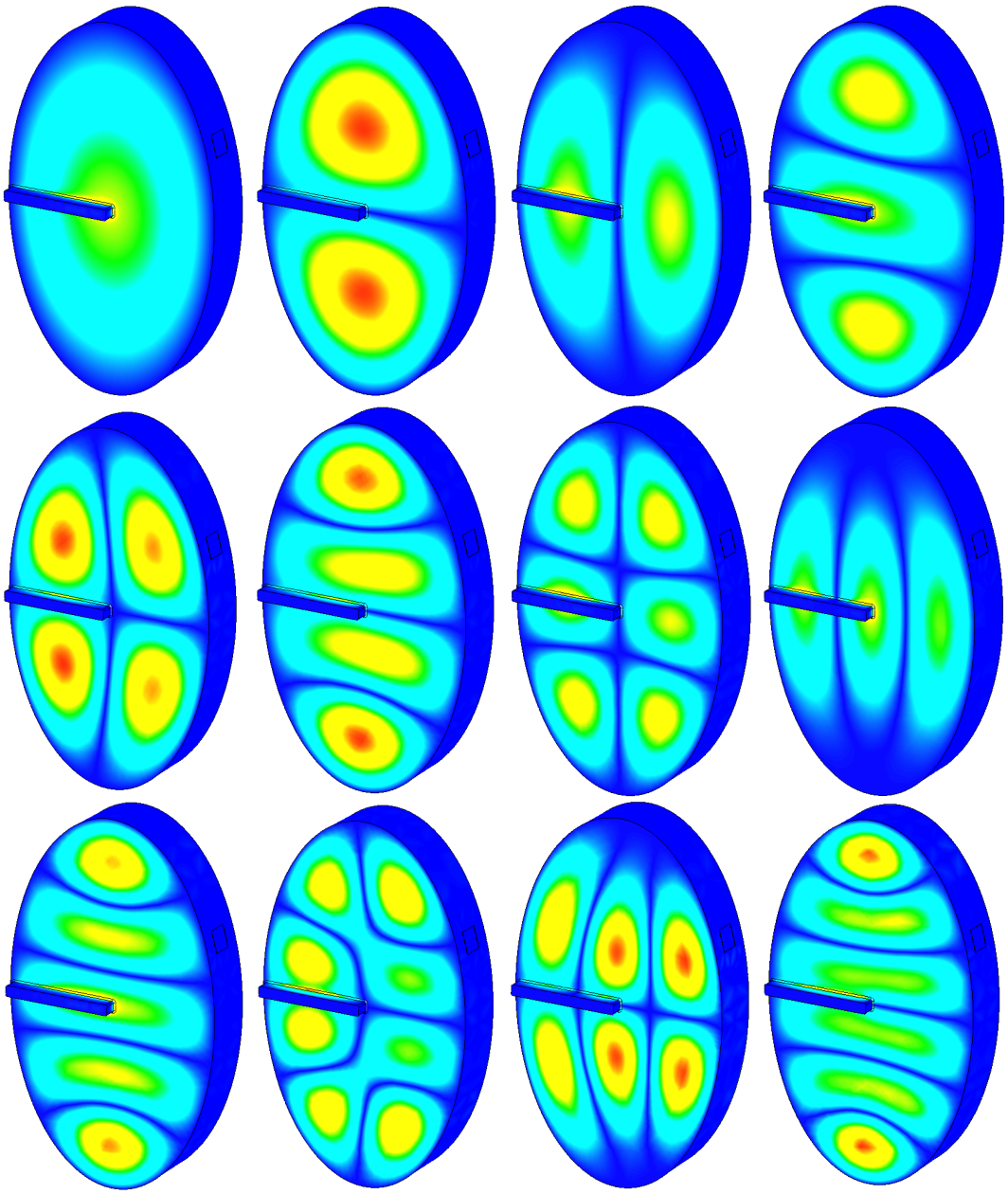

Fig. 7.1: Distribution of $\vec{E}_z$ in elliptical cavity for R3 with thickness of 200 mm. First 12 modes.

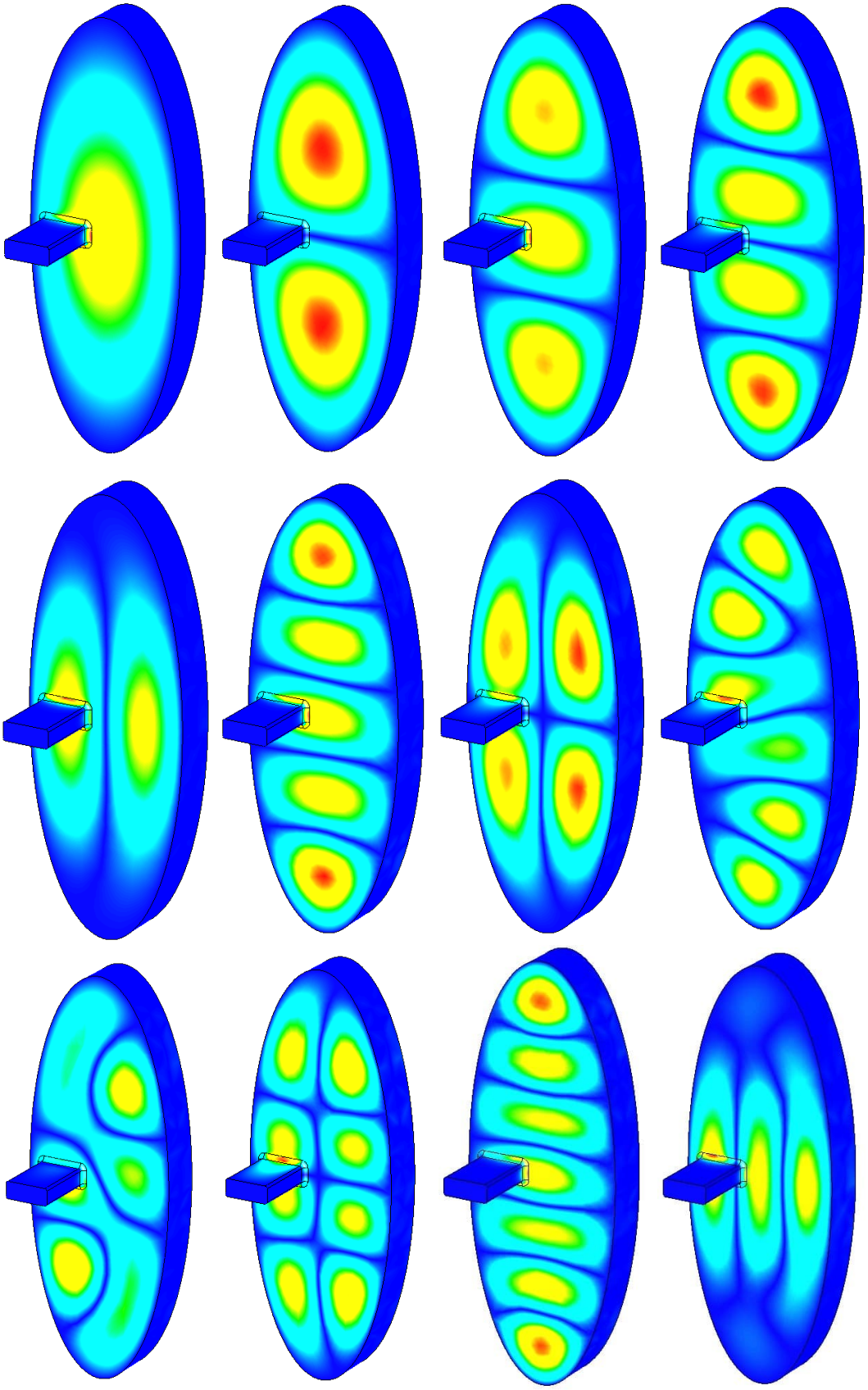

Fig. 7.2: Distribution of $\vec{E_z}$ in elliptical cavity for DALINAC. First 12 modes.

7.2 Simulations for the S-DALINAC Prototype

A similar set of simulations as for the R3 cavities were conducted for the cavities of the adapted prototype. For the beam pipe with an outer width of 100 mm and wall thickness of 2.5 mm this equation (3.1) gives a cutoff frequency of $f_0 = 1538$ MHz. Results of simulation of an EM field inside the beampipe without cavities is given in Fig. 7.3

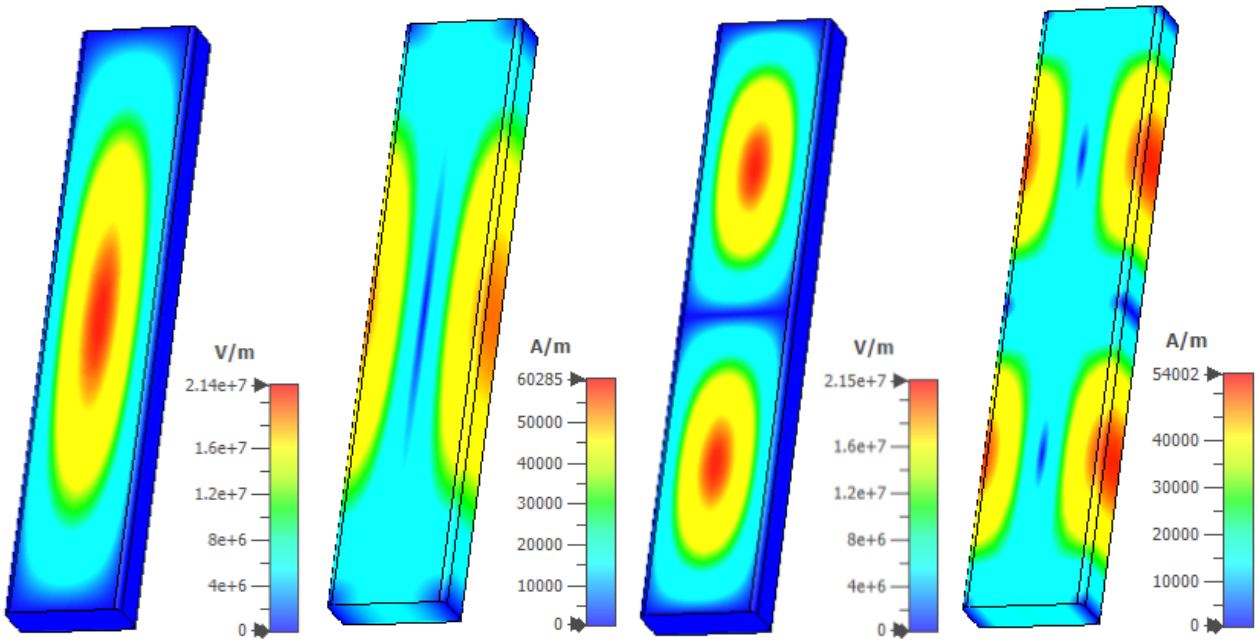

Fig. 7.3: EM field distribution for the first two eigenfrequencies for a beampipe without cavities.

The difference between cutoff frequencies given by the analytical solution and simulation can be explained by 2 mm edges blending that is taken into account in simulation but ignored during analytical calculations.

The same simulations for a couple of cavities have been conducted to investigate the cross-talking effect. The resonant frequency of the monopole mode is around 502 MHz, beampipe sizes are 100 × 40 × 500 mm. The cylindrical cavity diameter is 230 mm. Size of the elliptical cavity is 910 × 340 × 100 mm. The walls of the cavities are made from 8 mm steel. More information is given in Fig. 7.20. Simulation results are given below:

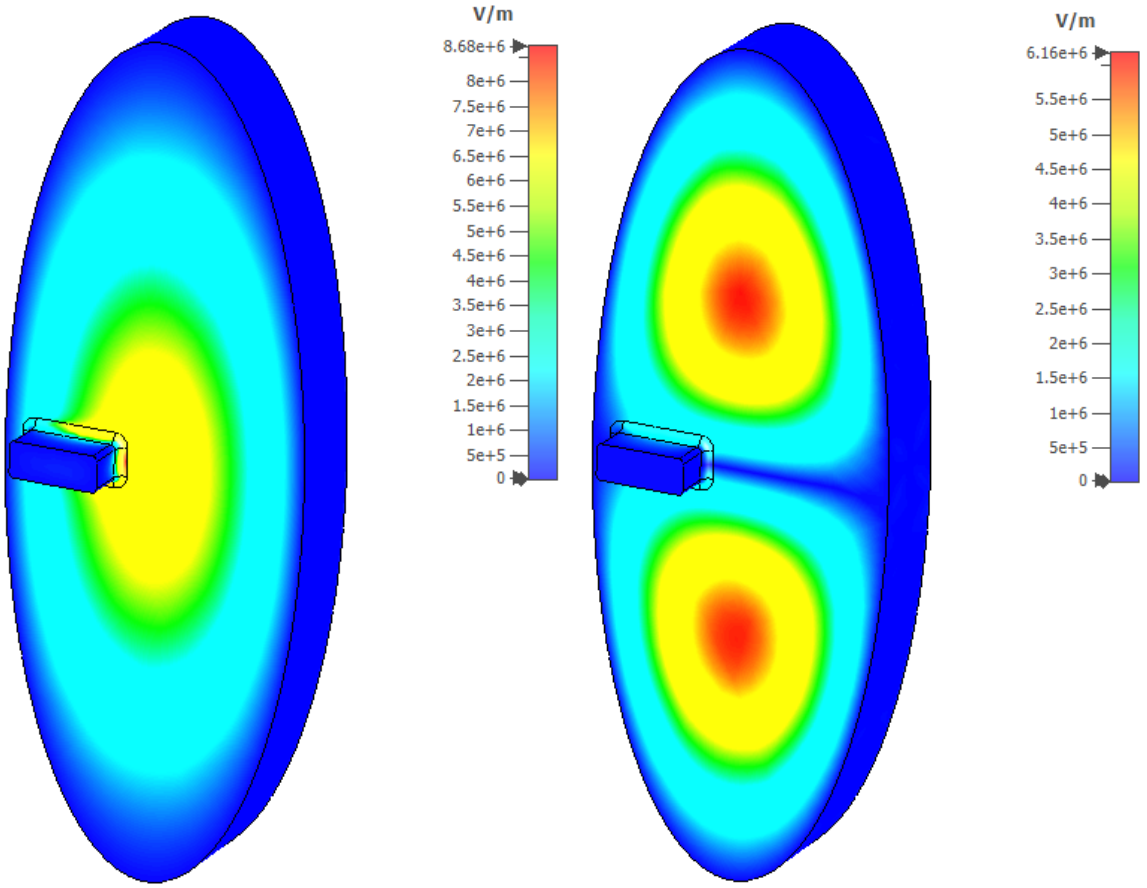

(a) Monopole mode. (b) Dipole mode.

Fig. 7.4: Field modes simulation for the elliptical cavity.

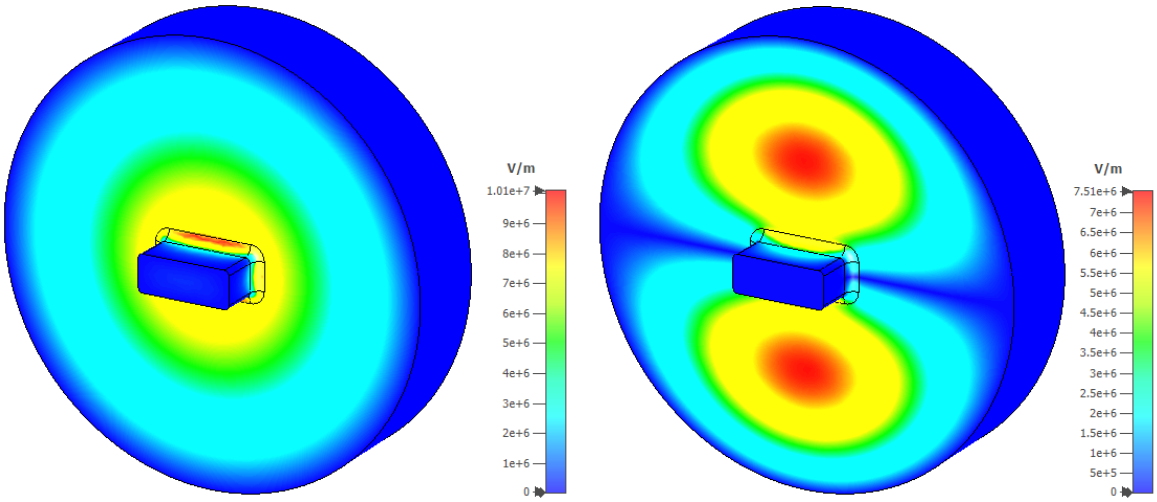

(a) Monopole mode. (b) Dipole mode.

Fig. 7.5: Field modes simulation for the cylindrical cavity.

Simulations of the structure which consists of two consequent cavities were conducted later. This was necessary to overcome the issue with the Eigenmode solver. An illustration is shown in Fig. 7.6. Profile of Z component of the EM field long the Z-axis in the middle of the beam pipe was taken and "0" point for each plot is the center of the corresponding cavity. Results are shown in Fig. 7.7.

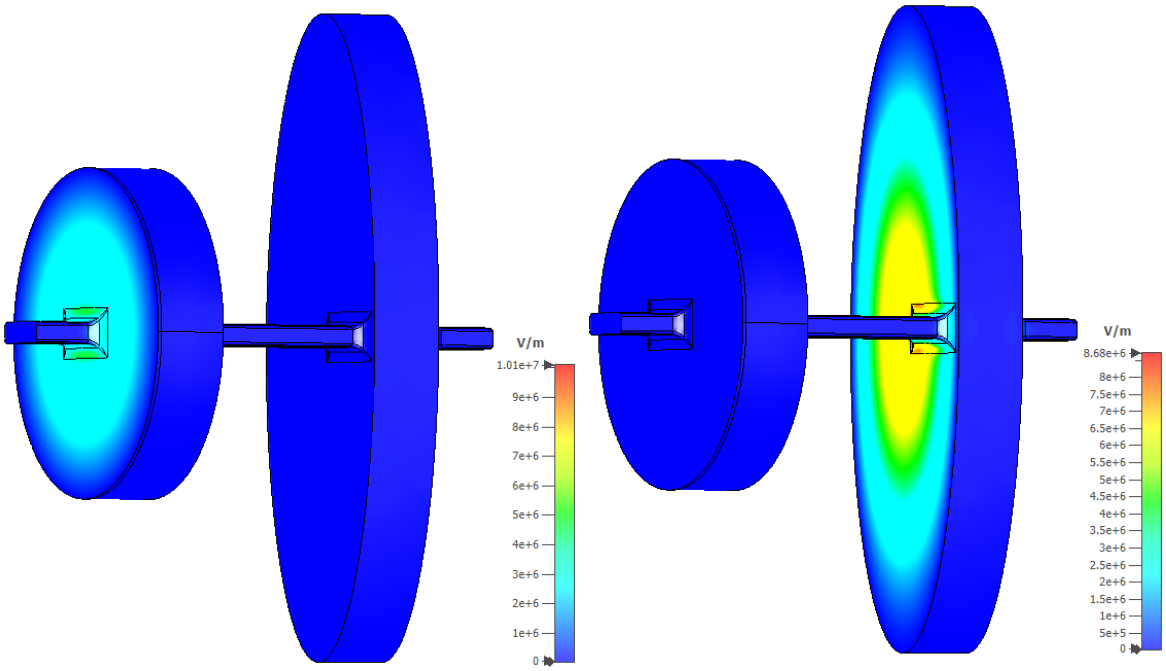

(a) First calculation. (b) Second calculation.

Fig. 7.6: Field modes simulation for structure with two cavities.

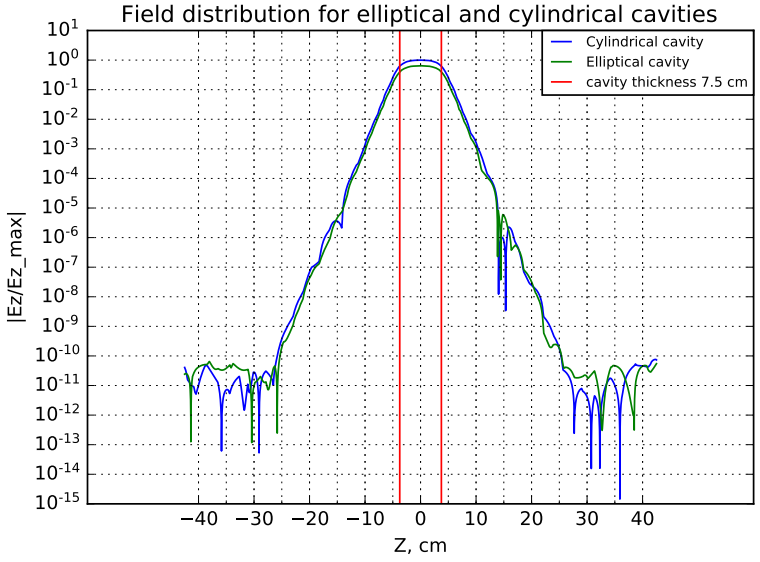

Fig. 7.7: Longitudinal field distribution along the center of the beam pipe. Published in [75].

According to Fig. 7.7 we decide that if the field intensity of the cylindrical cavity reduces by 4-6 orders of magnitude along the longitudinal symmetry axis of the beam pipe one can neglect its influence on the resolution of the position-sensitive cavity. So field distribution error caused by the interaction between EM fields of the cylindrical and elliptical cavities on the distance between cavities centers more than 300 mm is negligible [75]. For the R3 cavities, the distance has to be at least 400 mm for the drop by 4 orders of magnitude. This means that the larger is the beam pipe opening the more energy from the field inside the cavity goes to the beam pipe decreasing, among the other reasons, the unloaded quality factor. The blueprints of the constructed cavities one can find in Appendix 7.6.

7.3 TCAP, NTCAP and SDR Comparison

There were two DAQ in GSI which were used to read and store data from Schottky cavities at ESR, TCAP, and NTCAP [63, 64]. We suggest using a software-defined radio SDR instead of them. Comparison of these three systems are shown in Table 7.1.

Table 7.1: Comparison of different DAQ at GSI for Schottky cavities.

Name	TCAP	NTCAP	SDR
Max. Sampling rate, MHz	0.624	40	61.44
Max. Bandwidth, MHz	0.312	20	30.72
Data transfer, Mb/s	40	1000	387

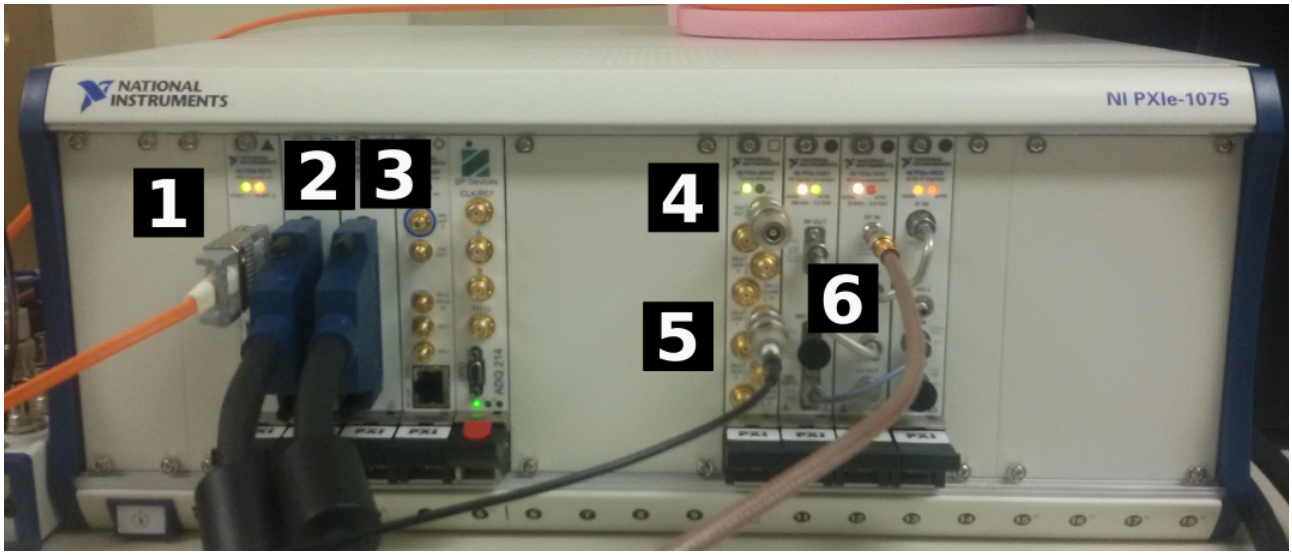

Fig. 7.8: NTCAP DAQ. Picture taken from [64], p.133 .

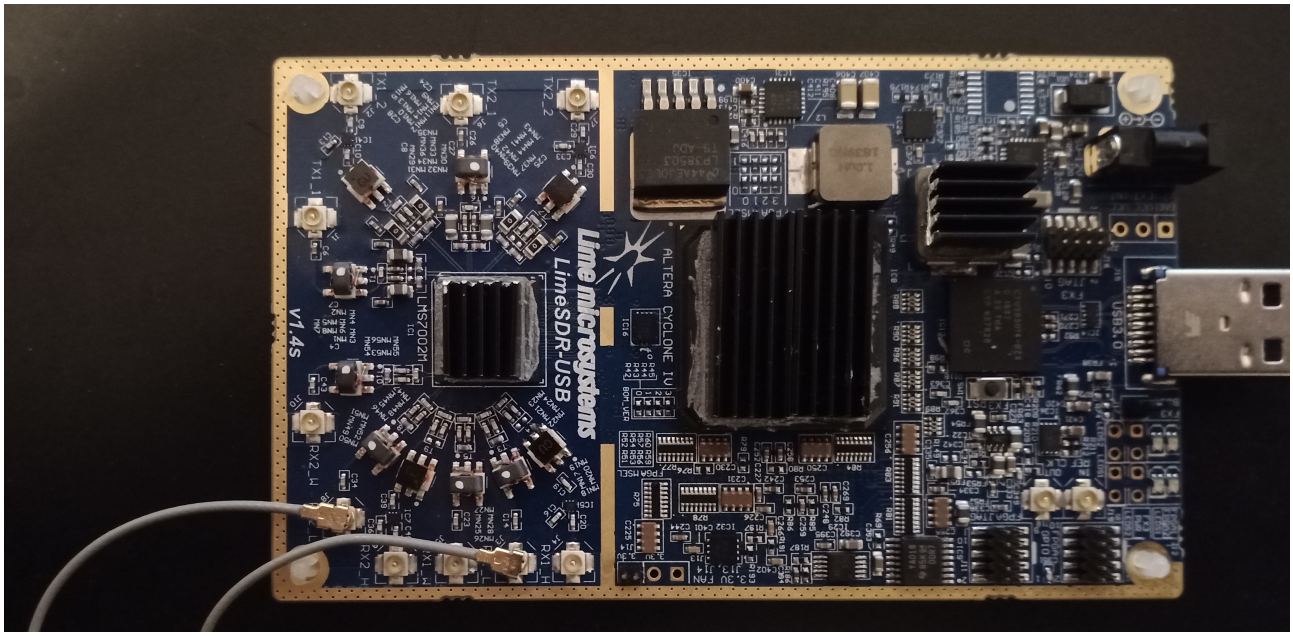

Fig. 7.9: SDR DAQ.

7.4 Driving System

The mechanical part consists of two motor-driven systems. The total weight of the detector system is around 140 kg which restricts our choice of lifter. After a thorough investigation of possibilities, we figured out that the best solution will be the lifter SWISSBOY 122M, mounted on the plate, driven by an ISEL stepper motor.

7.4.1 SWISSBOY 122M Lifter

The lifter can operate only in continuous mode by pressing a button due to the design of its driver. Illustration is given in Fig. 7.10. To overcome this issue, we modified the control box of a lifter by adding two 3-pin connectors for the remote control and developed a small circuit with relays [83]. When one relay is shorted, the lifter platform goes up, another relay shorting moves it down. To avoid potential damage to the motor, we strongly recommend not to short both relays simultaneously.

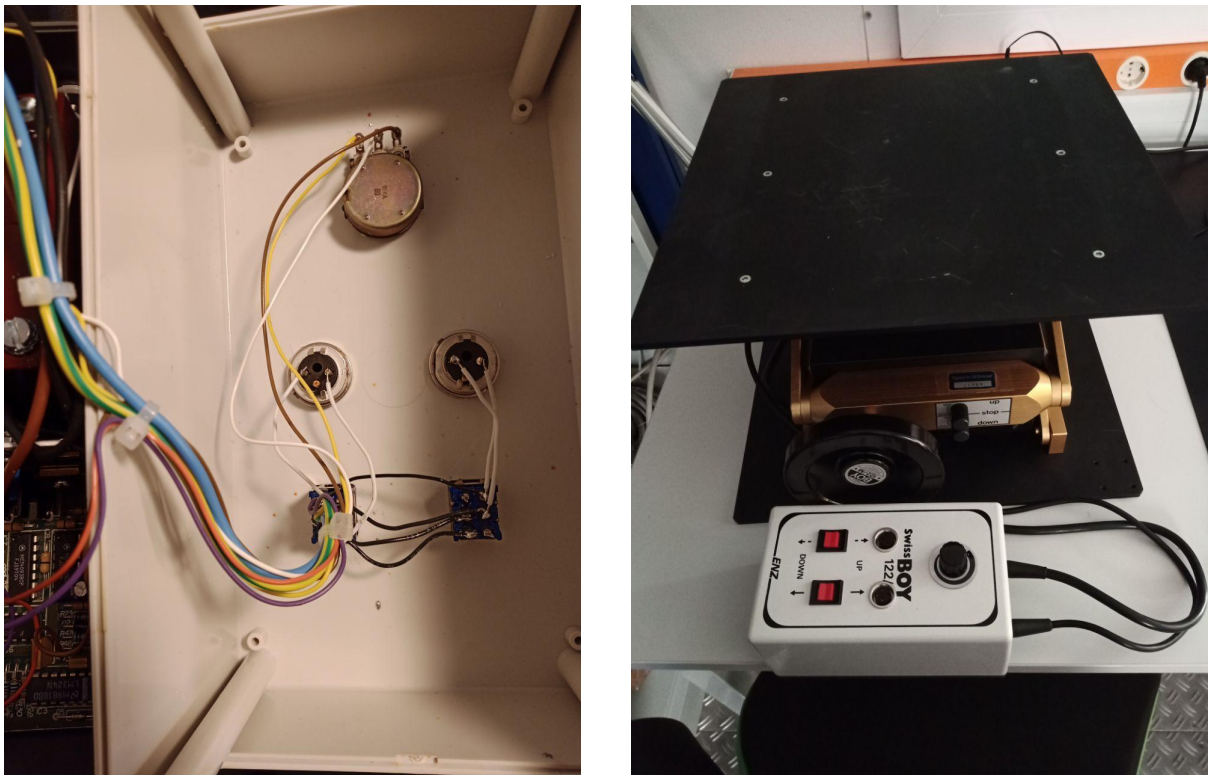

(a) Modified motor control box. (b) Lifter and control box.

Fig. 7.10: Modification of a SwissBOY122M control box by adding 3-pin connectors for the remote control through the relays by microcomputer Raspberry Pi (RPi) [84].

Relays are the power electronics part. To prevent back current flow through the RPi, we decided to use the ULN2003A Darlington couple array, which is an array of a couple of NPN transistors with reverse logic [85]. This means that when a logical "1" is presented in its input, the corresponding output will have logical "0" and vice-versa. Amplification is done by adding a 5V DC generated by the TRACO power supply to its power input. An example of a circuit is shown on the Fig. 7.11

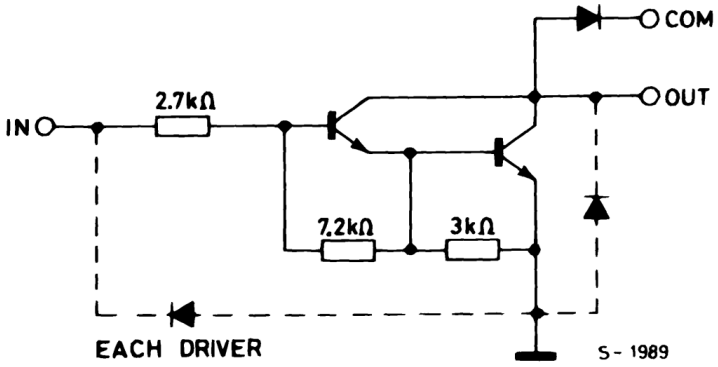

Fig. 7.11: ULN2003A inner circuit. COM has to be connected to +5V.

As one can see in Fig. 7.11 the ULN circuit is made to prevent backflow of the current from the load such as a motor to the sensitive operating electronics.

7.4.2 ISEL Stepper Motor and Driver

(a) Driver rear panel.

(b) Driver front panel.

(c) ISEL stepper motor with platform.

Fig. 7.12: ISEL stepper motors and their driver.

The horizontal movements are executed by the ISEL stepper motor. It has mechanical terminators on the moving line which stop the movement of a plate. The driver of the motor can be remotely operated by sending commands in byte format using a USB port. It supports commands, which define the number of steps (even 1/32 step division is possible). Motors and driver are shown in Fig. 7.12

7.5 SDR-based DAQ

The operation of the motor system with a position-sensitive detector on it in a radioactive area demands remote control and DAQ systems. In this Section, we will describe electronic devices that were used for the design of those systems and the reasons why they have been chosen. The SDR itself has been described in Chapter 4.

7.5.1 Megatron Potentiometers

The position of the detector is one of the utmost important parameters during all measurement cycles. It is possible to move the detector in a horizontal direction by using the ISEL motor with great accuracy. However, the lifter has no function of step calculation, which leads to the idea that we have to provide an additional independent position measurement system. For this, we chose a linear potentiometer by Megatron. It is a simple voltage divider that demands feeding voltage and ground connection as inputs and returns a voltage that depends on the distance between its two ends. Every linear potentiometer has its electrical travel and resistance, which have to be taken into account. We chose model RC35 [86] because its sizes and resistance were suitable for our application. The device is illustrated in Fig. 7.13

Fig. 7.13: RC35 linear potentiometer.

Linear potentiometers have a resolution of 0.05%, but we are also limited by the resolution of our ADC. The main function of ADC in our case is to get a number from the voltage on the potentiometer output. Unfortunately, the used microcomputer Raspberry Pi 3B+ (RPi) [84] has no ADC. That's why we chose ADC MCP3204 from Microchip [87]. It is a 4-channel 12-bit ADC that can be connected to RPi by the Serial Peripheral Interface (SPI) bus. It needs to be connected to 5V DC for operation and to the reference voltage used for displacement measurements. In our case, it is also 5V. To get the stable voltage we connected the potentiometer to the 5V pin of the RPi. The connection between the RPi and MCP3204 is illustrated in [87] and on Fig. 7.22.

It is worth mentioning that potentiometers do not give a precise position immediately. To receive stable number one has to wait several seconds. Additionally, we average 100 data points from potentiometers to reduce the error of the position measurements.

7.5.2 Assembled DAQ

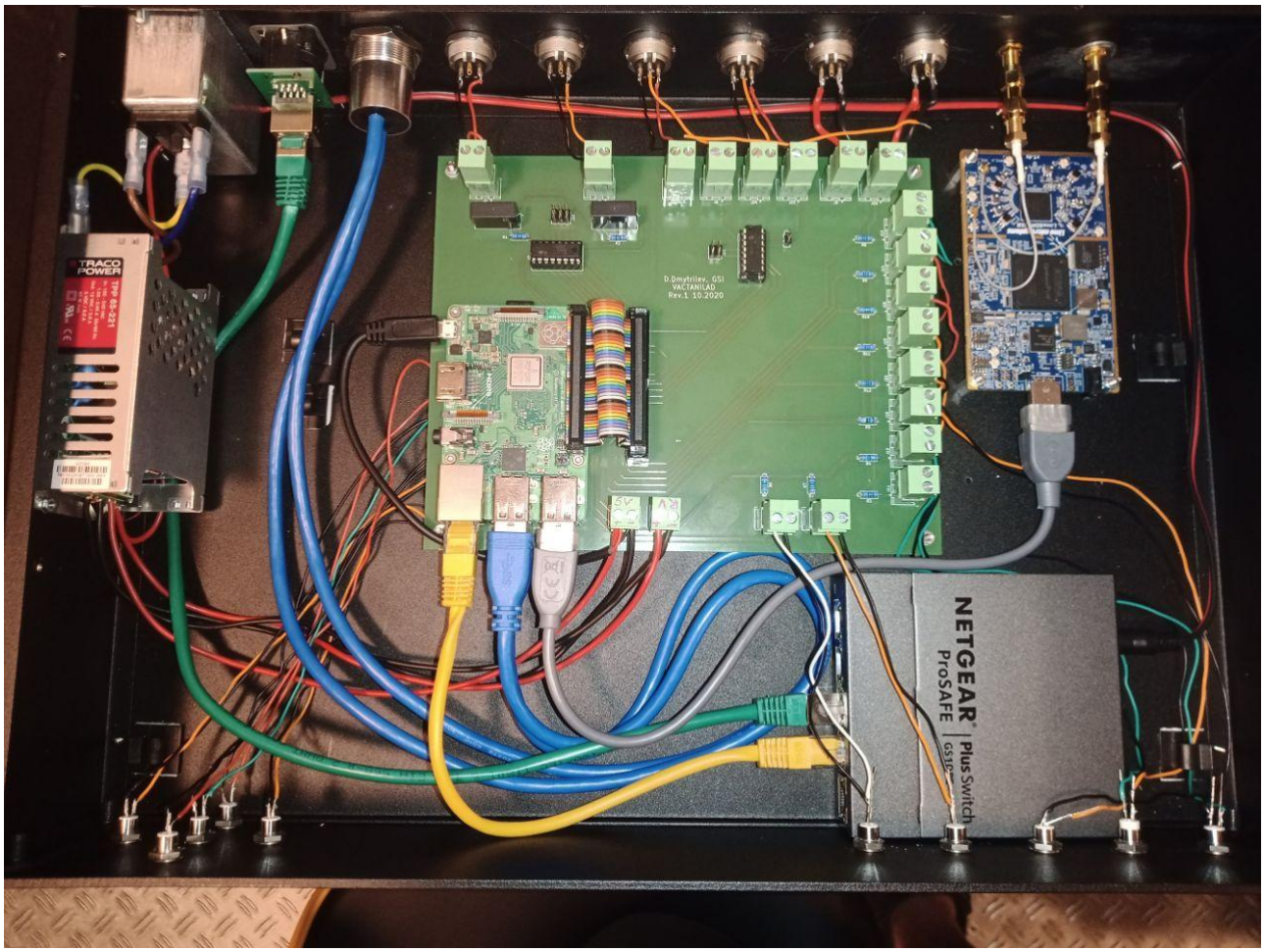

Fig. 7.14: Board connected to peripheral devices.

The front panel of the DAQ box contains 10 LEDs used for the information of the status of its different parts or to illustrate the movement process. There are 5 status LEDs on the right side of the front panel (from left to the right) status of the relay which moves detector UP(if shines then relay is shorted and movement is performing), the status of the relay which moves detector DOWN, 3.3V power line, 5V power line, and 12V power line.

Fig. 7.15: Front panel of the DAQ box.

The rear panel of the DAQ box contains several connectors for motors, relays, and other devices(from right to the left): 220V power supply, USB port for connection to the ISEL motor

controller, two connectors to operate the driver of the lifter, two connectors to read the data from potentiometers, two connectors to feed LNAs with 12V and two SMA connectors to get the RF signal from the LNAs to the SDR.

Fig. 7.16: Rear panel of the DAQ box.

SDR will be used to read out the data from the Schottky cavities. It will be connected to the Schottky via rigid RF cable and low-noise amplifier (LNA) [70]. The scheme of the connection is given in Fig. 7.17

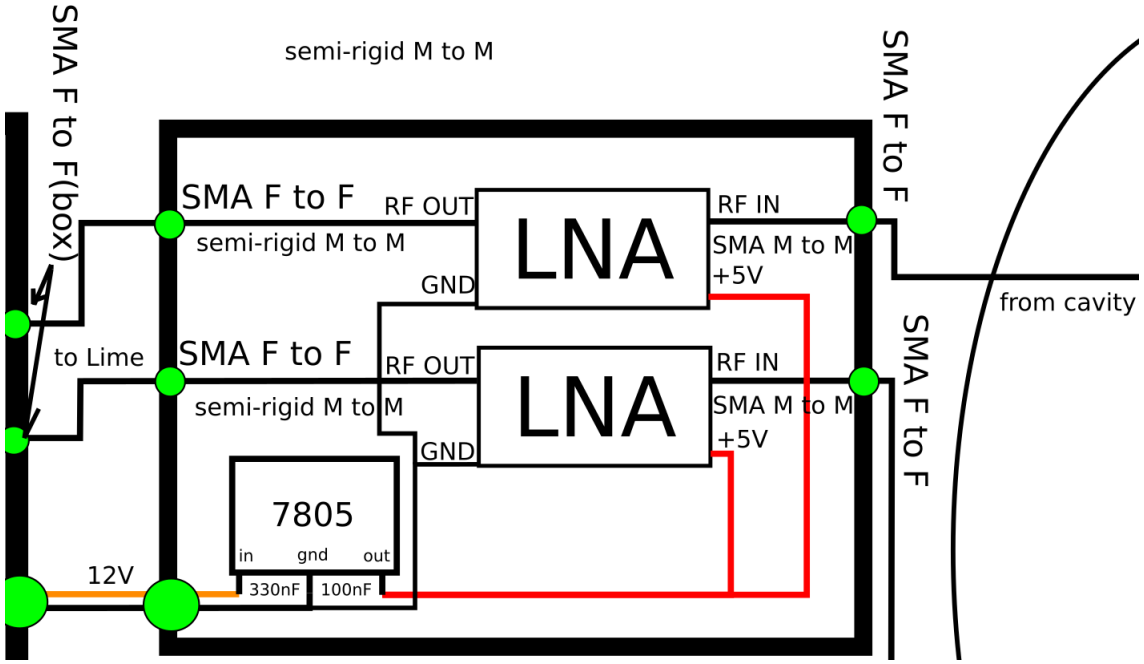

Fig. 7.17: Connection of the LNA to 12V power supply and RF line.

7.6 Blueprints

Our cavities have been constructed and manufactured by Kress GmbH [88] and they also provided us with blueprints for final agreements. To estimate possible restrictions on the geometry of the R3 cavities we were provided with a blueprint of the straight section at R3. An illustration is shown in Fig. 7.18:

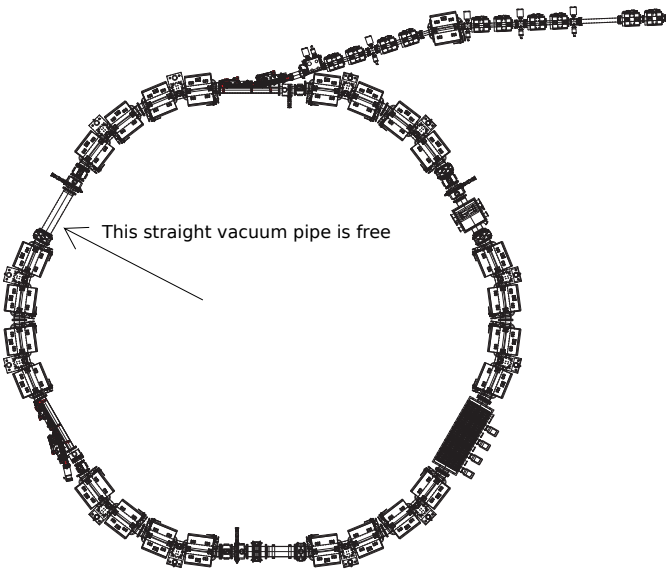

(a) R3 layout with suggested place for the Schottky.

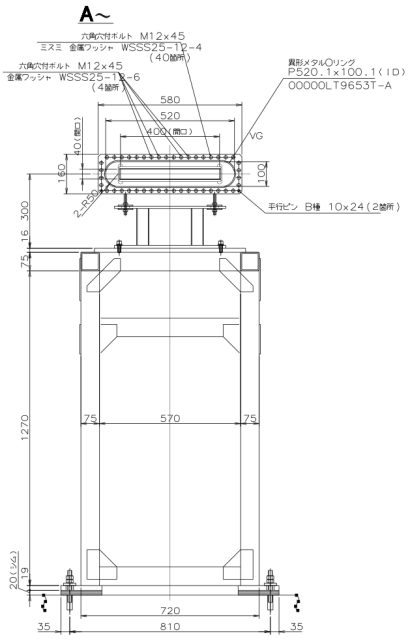

(b) Cross section of the beam pipe at the straight section of the R3.

Fig. 7.18: R3 storage ring layout and beam pipe blueprint.

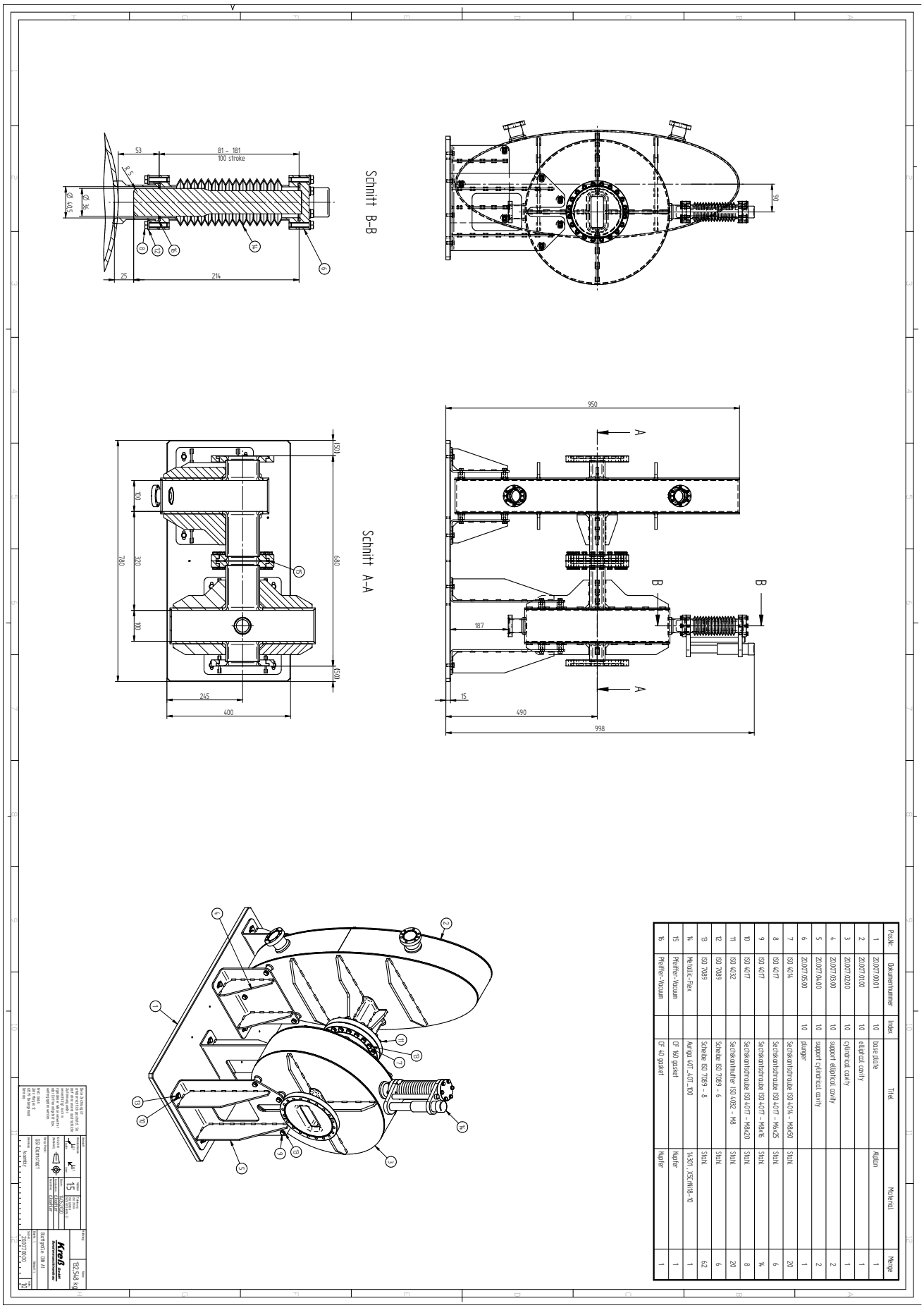

PosNr.	Dokumentnummer	Index	Titel	Material	Menge
1	201.07.00.01	10	base plate	Alubn	1
2	201.07.01.00	10	elliptical cavity		1
3	201.07.02.00	10	cylindrical cavity		1
4	201.07.03.00	10	support elliptical cavity		2
5	201.07.04.00	10	support cylindrical cavity		2
6	201.07.05.00	10	plunger		1
7	ISO 4014		Sechskantschraube ISO 4014 - M8x50	Stahl	20
8	ISO 4017		Sechskantschraube ISO 4017 - M6x25	Stahl	6
9	ISO 4017		Sechskantschraube ISO 4017 - M8x16	Stahl	14
10	ISO 4017		Sechskantschraube ISO 4017 - M8x20	Stahl	8
11	ISO 4032		Sechskantmutter ISO 4032 - M8	Stahl	20
12	ISO 7089		Scheibe ISO 7089 - 6	Stahl	6
13	ISO 7089		Scheibe ISO 7089 - 8	Stahl	62
14	Metallic-Flex		Aurigo 40T-40T_100	1.4301 ; X5CrNi18-10	1
15	Pfeiffer-Vacuum		CF 160 gasket	Kupfer	1
16	Pfeiffer-Vacuum		CF 40 gasket	Kupfer	1

Fig. 7.19: Prototype of the position-sensitive Schottky cavity doublet for the experiment at DALINAC.

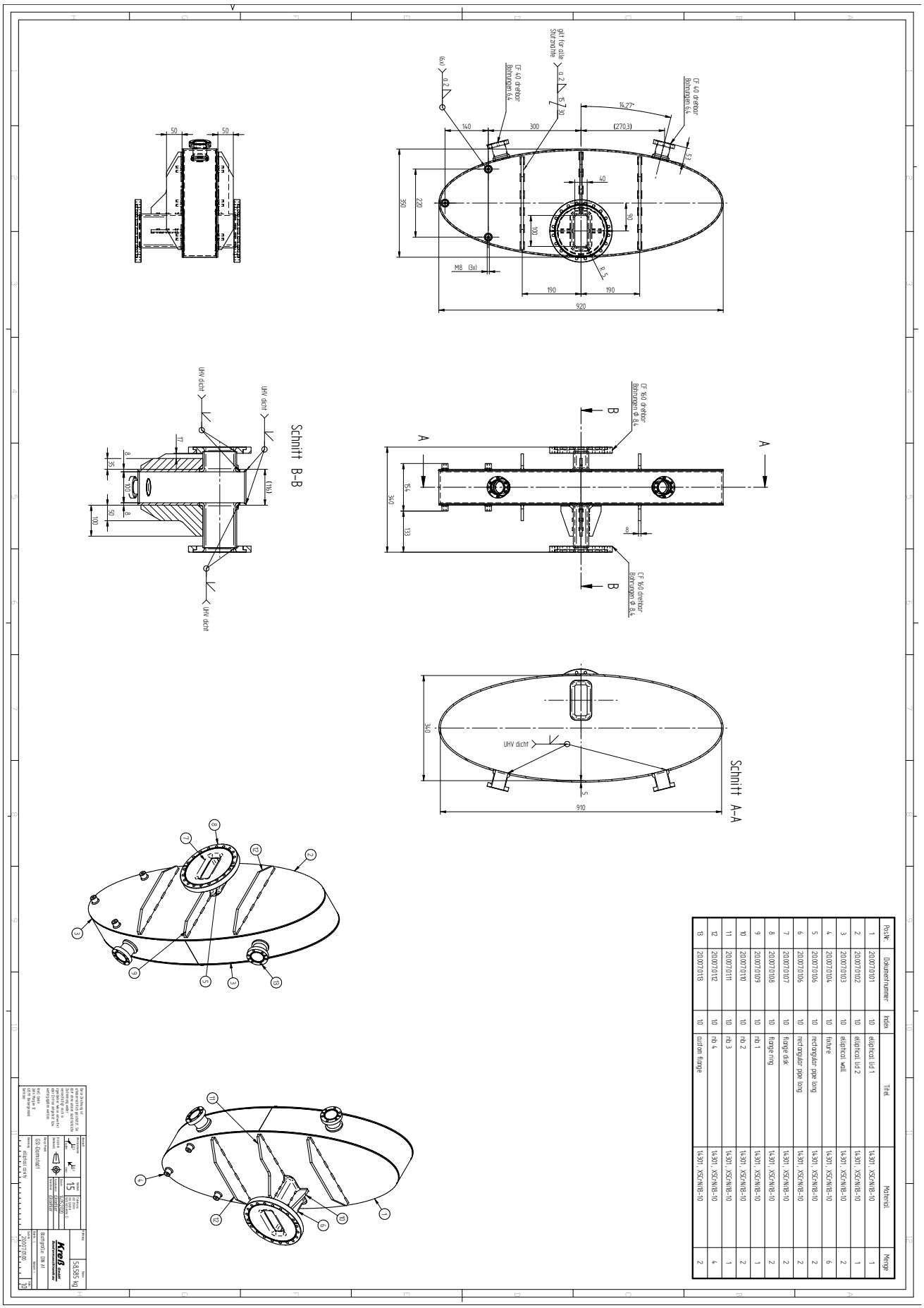

Fig. 7.20: Elliptical cavity blueprint.

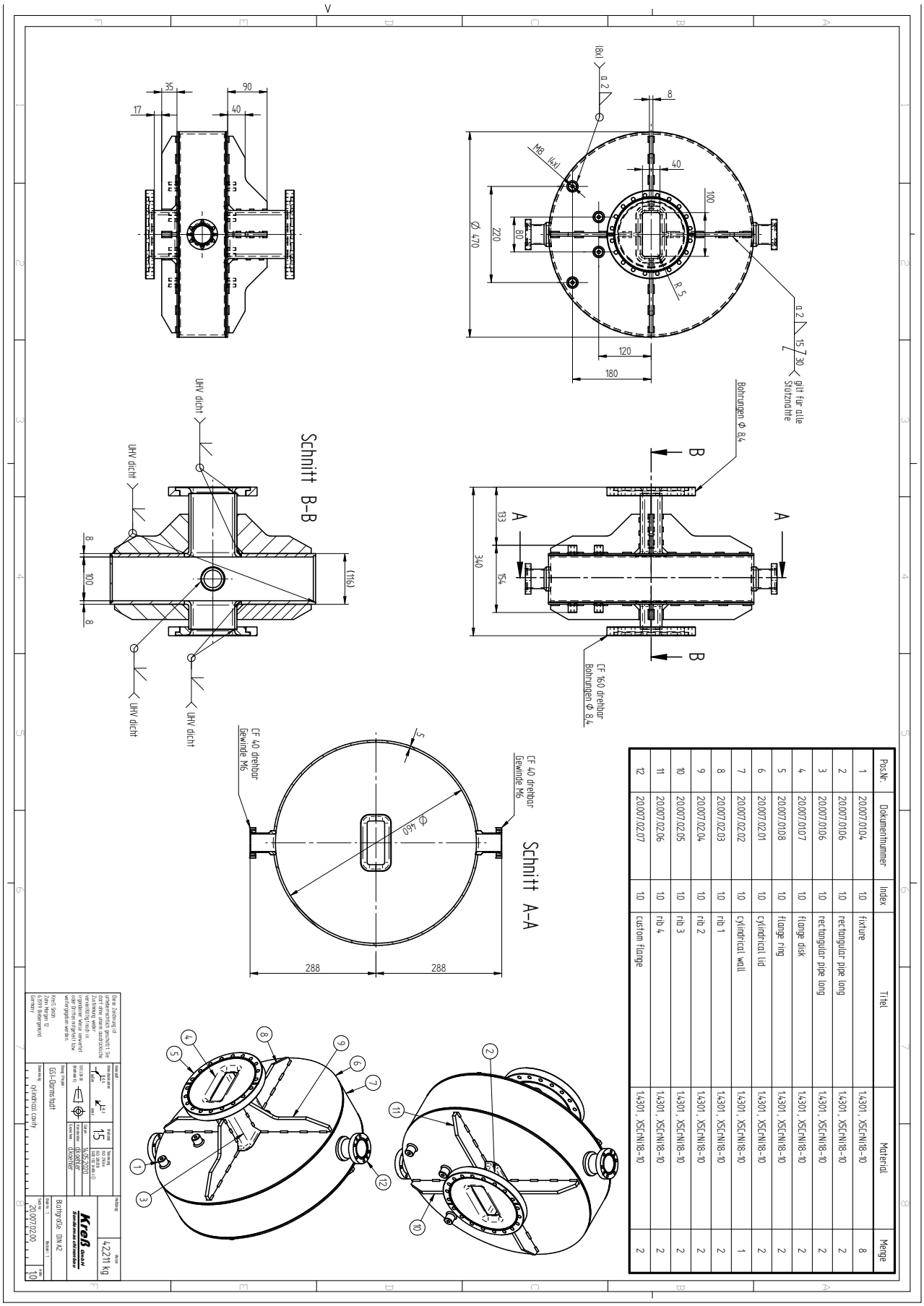

Pos.Nr.	Dokumentnummer	Index	Titel	Material	Menge
1	20.007.0104	10	fixture	1.4301, X5CrNi18-10	8
2	20.007.0106	10	rectangular pipe long	1.4301, X5CrNi18-10	2
3	20.007.0106	10	rectangular pipe long	1.4301, X5CrNi18-10	2
4	20.007.0107	10	flange disk	1.4301, X5CrNi18-10	2
5	20.007.0108	10	flange ring	1.4301, X5CrNi18-10	2
6	20.007.02.01	10	cylindrical lid	1.4301, X5CrNi18-10	2
7	20.007.02.02	10	cylindrical wall	1.4301, X5CrNi18-10	1
8	20.007.02.03	10	rib 1	1.4301, X5CrNi18-10	2
9	20.007.02.04	10	rib 2	1.4301, X5CrNi18-10	2
10	20.007.02.05	10	rib 3	1.4301, X5CrNi18-10	2
11	20.007.02.06	10	rib 4	1.4301, X5CrNi18-10	2
12	20.007.02.07	10	custom flange	1.4301, X5CrNi18-10	2

Fig. 7.21: cylindrical cavity blueprint.

7.7 Circuit schematics and PCB

Using a PCB instead of the usual perforated plate is a more reliable option. However, PCB can not be rebuilt as soon as it is produced. This requires accurate board development starting from the schematic. PCB design has been done using free software KiCad 5.1.7 [89]

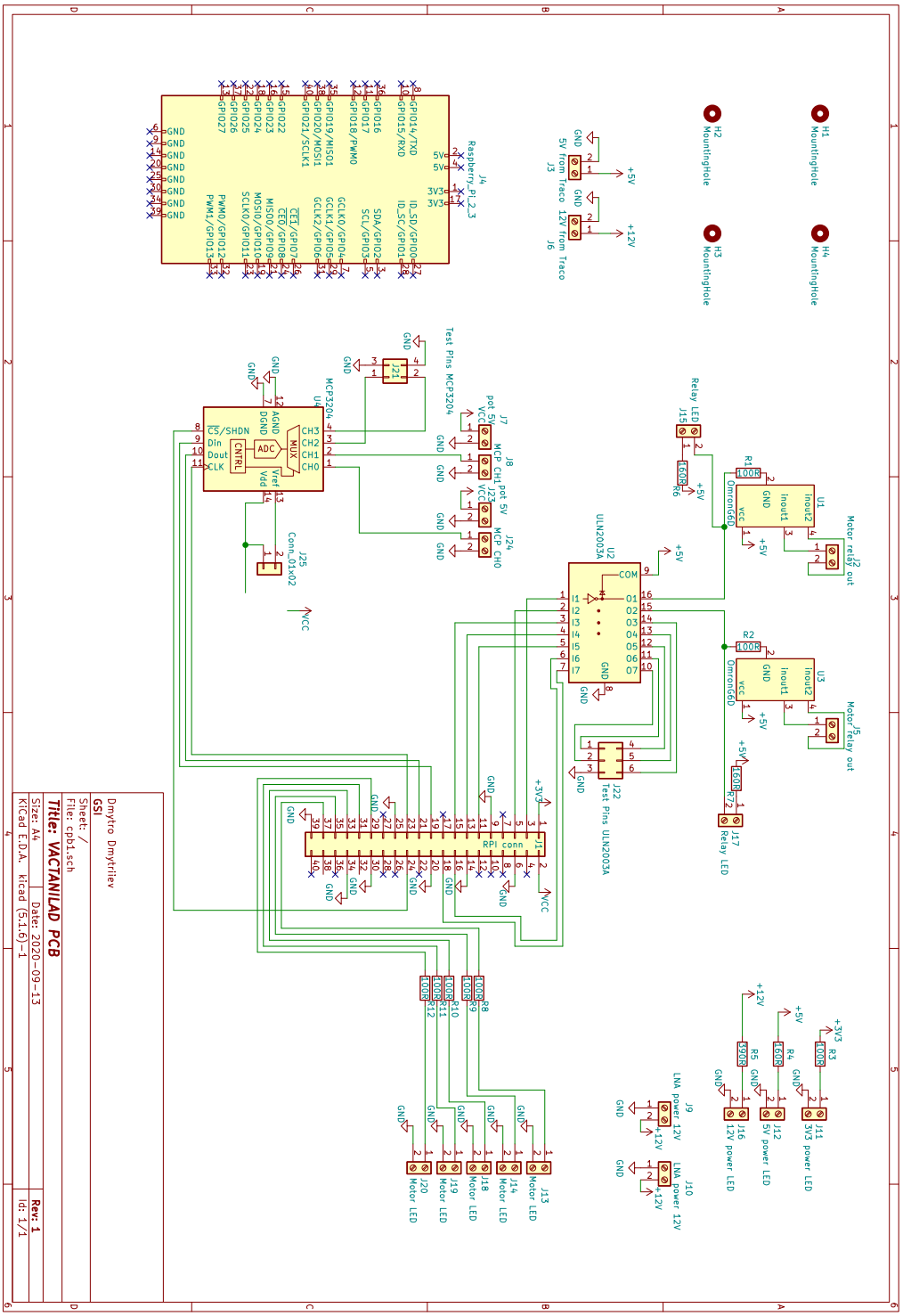

Fig. 7.22: KiCad scheme of PCB for DAQ and control systems

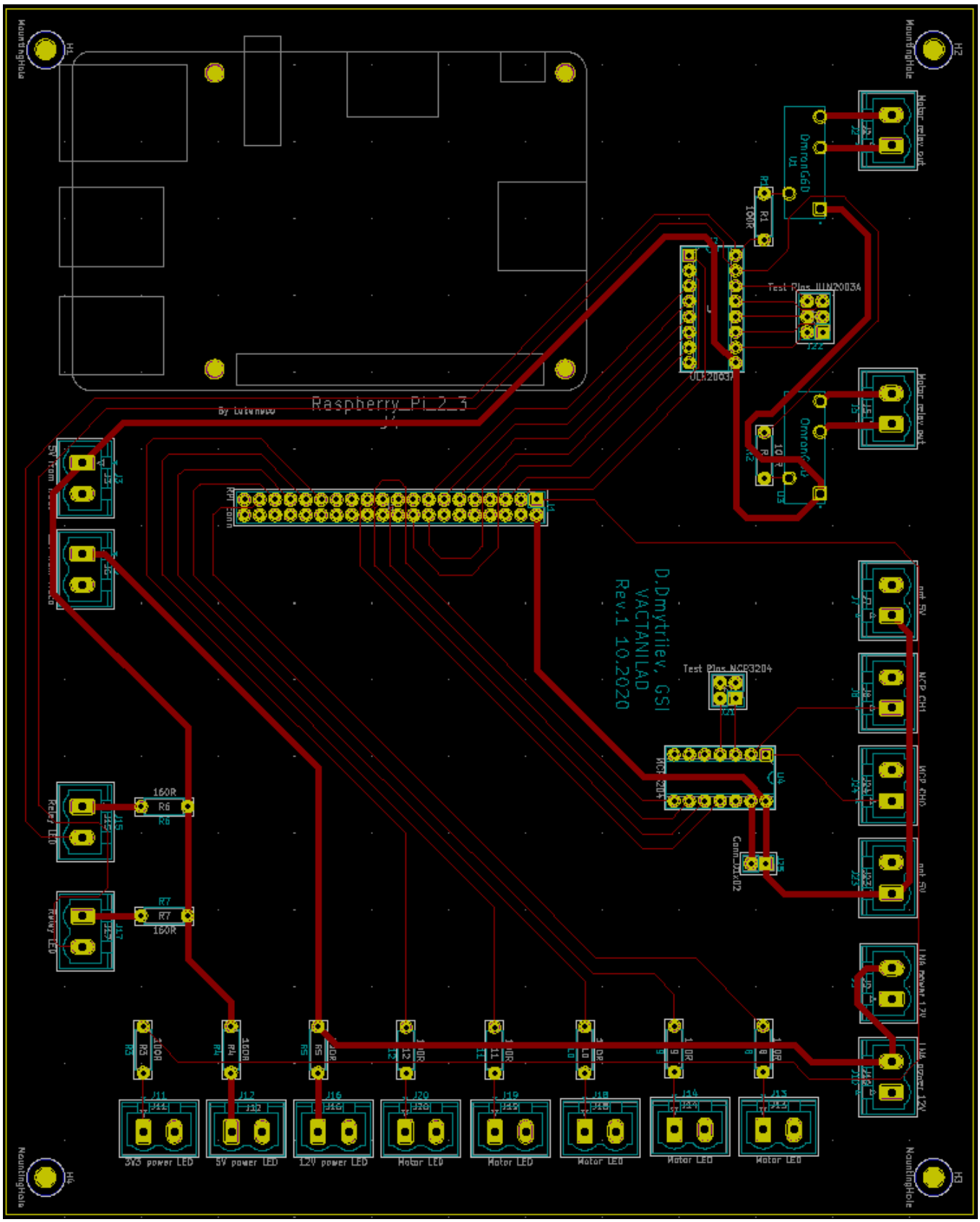

Fig. 7.23: PCB designer scheme of the PCB for DAQ and control systems

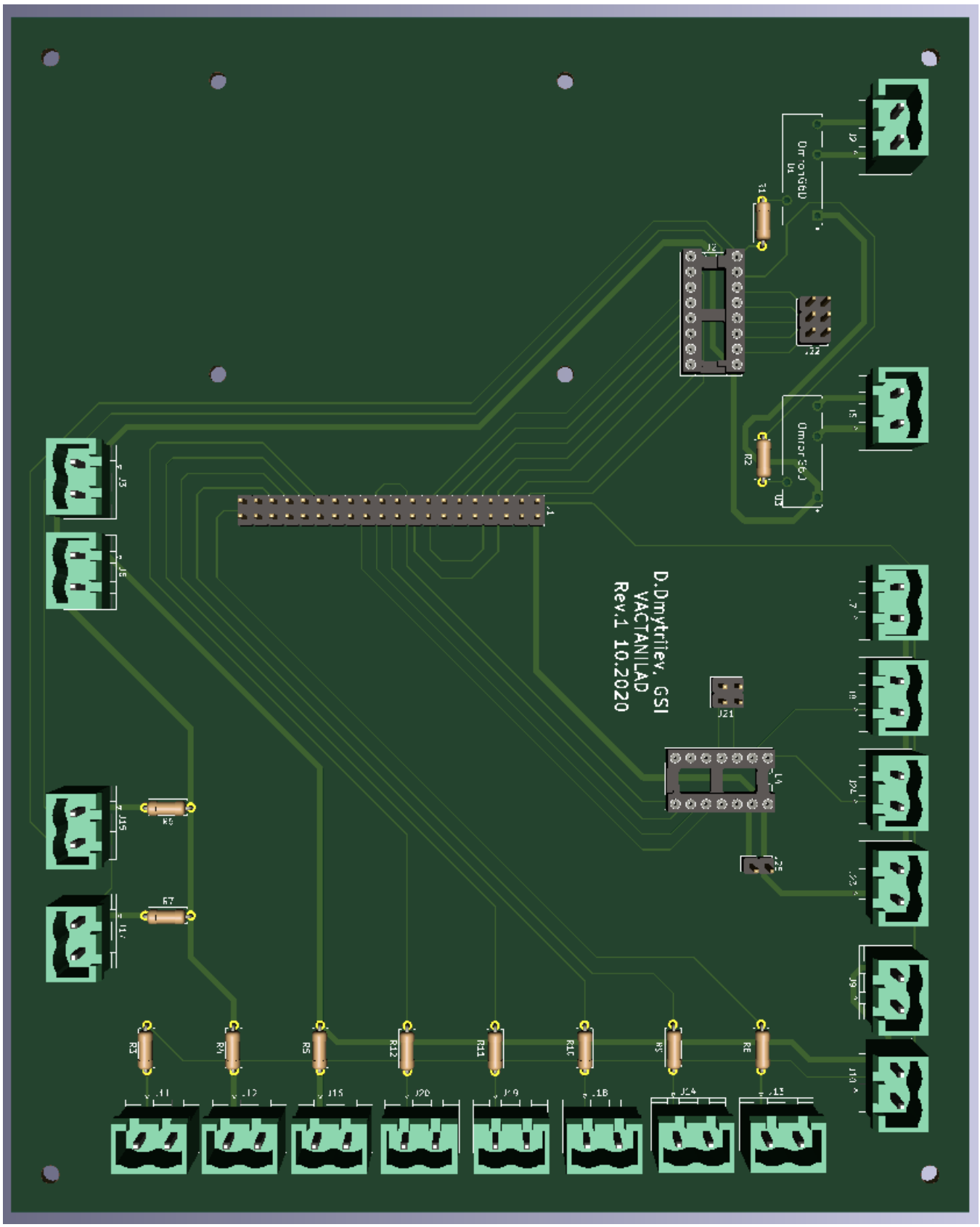

Fig. 7.24: 3D view of PCB

7.8 Gerber files

Gerber files are used by the manufacturer of PCB to unambiguously understand how does the PCB should look. These files also can be used to find a mistake or to optimize space use, etc. There is one file for one layer of PCB. We send files for 6 different layers to the manufacturer but one can use more layers if it is necessary. Along with it, 2 drill files were generated as a map for the drilling machine. In this work, they were exported as PDF files. The edge cut file is not drawn because it is just a rectangle around the PCB which is visible on every other picture.

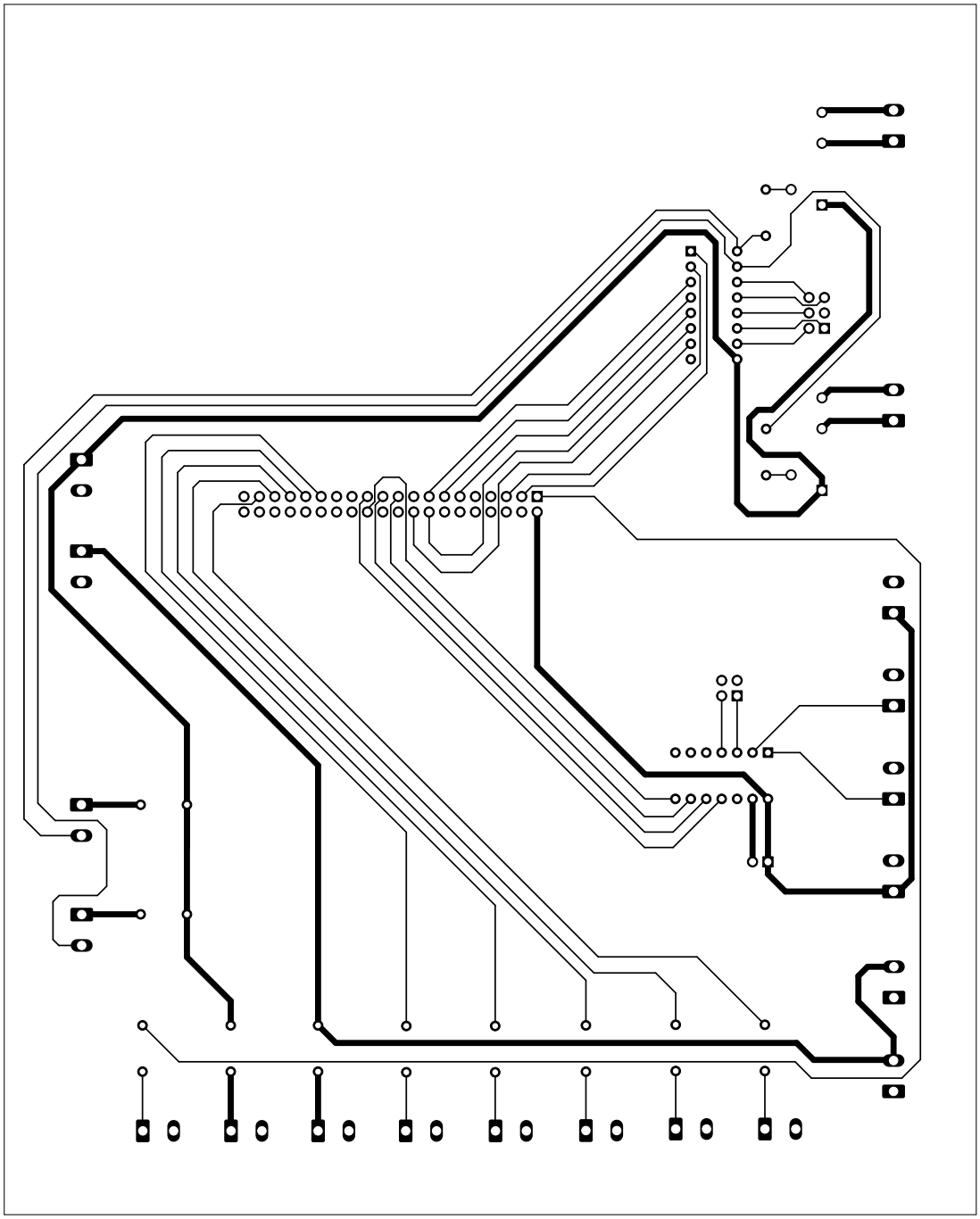

Fig. 7.25: Front copper layer. Tracks and elements' footprints are drawn here. Top view on the PCB

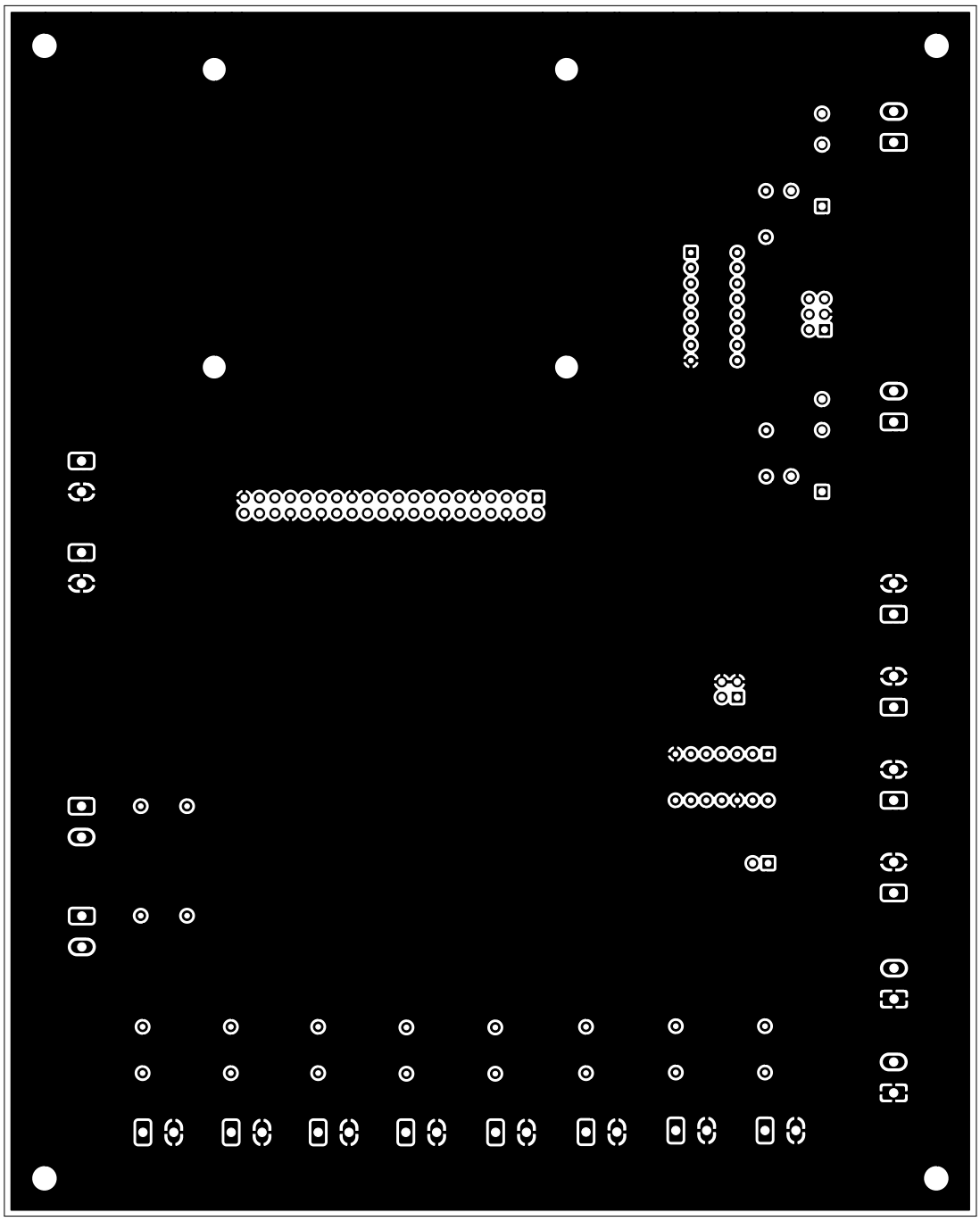

Fig. 7.26: Bottom copper layer. A large ground line which is connected only to the ground pins of elements from the front copper layer

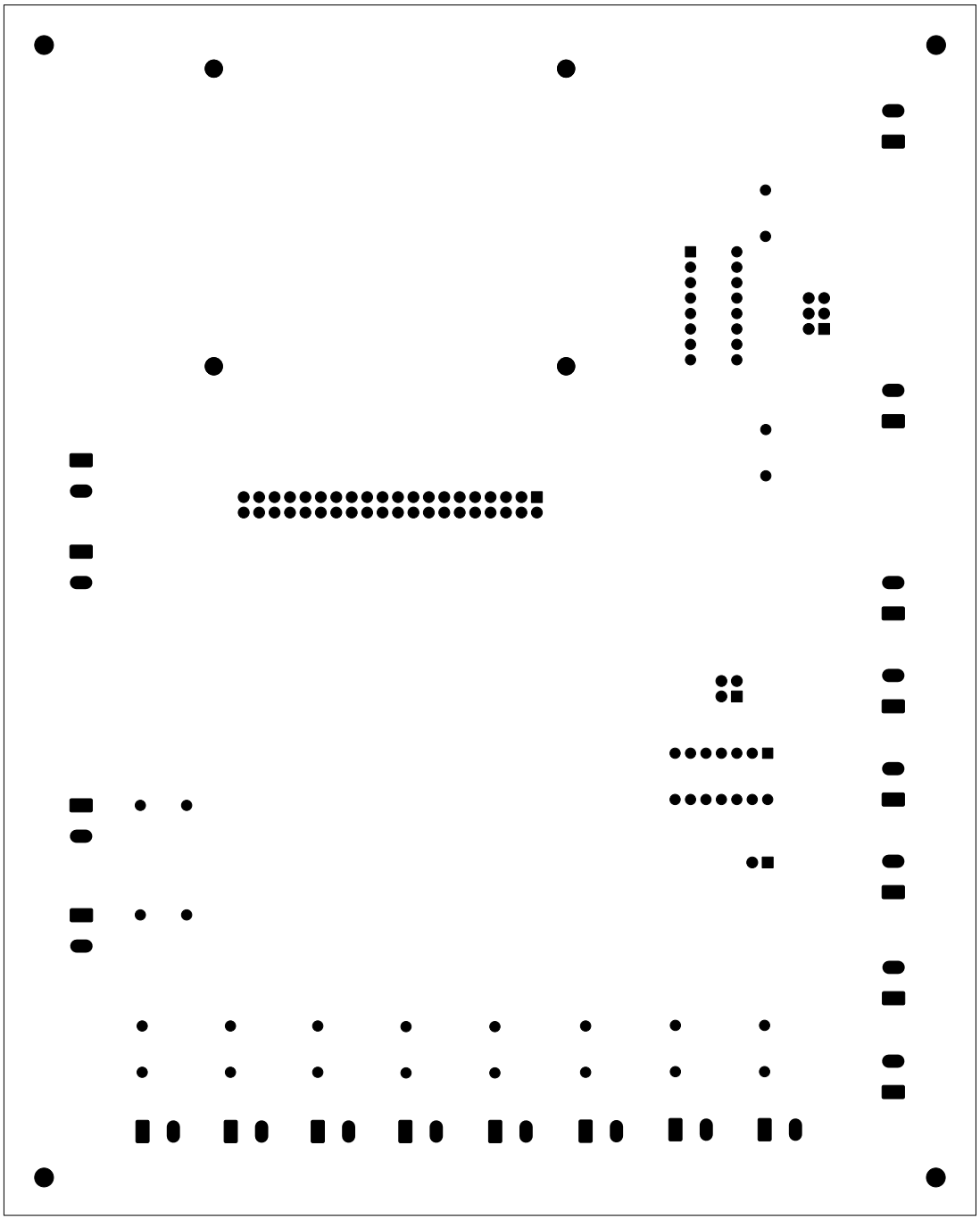

Fig. 7.27: Front and Back mask file shows which parts of a board on the top and the bottom should not be covered by a non-conductive material

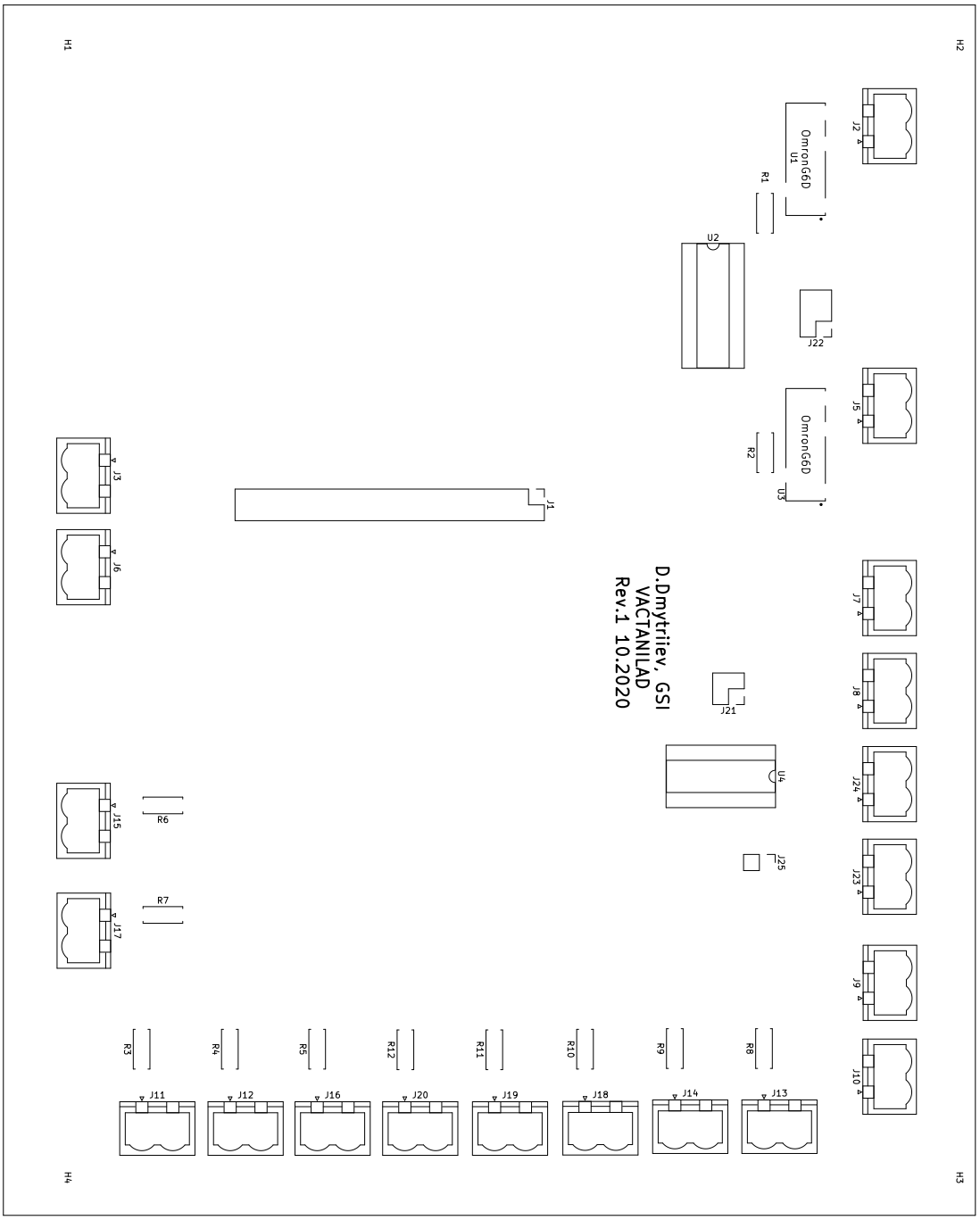

Fig. 7.28: The silk layer shows every footprint for the elements on the top layer of the PCB. Also, it can be used for user-defined writings

7.9 SDR Program

```
#!/usr/bin/env python
#-*-coding:utf-8-*-
'''
A code for the recording data from LimeSDR and saving in .bin file
Output files are suitable for the processing with the iqtools library

2021 D.Dmytriiev

Originally published on https://github.com/Skyedragon/VACTANILAD
'''
import numpy as np
import argparse
from matplotlib import pyplot as plt
import SoapySDR
from SoapySDR import SOAPY_SDR_RX, SOAPY_SDR_CS16
import time

class LimeSDR:
  #at first one has to initialize SDR. Init method sets all
  #preferences and setups the data streams
  #rx_bw - bandwidth, fs - sampling rate
  def __init__(self, cent_freq, meas_time, rx_bw, fs, channel):
    self.channel = channel
    use_agc = True          # Use or don't use the AGC
    self.freq = cent_freq   # LO tuning frequency in Hz
    self.timeout_us = int(5e6)
    self.N = int(fs * meas_time) # Number of complex samples per transfer
    self.rx_bits = 12            # The Lime's ADC is 12 bits
    RX1 = 0                      # RX1 = 0, RX2 = 1
    RX2 = 1
    self.sdr = SoapySDR.Device(dict(driver="lime")) # Create AIR-T instance

    if (len(self.channel) == 2):
          # Set sample rate of receiver
      self.sdr.setSampleRate(SOAPY_SDR_RX, RX1, fs)
      self.sdr.setSampleRate(SOAPY_SDR_RX, RX2, fs)

          # Set the gain mode of receiver
      self.sdr.setGainMode(SOAPY_SDR_RX, RX1, True)
      self.sdr.setGainMode(SOAPY_SDR_RX, RX2, True)

      # Set TransImpedance Amplifier gain
      self.sdr.setGain(SOAPY_SDR_RX, RX1, "TIA", 0)
      self.sdr.setGain(SOAPY_SDR_RX, RX2, "TIA", 0)

      # Set Low-Noise Amplifier gain of receiver
      self.sdr.setGain(SOAPY_SDR_RX, RX1, "LNA", 0)
      self.sdr.setGain(SOAPY_SDR_RX, RX2, "LNA", 0)

      # programmable-gain amplifier (PGA) of receiver
      self.sdr.setGain(SOAPY_SDR_RX, RX1, "PGA", 0)
```

```
        self.sdr.setGain(SOAPY_SDR_RX, RX2, "PGA", 0)

            # Set overall gain if receiver amplifier stage doesn't matter
        self.sdr.setGain(SOAPY_SDR_RX, RX1, 0)
        self.sdr.setGain(SOAPY_SDR_RX, RX2, 0)
        self.sdr.setDCOffsetMode(SOAPY_SDR_RX, 0, False)
        self.sdr.setDCOffsetMode(SOAPY_SDR_RX, 1, False)

            # Tune the LO
        self.sdr.setFrequency(SOAPY_SDR_RX, RX1, self.freq)
        self.sdr.setFrequency(SOAPY_SDR_RX, RX2, self.freq)

            # Create memory buffer for data acquisition
        self.RX1_buff = np.empty(2 * self.N, np.int16)
        self.RX2_buff = np.empty(2 * self.N, np.int16)

            # Set Bandwidth of receiver
        self.sdr.setBandwidth(SOAPY_SDR_RX, RX1, rx_bw)
        self.sdr.setBandwidth(SOAPY_SDR_RX, RX2, rx_bw)

        self.sdr.setAntenna(SOAPY_SDR_RX, RX1, "LNAL")
        self.sdr.setAntenna(SOAPY_SDR_RX, RX2, "LNAL")

        # Create data buffer and start streaming samples to it
        self.rx_stream = self.sdr.setupStream(SOAPY_SDR_RX,\
        SOAPY_SDR_CS16,[RX1, RX2])

    elif(self.channel[0] == 1):
        self.sdr.setSampleRate(SOAPY_SDR_RX, RX1, fs)
        self.sdr.setGainMode(SOAPY_SDR_RX, RX1, True)
        self.sdr.setGain(SOAPY_SDR_RX, RX1, "TIA", 0)
        self.sdr.setGain(SOAPY_SDR_RX, RX1, "LNA", 0)
        self.sdr.setGain(SOAPY_SDR_RX, RX1, "PGA", 0)
        self.sdr.setFrequency(SOAPY_SDR_RX, RX1, self.freq)

            # Create memory buffer for data stream
        self.RX1_buff = np.empty(2 * self.N, np.int16)

        self.sdr.setBandwidth(SOAPY_SDR_RX, RX1, rx_bw)
        self.sdr.setAntenna(SOAPY_SDR_RX, RX1, "LNAL")
        # Start data stream
        self.rx_stream = self.sdr.setupStream(SOAPY_SDR_RX, \
        SOAPY_SDR_CS16, [RX1])


    elif(self.channel[0] == 2):
        self.sdr.setSampleRate(SOAPY_SDR_RX, RX2, fs)
        self.sdr.setGainMode(SOAPY_SDR_RX, RX2, True)
        self.sdr.setGain(SOAPY_SDR_RX, RX2, "TIA", 0)
        self.sdr.setGain(SOAPY_SDR_RX, RX2, "LNA", 0)
        self.sdr.setGain(SOAPY_SDR_RX, RX2, "PGA", 0)
        self.sdr.setFrequency(SOAPY_SDR_RX, RX2, self.freq) # Tune the LO
        self.RX2_buff = np.empty(2 * self.N, np.int16)
```

```
      self.sdr.setBandwidth(SOAPY_SDR_RX, RX2, rx_bw)
      self.sdr.setAntenna(SOAPY_SDR_RX, RX2, "LNAL")
      self.rx_stream = self.sdr.setupStream(SOAPY_SDR_RX, \
      SOAPY_SDR_CS16, [RX2])

    else:
      print("Channel␣amount␣has␣to␣be␣1␣or␣2")

  #this function reads stream of data and puts it
  #in self.rx_stream numpy array
  def get_signal(self):

    #  Initialize the AIR-T receiver using SoapyAIRT
    self.sdr.activateStream(self.rx_stream)  # this turns the radio on
    time.sleep(0.8)

     # Read the samples from the data buffer
    if (len(self.channel) == 2):
      sr = self.sdr.readStream(self.rx_stream, [self.RX1_buff, \
      self.RX2_buff],self.N, timeoutUs = self.timeout_us)

    elif(self.channel[0] == 1):
      sr = self.sdr.readStream(self.rx_stream, [self.RX1_buff], \
      self.N, timeoutUs = self.timeout_us)

    elif(self.channel[0] == 2):
      sr = self.sdr.readStream(self.rx_stream, [self.RX2_buff], \
      self.N, timeoutUs = self.timeout_us)

    rc = sr.ret # number of samples read or the error code
    assert rc == self.N, 'Error␣Reading␣Samples␣from␣Device␣\
␣␣␣␣(error␣code␣=␣%d)!' % rc

    # Stop streaming
    self.sdr.deactivateStream(self.rx_stream)
    self.sdr.closeStream(self.rx_stream)

  #this function makes complex64 from ADC bits and saves it as binary file
  def make_iq(self, filenames):
    if (len(self.channel) == 2):
    # Convert interleaved shorts (received signal) to numpy.complex64
    #normalized between [-1, 1]
      RX1bits = self.RX1_buff.astype(float) / np.power(2.0, self.rx_bits-1)
      RX2bits = self.RX2_buff.astype(float) / np.power(2.0, self.rx_bits-1)
      RX1complex = (RX1bits[::2] + 1j*RX1bits[1::2]).astype(np.complex64)
      RX2complex = (RX2bits[::2] + 1j*RX2bits[1::2]).astype(np.complex64)
      RX1complex = np.complex64(RX1complex)
      RX2complex = np.complex64(RX2complex)
      RX1complex = np.insert(RX1complex, 0, (self.N + 1j*self.freq) )
      RX2complex = np.insert(RX2complex, 0, (self.N + 1j*self.freq) )
      RX1complex.tofile(filenames[0])
      RX2complex.tofile(filenames[1])
```

```
    elif(self.channel[0] == 1):
      RX1bits = self.RX1_buff.astype(float) / np.power(2.0, self.rx_bits-1)
      RX1complex = (RX1bits[::2] + 1j*RX1bits[1::2])
      RX1complex = np.insert(RX1complex, 0, (self.N + 1j*self.freq) )
      RX1complex = np.complex64(RX1complex)
      RX1complex.tofile(filenames[0])

    elif(self.channel[0] == 2):
      RX2bits = self.RX2_buff.astype(float) / np.power(2.0, self.rx_bits-1)
      RX2complex = (RX2bits[::2] + 1j*RX2bits[1::2])
      RX2complex = np.insert(RX2complex, 0, (self.N + 1j*self.freq) )
      RX2complex = np.complex64(RX2complex)
      RX2complex.tofile(filenames[0])

if __name__ == "__main__":
  parser = argparse.ArgumentParser()
  parser.add_argument("--center", type=float, nargs='?', help="Set␣local␣\
␣␣oscillator␣frequency")

  parser.add_argument("--time", type=int, nargs='?', \
  help="Set␣measurement␣time")
  parser.add_argument("--samprate", type=float, nargs='?', \
  help="Set␣sampling␣rate")
  parser.add_argument("--bw", type=float, nargs='?', \
  help="Set␣bandwidth")
  parser.add_argument("--channel", type=int, nargs='+', \
  help="Set␣channels␣to␣read␣data␣from")

  parser.add_argument("--filename", type=str, action='append', nargs='+',
  \ help="Path␣to␣saved␣file")
  args = parser.parse_args()

  if args.time and args.samprate and args.bw and args.filename \
  and args.channel:
    print ("Central␣frequency␣set␣to␣", args.center, "␣Hz.")
    print ("Measurement␣time␣set␣to␣", args.time, "␣sec.")
    print ("Sampling␣rate␣set␣to␣", args.samprate, "␣Samples/sec.")
    print ("Bandwidth␣set␣to␣", args.bw, "␣Hz.")

    if ( len(args.channel) == len(args.filename[0]) and \
    len(args.channel) == 1 ):
      print ("Reading␣from␣channels␣", args.channel[0])
      print ("file␣saved␣as:␣", args.filename[0][0])
      #initialize Lime SDR with entered measure time, bandwidth, \
      sampling rate
      Lime = LimeSDR(args.center, args.time, args.bw, args.samprate, \
      args.channel)
      Lime.get_signal()
      Lime.make_iq(args.filename[0])

    elif ( len(args.channel) == len(args.filename[0]) and \
    len(args.channel) == 2 ):
      print ("Reading␣from␣channels␣", args.channel[0],args.channel[1])
```

```
    print ("file␣saved␣as:␣", args.filename[0][0], args.filename[0][1])
    #initialize Lime SDR with entered measure time, bandwidth,\
     sampling rate
    Lime = LimeSDR(args.center, args.time, args.bw, args.samprate, \
    args.channel)
    Lime.get_signal()
    Lime.make_iq(args.filename[0])

  else:
    print ("channels␣amount␣not␣equal␣to␣amount␣of␣files")
else:
  print ("No␣parameters␣were␣given")
```

7.10 List of publications

- Dmytriiev, D. et al. "Position sensitive resonant Schottky cavities for heavy ion storage rings". *In: Nuclear Instruments and Methods in Physics Research Section B: Beam Interactions with Materials and Atoms* 463 (Jan. 2020), pp. 320–323. issn: 0168583X. doi:10.1016/j.nimb.2019.04.074. Cited as [75].

- Dmytriiev, D. et al. "Software defined radio for Schottky analysis in storage rings". *In: Journal of Physics: Conference Series (2020)* 1668 012014. doi:10.1088/1742-6596/1668/1/012014

- Sanjari, M. S. et al. "A 410 MHz resonant cavity pickup for heavy ion storage rings". *In:Review of Scientific Instruments 91.8 (Aug. 1, 2020)*, p. 083303. issn: 0034-6748, 1089-7623. doi: 10.1063/5.0009094. Cited as [22]

Bibliography

[1] Litvinov, Y. "Nuclear physics experiments with ion storage rings". In: *Nuclear Instruments and Methods in Physics Research Section B: Beam Interactions with Materials and Atoms* 317 (Dec. 15, 2013), pp. 603–616. DOI: https://doi.org/10.1016/j.nimb.2013.07.025.

[2] Franzke, B., Hans Geissel, and Gottfried Münzenberg. "Mass and lifetime measurements of exotic nuclei in storage rings". In: *Mass Spectrometry Reviews* 27.5 (Sept. 2008), pp. 428–469. ISSN: 0277-7037, 1098-2787. DOI: 10.1002/mas.20173.

[3] Franzke, B. "The heavy ion storage and cooler ring project ESR at GSI". In: *Nuclear Instruments and Methods in Physics Research Section B: Beam Interactions with Materials and Atoms* 24-25 (Apr. 1987), pp. 18–25. ISSN: 0168583X. DOI: 10.1016/0168-583X(87)90583-0.

[4] Danared, H. "CRYRING MACHINE STUDIES FOR FLAIR". In: *Proceedings of EPAC*. EPAC. Edinburgh, p. 3.

[5] Xia, J.W. et al. "The heavy ion cooler-storage-ring project (HIRFL-CSR) at Lanzhou". In: *Nuclear Instruments and Methods in Physics Research Section A: Accelerators, Spectrometers, Detectors and Associated Equipment* 488.1 (Aug. 2002), pp. 11–25. ISSN: 01689002. DOI: 10.1016/S0168-9002(02)00475-8.

[6] Yamaguchi, Y. et al. "Rare-RI ring project at RIKEN RI beam factory". In: *Nuclear Instruments and Methods in Physics Research Section B: Beam Interactions with Materials and Atoms* 266.19 (Oct. 2008), pp. 4575–4578. ISSN: 0168583X. DOI: 10.1016/j.nimb.2008.05.081.

[7] Ozawa A. et al. "The RARE-RI ring". In: *Progress of Theoretical and Experimental Physics* 2012.1 (Jan. 1, 2012). ISSN: 2050-3911. DOI: 10.1093/ptep/pts060.

[8] Lunney, D., J. M. Pearson, and C. Thibault. "Recent trends in the determination of nuclear masses". In: *Reviews of Modern Physics* 75.3 (Aug. 20, 2003), pp. 1021–1082. ISSN: 0034-6861, 1539-0756. DOI: 10.1103/RevModPhys.75.1021.

[9] Goeppert Mayer, M. "On Closed Shells in Nuclei". In: *Physical Review* 74.3 (Aug. 1, 1948), pp. 235–239. ISSN: 0031-899X. DOI: 10.1103/PhysRev.74.235.

[10] Weizsäcker, C. F. "Zur Theorie der Kernmassen". In: *Zeitschrift für Physik* 96.7 (July 1935), pp. 431–458. ISSN: 1434-6001, 1434-601X. DOI: 10.1007/BF01337700. URL: http://link.springer.com/10.1007/BF01337700.

[11] Chen, L. et al. "Schottky Mass Measurement of the Hg 208 Isotope: Implication for the Proton-Neutron Interaction Strength around Doubly Magic Pb 208". In: *Physical Review Letters* 102.12 (Mar. 27, 2009), p. 122503. ISSN: 0031-9007, 1079-7114. DOI: 10.1103/PhysRevLett.102.122503.

[12] Bosch, F. "The planned heavy-ion storage-cooler rings: powerful tools for new experiments in nuclear and atomic physics". In: *Physica Scripta* 36.4 (Oct. 1, 1987), pp. 730–736. ISSN: 0031-8949, 1402-4896. DOI: 10.1088/0031-8949/36/4/019.

[13] Bosch, F. "Schottky mass- and lifetime-spectrometry of unstable, stored ions". In: *Journal of Physics B: Atomic, Molecular and Optical Physics* 36.3 (Feb. 14, 2003), pp. 585–597. ISSN: 0953-4075. DOI: 10.1088/0953-4075/36/3/316.

[14] Bosch, F. "Beta decay of highly charged ions". In: *TCP 2006*. Ed. by J. Dilling et al. Berlin, Heidelberg: Springer Berlin Heidelberg, 2007, pp. 157–167. ISBN: 978-3-540-73465-9 978-3-540-73466-6. DOI: 10.1007/978-3-540-73466-6_20.

[15] Bosch, F. "Measurement of Mass and Beta-Lifetime of Stored Exotic Nuclei". In: *The Euroschool Lectures on Physics with Exotic Beams, Vol. I*. Ed. by Jim Al-Khalili and Ernst Roeckl. Vol. 651. Series Title: Lecture Notes in Physics. Berlin, Heidelberg: Springer Berlin Heidelberg, Aug. 20, 2004, pp. 137–168. ISBN: 978-3-540-22399-3 978-3-540-44490-9. DOI: 10.1007/978-3-540-44490-9_5.

[16] Jung, M. et al. "First observation of bound-state β - decay". In: *Physical Review Letters* 69.15 (Oct. 12, 1992), pp. 2164–2167. ISSN: 0031-9007. DOI: 10.1103/PhysRevLett.69.2164.

[17] Bosch, F. "Manipulation of nuclear lifetimes in storage rings". In: *Physica Scripta* T59 (Jan. 1, 1995), pp. 221–229. ISSN: 0031-8949, 1402-4896. DOI: 10.1088/0031-8949/1995/T59/030.

[18] Ohtsubo, T. et al. "Simultaneous Measurement of β - Decay to Bound and Continuum Electron States". In: *Physical Review Letters* 95.5 (July 25, 2005), p. 052501. ISSN: 0031-9007, 1079-7114. DOI: 10.1103/PhysRevLett.95.052501.

[19] Irnich, H. et al. "Half-Life Measurements of Bare, Mass-Resolved Isomers in a Storage-Cooler Ring". In: *Physical Review Letters* 75.23 (Dec. 4, 1995), pp. 4182–4185. ISSN: 0031-9007, 1079-7114. DOI: 10.1103/PhysRevLett.75.4182.

[20] Varga, L. "Proton capture measurements on stored ions for the γ-process nucleosynthesis". Publisher: Heidelberg University Library. PhD thesis. Heidelberg, Germany: Heidelberg University, July 27, 2021.

[21] Nolden, F. et al. "A fast and sensitive resonant Schottky pick-up for heavy ion storage rings". In: *Nuclear Instruments and Methods in Physics Research Section A: Accelerators, Spectrometers, Detectors and Associated Equipment* 659.1 (Dec. 2011), pp. 69–77. ISSN: 01689002. DOI: 10.1016/j.nima.2011.06.058.

[22] Sanjari, M. S. et al. "A 410 MHz resonant cavity pickup for heavy ion storage rings". In: *Review of Scientific Instruments* 91.8 (Aug. 1, 2020), p. 083303. ISSN: 0034-6748, 1089-7623. DOI: 10.1063/5.0009094.

[23] Kienle, P. et al. "High-resolution measurement of the time-modulated orbital electron capture and of the $\beta+$ decay of hydrogen-like 142Pm60+ ions". In: *Physics Letters B* 726.4 (Nov. 2013), pp. 638–645. ISSN: 03702693. DOI: 10.1016/j.physletb.2013.09.033.

[24] Schottky, W. "Über spontane Stromschwankungen in verschiedenen Elektrizitätsleitern". In: *Annalen der Physik* 362.23 (1918), pp. 541–567. ISSN: 00033804, 15213889. DOI: 10.1002/andp.19183622304.

[25] Schlitt, B. et al. "Schottky mass spectrometry at the heavy ion storage ring ESR". In: *Hyperfine Interactions* 99.1 (Dec. 1996), pp. 117–125. ISSN: 0304-3834, 1572-9540. DOI: 10.1007/BF02274915.

[26] Hänsch, T.W. and Schawlow, A.L. "Cooling of gases by laser radiation". In: *Optics Communications* 13.1 (Jan. 1975), pp. 68–69. ISSN: 00304018. DOI: 10.1016/0030-4018(75)90159-5.

[27] Budker, G. I. "An effective method of damping particle oscillations in proton and antiproton storage rings". In: *Soviet Atomic Energy* 22.5 (May 1967), pp. 438–440. ISSN: 0038-531X, 1573-8205. DOI: 10.1007/BF01175204.

[28] Poth, H. "Electron cooling: Theory, experiment, application". In: *Physics Reports* 196.3 (Nov. 1990), pp. 135–297. ISSN: 03701573. DOI: 10.1016/0370-1573(90)90040-9.

[29] van der Meer, S. *Stochastic damping of betatron oscillations in the ISR*. CERN-ISR-PO-72-31, ISR-PO-72-31. Geneva: CERN, 1972.

[30] Möhl, D. et al. "Physics and technique of stochastic cooling". In: *Physics Reports* 58.2 (Feb. 1980), pp. 73–102. ISSN: 03701573. DOI: 10.1016/0370-1573(80)90140-4.

[31] Nolden, F. et al. "Experience and prospects of stochastic cooling of radioactive beams at GSI". In: *Nuclear Instruments and Methods in Physics Research Section A: Accelerators, Spectrometers, Detectors and Associated Equipment* 532.1 (Oct. 2004), pp. 329–334. ISSN: 01689002. DOI: 10.1016/j.nima.2004.06.062.

[32] Hausmann, M. et al. "First isochronous mass spectrometry at the experimental storage ring ESR". In: *Nuclear Instruments and Methods in Physics Research Section A: Accelerators, Spectrometers, Detectors and Associated Equipment* 446.3 (May 2000), pp. 569–580. ISSN: 01689002. DOI: 10.1016/S0168-9002(99)01192-4.

[33] Geissel, H. and Litvinov, Y. "Precision experiments with relativistic exotic nuclei at GSI". In: *Journal of Physics G: Nuclear and Particle Physics* 31.10 (Oct. 1, 2005), S1779–S1783. ISSN: 0954-3899, 1361-6471. DOI: 10.1088/0954-3899/31/10/072.

[34] Sun B. et al. *A new resonator Schottky pick-up for short-lived nuclear investiga- tions*. Gsi Scientific Report. Darmstadt, Germany: GSI, 2011.

[35] Geissel, H. et al. "A new experimental approach for isochronous mass measurements of short-lived exotic nuclei with the FRS-ESR facility". In: *Hyperfine Interactions* 173.1 (Nov. 2006), pp. 49–54. ISSN: 0304-3843, 1572-9540. DOI: 10.1007/s10751-007-9541-4.

[36] Dolinskii, A. et al. "Study of the mass resolving power in the CR storage ring operated as a TOF spectrometer". In: *Nuclear Instruments and Methods in Physics Research Section A: Accelerators, Spectrometers, Detectors and Associated Equipment* 574.2 (May 2007), pp. 207–212. ISSN: 01689002. DOI: 10.1016/j.nima.2007.01.182.

[37] Dolinskii, A. et al. "The CR storage ring in an isochronous mode operation with nonlinear optics characteristics". In: *Nuclear Instruments and Methods in Physics Research Section B: Beam Interactions with Materials and Atoms* 266.19 (Oct. 2008), pp. 4579–4582. ISSN: 0168583X. DOI: 10.1016/j.nimb.2008.05.082.

[38] Zhang, W. et al. "A timing detector with pulsed high-voltage power supply for mass measurements at CSRe". In: *Nuclear Instruments and Methods in Physics Research Section A: Accelerators, Spectrometers, Detectors and Associated Equipment* 755 (Aug. 2014), pp. 38–43. ISSN: 01689002. DOI: 10.1016/j.nima.2014.04.031.

[39] Sanjari, M. S. "Resonant pickups for non-destructive single-particle detection in heavy-ion storage rings and first experimental results". Doctoral Thesis. Germany: Johann Wolfgang Goethe-Universität, May 21, 2013. 164 pp.

[40] Chen, X. "Non-interceptive position detection for short-lived radioactive nuclei in heavy-ion storage rings". PhD thesis. Germany: Heidelberg University, Nov. 18, 2015.

[41] Chen, X. et al. "Intensity-sensitive and position-resolving cavity for heavy-ion storage rings". In: *Nuclear Instruments and Methods in Physics Research Section A: Accelerators, Spectrometers, Detectors and Associated Equipment* 826 (Aug. 2016), pp. 39–47. ISSN: 01689002. DOI: 10.1016/j.nima.2016.04.056. URL: https://linkinghub.elsevier.com/retrieve/pii/S0168900216302649.

[42] Hofmann, A. "Physical phenomena used in beam observation". In: *3rd Joint US-CERN School on Particle Accelerators: Frontiers of Particle Beams, Observation, Diagnosis and Correction*. 1988, pp. 367–379.

[43] Dôme, G. "Basic RF theory, waveguides and cavities". In: *RF Engineering for Particle Accelerators*. CAS '91. Oxford, UK, 1991.

[44] Jensen, E. "Cavity basics". In: *RF for Accelerators*. CAS '10: Ebeltoft, Denmark, 2010, p. 259.

[45] Klein, H. "Basic concepts I". In: *RF Engineering for Particle Accelerators*. CAS '91. Oxford, UK, 1991.

[46] Caspers, F. "RF engineering basic concepts the Smith chart". In: *RF for Accelerators*. CAS '10: Ebeltoft, Denmark, 2010.

[47] Alessini, D. "Power coupling". In: *RF for Accelerators*. CAS '10: Ebeltoft, Denmark, 2010.

[48] Hansli, M. et. al. "CURRENT STATUS OF THE SCHOTTKY SENSOR SYSTEM AT THE CR AT FAIR". In: *International Beam Instrumentation Conference,* IBIS-2013. Oxford, uk, 2013.

[49] Caspers, F. "Schotkky signals for longitudinal and transverse beam diagnostics". In: *RF Basic Concepts*. CAS '15. Geneva, Switzerland, 2015.

[50] Bosch, F. and Litvinov, Y. "Mass and lifetime measurements at the experimental storage ring of GSI". In: *International Journal of Mass Spectrometry* 349-350 (Sept. 2013), pp. 151–161. ISSN: 13873806. DOI: 10.1016/j.ijms.2013.04.025.

[51] Litvinov, S. "Investigation of the Isochronous Mode of the Experimental Storage Ring (ESR) and the Collector Ring (CR). Decay Spectroscopy of Highly Charged Stored 140 Pr Ions at the FRS-ESR Facility". PhD thesis. Apr. 2008.

[52] *CST Microwave Studio Suite*. Version 2020.

[53] Sanjari, M. S. "Conceptual design of elliptical cavity beam position monitors for heavy ion storage rings". In: *International Beam Instrumentation Conference,* IBIS-2014. USA, 2014.

[54] Sanjari, M. S. et al. "Conceptual design of elliptical cavities for intensity and position sensitive beam measurements in storage rings". In: *Physica Scripta* T166 (Nov. 1, 2015), p. 014060. ISSN: 0031-8949, 1402-4896. DOI: 10.1088/0031-8949/2015/T166/014060.

[55] Chen, X. et al. "Accuracy improvement in the isochronous mass measurement using a cavity doublet". In: *Hyperfine Interactions* 235.1 (Nov. 2015), pp. 51–59. ISSN: 0304-3843, 1572-9540. DOI: 10.1007/s10751-015-1183-3. URL: http://link.springer.com/10.1007/s10751-015-1183-3.

[56] Yamaguchi, Y. *Beam commissioning of the rare-RI ring*. RIKEN Accel. Prog. Rep. 49. 2016.

[57] Daisuke, N et al. "First Demonstration of Mass Measurements for Exotic Nuclei Using Rare-RI Ring". In: *Proceedings of 10th International Conference on Nuclear Physics at Storage Rings (STORI'17)*. Kanazawa, Japan: Journal of the Physical Society of Japan, June 15, 2021. ISBN: 978-4-89027-148-1. DOI: 10.7566/JPSCP.35.011014. URL: https://journals.jps.jp/doi/10.7566/JPSCP.35.011014.

[58] Suzaki, F. et al. "A resonant Schottky pick-up for Rare-RI Ring at RIKEN". In: *Physica Scripta* T166 (Nov. 1, 2015), p. 014059. ISSN: 0031-8949, 1402-4896. DOI: 10.1088/0031-8949/2015/T166/014059.

[59] Mueller, J. "Untersuchungen über elektromagnetische Hohlräume". In: *Zeitschrift für Elektrotechnik, Mitteilung aus dem Laboratorium der Telefunken G.m.b.H.* (1939), pp. 157–161.

[60] Maier, L. C. and Slater, J. C. "Field Strength Measurements in Resonant Cavities". In: *Journal of Applied Physics* 23.1 (Jan. 1952), pp. 68–77. ISSN: 0021-8979, 1089-7550. DOI: 10.1063/1.1701980.

[61] Doll, P. *R3 cavity construction*. Darmstadt, Germany: GSI, 2020.

[62] Dermati, K. *FEM calculation*. Darmstadt, Germany: GSI, 2020.

[63] Trageser, C. et al. "A new data acquisition system for Schottky signals in atomic physics experiments at GSI's and FAIR's storage rings". In: *Physica Scripta* T166 (Nov. 1, 2015), p. 014062. ISSN: 0031-8949, 1402-4896. DOI: 10.1088/0031-8949/2015/T166/014062.

[64] Trageser, C. "Aufbau einer Datenaufnahme zur Integration von Schottky-Signalen in Atomphysikexperimenten an Speicherringen". PhD thesis. Gießen: Justus-Liebig-Universität Gießen, Sept. 26, 2018. 179 pp.

[65] *1.8V, 500mA Field Programmable Radio Frequency chip*. LMS7002M. 2018: Lime microsystems. URL: https://limemicro.com/app/uploads/2017/07/LMS7002M-Data-Sheet-v3.1r00.pdf.

[66] *6..12V, 1,5A LimeSDR-USB development board*. LimeSDR-USB. Lime microsystems, 2018. URL: https://wiki.myriadrf.org/LimeSDR-USB_hardware_description.

[67] *List of Software-Defined Radios*. Aug. 2020. URL: https://en.wikipedia.org/wiki/List_of_software-defined_radios.

[68] xaratustrah. *Collection of code for working with offline complex valued time series data*. Mar. 2016. URL: https://github.com/xaratustrah/iqtools.

[69] Tuzlukov, V. P. *Signal processing noise*. OCLC: 52156162. Boca Raton: CRC Press, 2002. ISBN: 978-0-8493-1025-6 978-1-4200-4111-8 978-1-315-22014-7 978-1-351-82734-8.

[70] *Low Noise Amplifier, 50 - 3000 MHz, 50 Ohm*. ZX60-P103LN+. Mini-Circuits, 2020, p. 4.

[71] *Coaxial amplifier, 10-1500 MHz, 50 Ohm*. ZKL-1R5+. Mini-Circuits, 2020, p. 2.

[72] Richter, A. "Operational Experience at the S-DALINAC A". In: EPAC 96: European Particle Accelerator Conference. Bristol, Philadelphia: Inst. of Physics Publ, 1996.

[73] Weiland, T. and Wanzenberg, R. "Wake fields and impedances". In: *Frontiers of Particle Beams: Intensity Limitations*. Ed. by M. Dienes, M. Month, and S. Turner. Vol. 400. Series Title: Lecture Notes in Physics. Berlin, Heidelberg: Springer Berlin Heidelberg, 1992, pp. 39–79. ISBN: 978-3-540-55250-5 978-3-540-46797-7. DOI: 10.1007/3-540-55250-2_26.

[74] *Hebebühne*. SwissBoy 122. Rudolf Grauer AG, 2019.

[75] Dmytriiev, D. et al. "Position sensitive resonant Schottky cavities for heavy ion storage rings". In: *Nuclear Instruments and Methods in Physics Research Section B: Beam Interactions with Materials and Atoms* 463 (Jan. 2020), pp. 320–323. ISSN: 0168583X. DOI: 10.1016/j.nimb.2019.04.074.

[76] Rost, A. "Design, installation and commissioning of new read-out electronics for HADES ECAL and diamond detectors for T0-reconstruction and beam diagnostics". Publisher: UNSPECIFIED. PhD thesis. Darmstadt, Germany: Darmstadt University, 2020. 138 pp.

[77] Lindenberg, K. "Development and Construction of the Low-Energy Photon Tagger NEPTUN". PhD thesis. Darmstadt, Germany, July 2007.

[78] Jian-Hua, C., Tong De-Chun, and Zhao Zhen-Tang. "RF measurements of a C-band cavity beam position monitor". In: *Chinese Physics C* 32.5 (May 2008), pp. 385–388. ISSN: 1674-1137. DOI: 10.1088/1674-1137/32/5/012. URL: https://iopscience.iop.org/article/10.1088/1674-1137/32/5/012.

[79] *SoapySDR*. 2020. URL: https://github.com/pothosware/SoapySDR.

[80] Walker, P. M., Litvinov, Y., and Geissel, H. "The ILIMA project at FAIR". In: International Journal of Mass Spectrometry.349 (2013), pp. 247–254.

[81] Yamaguchi, Y. "COMMISSIONING OF THE RARE-RI RING AT RIKEN RI BEAM FACTORY". In: COOL2015. Newport News, Virginia, USA, 2015, pp. 182–186. ISBN: ISBN 978-3-95450-174-8.

[82] Wu, B. et al. "The design of the Spectrometer Ring at the HIAF". In: *Nuclear Instruments and Methods in Physics Research Section A: Accelerators, Spectrometers, Detectors and Associated Equipment* 881 (Feb. 2018), pp. 27–35. ISSN: 01689002. DOI: 10.1016/j.nima.2017.08.017.

[83] *5V, 5A PCB Relay*. Omron G6D-1A-ASI 5D. Omron Corporation. 2012. URL: https://asset.conrad.com/media10/add/160267/c1/-/en/000503893DS01/datenblatt-503893-omron-g6d-1a-asi-5dc-printrelais-5-vdc-5-a-1-schliesser-1-st.pdf.

[84] *5V, 2,5A Raspberry Pi Compute Module 3+*. Raspberry Pi 3B+. Raspberry Pi Foundation. 2019. URL: https://www.raspberrypi.org/documentation/hardware/computemodule/datasheets/rpi_DATA_CM3plus_1p0.pdf.

[85] *5V, 500mA Seven Darlington array*. ULN2003A. STMicroelectronics. 2012. URL: http://www.farnell.com/datasheets/1690348.pdf.

[86] *3.3-12V, 1mA Potentiometric Linear Transducer*. Megatron RC13G. MEGATRON Elektronik GmbH and Co. KG. 2019. URL: https://www.megatron.de/fileadmin/user_upload/Datenblaetter/Wegsensoren/Potentiometrische/DS_RC13_en.pdf.

[87] *2.7V, 400uA 2.7V 4-Channel/8-Channel 12-Bit A/D Converters with SPI Serial Interface*. MCP3204. Microchip Technology Inc. 2008. URL: https://www.alldatasheet.com/datasheet-pdf/pdf/74936/MICROCHIP/MCP3204.html.

[88] *Kreß GmbH Sondermaschinenbau*. URL: https://www.kress-gmbh.de/.

[89] Batista, R. F. *KiCAD EDA*. Version 5.1.7. 2020. URL: https://www.kicad.org/.

8 Acknowledgments

This work would have not been possible without the guidance and assistance of many people that contributed to the project in various ways.

I am grateful to Apl. Prof. Dr. Yuri A. Litvinov as the leader of the ASTRUm group for accepting me as a Ph.D. student, for his recommendations, scientific guidance, and for involving me in a wide variety of scientific experiments in storage ring as well as involving me in DAAD exchange with our Chinese colleagues from IMP, Lanzhou. Without his efforts, this work would not have even started.

I express my sincerest gratitude to Dr. Shahab Sanjari, who opened for me large gates in the worlds of RF physics, microelectronics, and Python programming. PCB design, microcomputer programming, design and assembling of the RF channels as well as the design of the cavities and understanding of the RF physics - everything which has been done in this work as well as some hobby projects were done under his influence and with his help. Apart from it, Dr. Shahab Sanjari supported me in an understanding of German culture, the German way of life, and understanding of future possible ways after the Ph.D. I can not thank him enough for his influence, patience and support in all aspects of life.

I am thankful to Priv.-Doz. Dr. Wolfgang Quint, for being my referee, for all his suggestions and physics discussions which we had.

I acknowledge Prof. Dr. Klaus Blaum for his supervision and support. His advice and suggestions during the preparations for the conferences as well as scientific guidance greatly improved my understanding of presenting the scientific results.

Without the patience and wisdom of my previous supervisors, I would never reach that far. I want to express my appreciation towards Prof. Dr. Igor Kadenko, Dr. Ruslan Yermolenko, Dr. Oleg Bezshyyko, and Dr. Larisa Bezshyyko for their efforts in raising a high-qualified specialist.

I acknowledge Dr. Sergiy Trotsenko for his assistance and guidance in the dark forest of vacuum equipment and techniques. Without his efforts, the experiment at the Technical University of Darmstadt would be impossible.

I am grateful to Dr. Gleb Vorobjev, Mr. Davide Racano, and Dr. Nikolaos Petridis for their help in the design and construction of the stable supporting structure for the experiment at the Technical University of Darmstadt as well as for our discussions about storage rings engineering.

It is pleasure for me to acknowledge Mr. Wilfried Sturm and Mr. Patrick Doll from GSI as well as Mr. Daniel Koehler from Kress GmbH for their help and patience during the process of construction and manufacturing the position-sensitive cavity doublet for our experiment at the Technical University of Darmstadt. I would also thank Mr. Patrick Doll from GSI for his efforts in the construction of the cavities for the R3 ring.

I am thankful to the ESR team, especially Dr. Sergey Litvinov for his answers about the physics and working process of the storage ring as well as for his outstanding efforts in supporting all experiments on the ESR.

I am particularly thankful to Mr. George Hudson-Chang for his supervision of this work as an English native speaker. He pointed on some mistakes to which I would never pay attention.

Many thanks go to the Atomic Physics group in GSI which supported me during this work. I would express my gratitude to Prof. Dr. Thomas Stöhlker, Mrs. Lea Wunderlich, and Dr. Tatiana Litvinova for the smooth working process of the entire group as well as their priceless help with the arrangement of my documents. I am thankful to members of the Atomic physics group for our everyday life which was nice and funny. I would also express my gratitude to Dr. Pierre-Michel Hillenbrand who helped me in the translation of the Abstract to German.

I acknowledge the Technical University of Darmstadt team, especially Dr. Adrian Rost and Mr. Vadym Kedych for their everyday help in assembling the experimental setup in the experimental hall at the Technical University of Darmstadt. They were always ready to help by utilizing their knowledge, connections at University as well as with hands and instruments. I express my gratitude to Dr. Manuel Steinhorst for his help with the pumping of the experimental setup as well as with understanding the interlock system of the S-DALINAC. I am thankful to Mrs. Manuela Arnold for supervision of our activities at the university and to Dipl.-Ing. Sven Hennings, who greatly helped us as a specialist in radiation safety.

This work would be impossible without the great support of the HGSFP team at Heidelberg University, especially Mrs. Elisabeth Miller, who helped me and my colleagues on every stage of our enrollment in the HGSFP and in the arrangement all necessary documents for the final examination.

It is a great pleasure to know Dr. Xiangcheng Chen, and Ruijiu Chen, with whom we had interesting and fruitful discussions about the Schottky cavities as well as about CSRe in Lanzhou. I can not thank them and Ms. Qian Chen enough for their help in everyday life in Lanzhou. I am grateful to Dr. Yuanming Xing for our physics discussions as well as for the cultural exchange.

I express my warmest gratitude to my Ph.D. colleagues Ivan Kulikov, Laszlo Varga, Ragandeep Singh Sidhu who were always ready for the physics discussions, helped me with document arrangements and first days in Germany, and emotionally supported me during the hard days. Without you, guys, this time would be much worse. I raise my glass to my friends, with whom I had many entertaining adventures and spent "zsir" times together.

Nobody can work efficiently if the other part of life is hard. That is why I would thank all the people who supported me on my way to success. I am thankful to my family who supported and inspired me to pursue a Ph.D. in Germany. I am thankful to Mrs. Anastasiia Vladimirova, Mr. Viktor Rodin, Mr. Volodymyr Rodin, Mr. Roman Poludennyi for our discussions of physics, electronics, and other topics as well as for their support during my studies. I express my sincere gratitude to A. Poludenna, D. Chaban, A. Dzarkovsky, A. Gor, C. Jost, K. Brill, B. Buss, D. Vogt, J. Broden, D. Lockhard, Y. Melisov, E. Egorov, D. Protsko, I. Mamontov, D. Krivenkov, A. Litovchenko, E. Kinash and I. Horoshev for their support and inspiration.

S